Spin-transfer Torque in Magnetic Nanostructures

A Thesis
Presented to
The Academic Faculty

by

Jiang Xiao

In Partial Fulfillment
of the Requirements for the Degree
Doctor of Philosophy

School of Physics
Georgia Institute of Technology
August 2006

Spin-transfer Torque in Magnetic Nanostructures

Approved by:

Prof. Andrew Zangwill, Advisor
School of Physics,
Georgia Institute of Technology

Prof. Phillip First
School of Physics,
Georgia Institute of Technology

Prof. Carlos Sa De Melo
School of Physics,
Georgia Institute of Technology

Prof. Mei-yin Chou
School of Physics,
Georgia Institute of Technology

Dr. Mark D. Stiles
Electron Physics Group,
National Institute of Standards and Technology

Date Approved: May 24, 2006

To my niece,

Zhiyan Xiao,

a lovely girl born during my graduate study.

ACKNOWLEDGEMENTS

Before my thesis finally becomes possible, I owe a lot to many people. First of all, I have to thank my advisor — Andrew Zangwill, for his constant and wise guidance throughout my graduate study and research. I also especially thank Mark Stiles, who patiently offered me help and guidance on almost every step of my research work. Some of my thanks belong to my traveling gang: Guang Yang, Rui Yang, Xiangyu Yang, Xinle Yang, Xun Gu, Yi Liu, Xiaoyue Guan, and Renbin Yan, with whom I enjoyed many trips. I would also like to thank some people here in Atlanta: Zhimin Song, who helped me a lot when I was new to Atlanta; Yaguang Wei & Yujia Wang, who treated me like a family; Xuan Liu and Kun Zhang, who were my great roommates; Stephen Burks & Tara Kilfoyle, and Judy Melton who helped me edit this thesis. Finally, I want to thank my parents and my older brother for their love, support and understanding.

TABLE OF CONTENTS

LIST OF TABLES

LIST OF FIGURES

SUMMARY

This thesis consists of three distinct components: (1) a test of Slocnzewski's theory of spin-transfer torque using the Boltzmann equation, (2) a comparison of macrospin models of spin-transfer dynamics in spin valves with experimental data, and (3) a study of spin-transfer torque in continuously variable magnetization.

Slonczewski developed a simple circuit theory for spin-transfer torque in spin valves with thin spacer layer. We developed a numerical method to calculate the spin-transfer torque in a spin valve using Boltzmann equation. In almost all realistic cases, the circuit theory predictions agree well with the Boltzmann equation results.

To gain a better understanding of experimental results for spin valve systems, current-induced magnetization dynamics for a spin valve are studied using a single-domain approximation and a generalized Landau-Lifshitz-Gilbert equation. Many features of the experiment were reproduced by the simulations. However, there are two significant discrepancies: the current dependence of the magnetization precession frequency, and the presence and/or absence of a microwave quiet magnetic phase with a distinct magnetoresistance signature.

Spin-transfer effects in systems with continuously varying magnetization also have attracted much attention. One key question is under what condition is the spin current adiabatic, i.e., aligned to the local magnetization. Both quantum and semi-classical calculations of the spin current and spin-transfer torque are done in a free-electron Stoner model. The calculation shows that, in the adiabatic limit, the spin current aligns to the local magnetization while the spin density does not. The reason is found in an effective field produced by the gradient of the magnetization in the wall. Non-adiabatic effects arise for short domain walls, but their magnitude decreases exponentially as the wall width increases.

CHAPTER I

INTRODUCTION AND BACKGROUND

This thesis is dedicated to understanding spin-transfer effects in magnetic nanostructures. By "spin-transfer" we mean angular momentum transfer between itinerant electrons and the localized magnetization of a ferromagnet. This chapter provides the background needed to understand the specific calculations that make up the thesis.

1.1 Spin Valve

The most widely studied magnetic nanostructure is the spin valve (Figure 1.1), where a thin-film non-magnet (spacer) is sandwiched between two thin-film ferromagnets. In the range of film thicknesses most commonly used, the magnetization **M** of the "fixed" layer and the magnetization **m** of the thinner "free" layer lie in the plane of the film. **M** and **m** form an angle θ. Nonmagnetic leads connect the spin valve to electron reservoirs.

1.2 Giant Magneto-Resistance

Spin valves exhibit a phenomenon called Giant Magneto-Resistance (GMR) [1, 2], which is a consequence of its structure composed of alternating ferromagnetic and non-magnetic layers (Figure 1.2). The resistance of such multilayers is low when the magnetizations of neighboring ferromagnetic layers are parallel and high when they are antiparallel. The relative change of resistance can be as high as 200%.

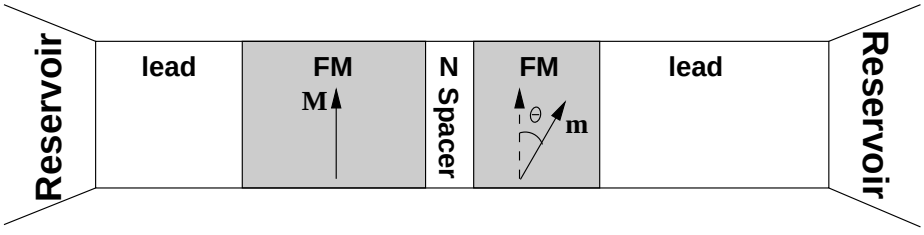

Figure 1.1: Schematic view of a spin valve (not to scale). FM and N layer thicknesses are very small compared to the distance between reservoirs.

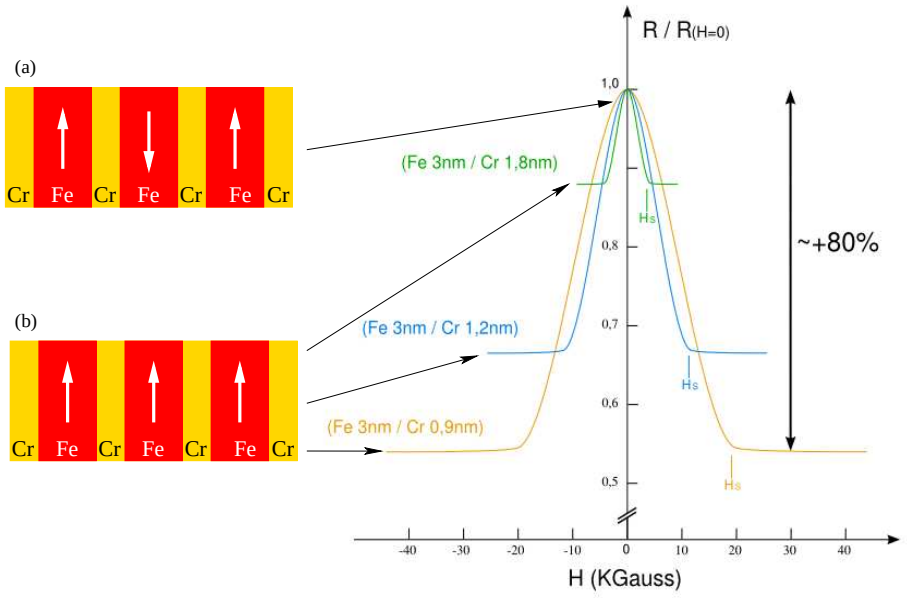

Figure 1.2: Magnetic multilayer structure and GMR.

The reason for the resistance difference between parallel and antiparallel configurations is the following: in a ferromagnet, the majority electrons and minority electrons carry current in parallel, but the majority electrons experience lower resistance than the minority electrons. When a large external field is applied, the magnetizations in different ferromagnetic layers align to the field, and hence parallel to each other as in structure (b) in Figure 1.2. The majority spin-up electrons are majority electrons in all layers. Therefore the spin-up (majority) channel forms a short circuit throughout the multilayer, which leads to lower resistance. At low magnetic field, the magnetostatic interaction causes the magnetizations in adjacent ferromagnetic layers to align antiparallel as in structure (a) in Figure 1.2. In this case, the spin-up (down) electrons are alternatively majority and minority electrons in adjacent layers. Therefore, both the spin-up and spin-down channels have the same resistance. There is no short circuit, and the multilayer has higher resistance.

1.3 Spin-transfer in a Spin Valve

In spin valves experiments, one finds that the resistance depends on the direction of the applied current [3–7]: high resistance when the current flows from fixed layer to free layer, low resistance when the current flows from free layer to fixed layer. Figure 1.3 illustrates

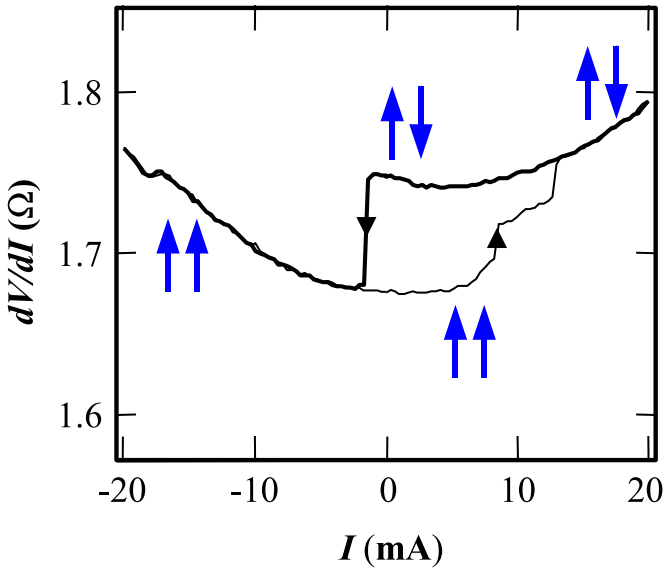

Figure 1.3: Spin valve differential resistance hysteresis curve. (Katine *et. al.* [3])

this with a plot of differential resistance versus current, where the high resistance and low resistance correspond to the anti-parallel and parallel configuration due to the GMR effect. More precisely, the current dependence of the resistance forms a hysteresis loop. This current polarity dependent resistance makes it possible to use a spin valve as a storage bit unit, which can be written as 0 or 1 by applying current in opposite directions.

To understand Figure 1.3 qualitatively, we need the concepts of both electric current I and spin current $\mathbf{Q}$. The electric current is the sum of the current carried by spin-up and spin-down electrons: $I = I_\uparrow + I_\downarrow$; The spin current is the difference: $\mathbf{Q} = I_\uparrow - I_\downarrow$. The direction of $\mathbf{Q}$ is along the spin-up direction in spin space. [1]

For simplicity, we will assume that when an electron spin hits a non-magnet/ferromagnet interface from the non-magnet side (see Figure 1.4), it passes through if its spin is parallel to the magnetization of the ferromagnet, but it is reflected if its spin is anti-parallel to the magnetization. This perfect filter assumption implies that the longitudinal component of an arbitrarily oriented spin current passes through a ferromagnetic layer, while the transverse component is absorbed by the interface. This fact has been shown to be correct to a good approximation in quantum mechanical calculations for realistic materials [8].

[1] This definition of spin current is not rigorous, Ref. [8] gives a more rigorous one.

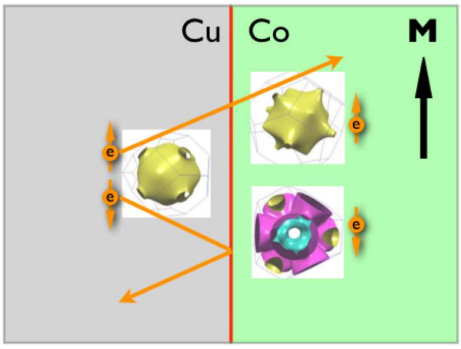

Figure 1.4: Spin dependent interface scattering at a NM/FM interface, the insets are the Fermi surfaces for spin up and spin down electrons in Cu and Co.

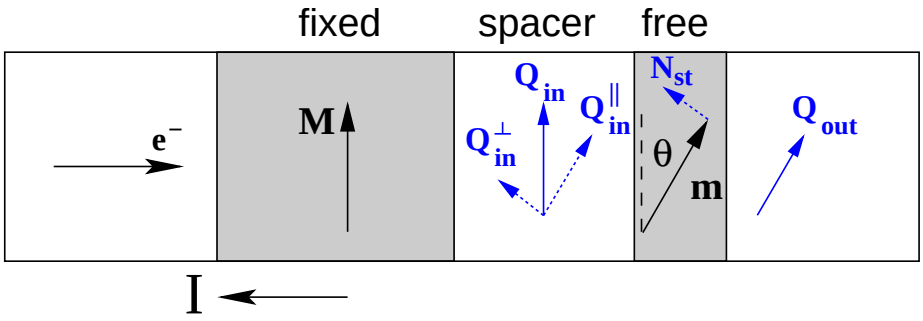

Figure 1.5: This current polarity stabilizes the parallel configuration.

Now, suppose an unpolarized electric current I is sent through a spin valve such that electrons flow from the fixed layer to the free layer (Figure 1.5). If we treat the ferromagnetic layer as a perfect filter as in the previous paragraph, the electric current becomes polarized as it passes through the fixed layer. In other words, in the non-magnetic spacer layer, there is a non-zero spin current $\mathbf{Q}_{\text{in}}$ that is parallel to $\mathbf{M}$. If for any reason, the free layer magnetization $\mathbf{m}$ is not parallel to $\mathbf{M}$, $\mathbf{Q}_{\text{in}}$ can be decomposed into components longitudinal and transverse to $\mathbf{m}$. The longitudinal (parallel) component $\mathbf{Q}_{\text{in}}^{\parallel}$ passes through the free layer and becomes $\mathbf{Q}_{\text{out}}$ (see Figure 1.5),

$$\mathbf{Q}_{\text{out}} = \mathbf{Q}_{\text{in}}^{\parallel}. \tag{1.1}$$

However, the transverse (perpendicular) component $\mathbf{Q}_{\text{in}}^{\perp}$ is absorbed by the interface and the angular momentum associated with $\mathbf{Q}_{\text{in}}^{\perp}$ is deposited into the free layer. Equivalently the absorption produces a torque $\mathbf{N}_{\text{st}}$ on the free layer magnetization $\mathbf{m}$. This torque, $\mathbf{N}_{\text{st}}$, is called *spin-transfer torque*. In Figure 1.5, we see that $\mathbf{N}_{\text{st}}$ pulls $\mathbf{m}$ towards $\mathbf{M}$.

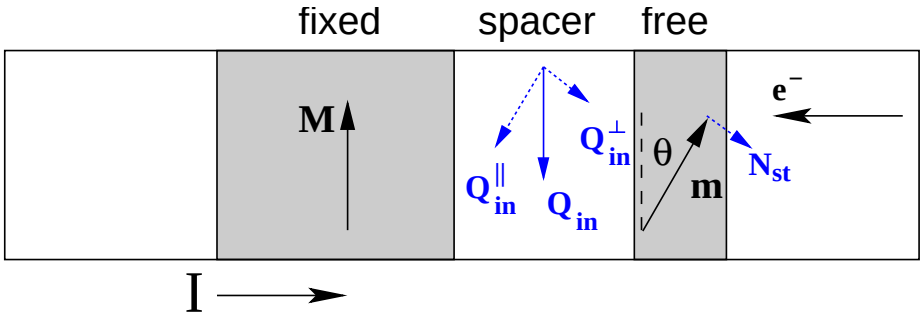

Figure 1.6: This current polarity de-stabilizes parallel configuration.

Therefore this current polarity stabilizes the parallel configuration, and thus leads to low GMR resistance. We can also see the following relations from Figure 1.5:

$$\mathbf{N}_{\rm st} = \mathbf{Q}_{\rm in}^{\perp} = \mathbf{Q}_{\rm in} - \mathbf{Q}_{\rm out}. \tag{1.2}$$

This equation simply states that spin-transfer torque equals the transverse component of the incoming spin current, or the difference between the incoming and outgoing spin current.

On the other hand, if the electric current is applied in the opposite direction, the "incoming" spin current towards the free layer comes from electrons that reflect backwards from the fixed layer. Remember that the spin anti-parallel to the magnetization ($\mathbf{M}$ in this case) is reflected. Therefore $\mathbf{Q}_{\rm in}$ is anti-parallel to $\mathbf{M}$ (Figure 1.6), which results in opposite $\mathbf{Q}_{\rm in}^{\parallel}$ and $\mathbf{Q}_{\rm in}^{\perp}$ compared to the previous case. Consequently, the spin-transfer torque $\mathbf{N}_{\rm st} = \mathbf{Q}_{\rm in}^{\perp}$ pulls $\mathbf{m}$ away from $\mathbf{M}$. Therefore, this current polarity de-stabilizes the parallel configuration and stabilizes the anti-parallel configuration, which leads to high GMR resistance.

Finally, if the current polarization in the spacer layer is $\eta(\theta) = (I_\uparrow - I_\downarrow)/(I_\uparrow + I_\downarrow)$, the spin current is

$$\mathbf{Q}_{\rm in} = \eta(\theta)\frac{I\hbar}{2e}\,\hat{\mathbf{M}}. \tag{1.3}$$

where $\hat{\mathbf{M}}$ denotes the unit vector in $\mathbf{M}$ direction. Since $Q_{\rm in}^{\perp} = Q_{\rm in}\sin\theta$ (see Figure 1.5 and Figure 1.6)

$$\mathbf{N}_{\rm st} = \mathbf{Q}_{\rm in}^{\perp} = \eta(\theta)\frac{I\hbar}{2e}\sin\theta\;\hat{\mathbf{Q}}_{\rm in}^{\perp} = \eta(\theta)\frac{I\hbar}{2e}\mathbf{m}\times(\mathbf{M}\times\mathbf{m}). \tag{1.4}$$

This formula, first derived by Slonczewski [9], is widely used in the literature.

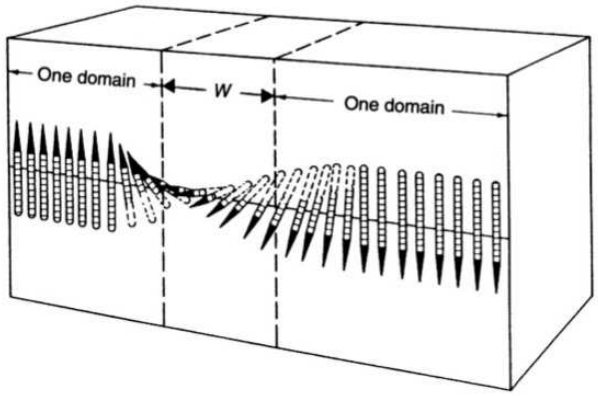

Figure 1.7: Domain wall.

1.4 Spin-transfer in a Domain Wall

Current-induced spin-transfer torque also occurs in continuous nanostructures like a domain wall (Figure 1.7), where the magnetization rotates continously to connect two regions of uniform and antiparallel magnetization. When an electric current passes through a domain wall, one observes domain wall motion [10–19], where the motion direction depends on the current polarity. This can also be explained using spin-transfer torque, at least qualitatively.

A spin-transfer torque (density) formula for continuous magnetization can be derived from Eq. (1.2):

$$\mathbf{N}_{\rm st} = \lim_{\delta x \to 0} \frac{\mathbf{Q}_{\rm in} - \mathbf{Q}_{\rm out}}{\delta x} = \lim_{\delta x \to 0} \frac{\mathbf{Q}(x) - \mathbf{Q}(x+\delta x)}{\delta x} = -\nabla \mathbf{Q}(x), \tag{1.5}$$

where δx is the thickness of the slab in the domain wall under consideration. If we assume that the spin current $\mathbf{Q}(x)$ follows the continuous magnetization adiabatically, *i.e.* $\mathbf{Q}(x) \parallel \mathbf{M}(x)$, then

$$\mathbf{N}_{\rm st} = -\nabla \mathbf{Q}(x) \propto \nabla \mathbf{M}(x). \tag{1.6}$$

In this thesis, we study spin-transfer torque and some of its consequences for a spin valve and for a domain wall. For the spin valve structure, we calculate an analytic spin-transfer torque formula ($\eta(\theta)$ in Eq. (1.4) essentially), and use a Boltzmann equation calculation to confirm the correctness of the formula (Chapter 2). Then, using this formula, we perform a thorough study of the

magnetization dynamics due to spin-transfer torque in a spin valve using the Landau-Lifshitz-Gilbert equation (Chapter 3). For a domain wall structure, we used both analytic and numerical tools to study the adiabaticity of the spin current as a function of on the domain wall width (Chapter 4).

CHAPTER II

SPIN-TRANSFER TORQUE FOR A SPIN VALVE

In this chapter, we calculate the spin-transfer torque acting on the ferromagnetic layers of a spin valve. Section 2.1 describes an analytic circuit theory approach. Section 2.2 gives a numerical approach using a matrix Boltzmann equation. Section 2.3 presents the results from both approaches and compares them.

2.1 Circuit Theory

In pure ferromagnetic material the simple circuit theory used in Figure 1.2 to explain the GMR effect works well. The up-spin and down-spin currents act in parallel. But in a spin valve, there is no obvious choice for the spin quantization axis in the spacer layer that connects the two non-collinear ferromagnetic layers. Based on this observation, Slonczewski developed [20] a theory of spin-transfer torque for a spin valve that combines a density-matrix description of the spacer layer with a circuit theory [21] description of the remainder of the structure. In this section, we generalize the symmetric case studied by Slonczewski to the case of a spin valve with arbitrary geometry.

We start with the region outside of the spacer layer where a circuit theory applies. We then use a density matrix method to study transport inside the spacer layer. Combining the results from outside and inside the spacer layer, we find the spin currents at the interfaces of the spacer layer. We compute the spin-transfer torque from these spin currents.

2.1.1 Outside of the Spacer Layer

We replace the part of the spin valve outside of the spacer layer by the effective circuit shown in Figure 2.1. In this circuit: $I = I_i^{\uparrow} + I_i^{\downarrow}$ is the total electric current, and $I_i^{\uparrow,\downarrow}$ are the currents carried by spin-up and spin-down electrons at the left/right ($i = L, R$) edge of the spacer layer. $R_i^{\uparrow,\downarrow}$ are the *effective* resistances experienced by spin-up and spin-down electrons between the reservoir and the spacer layer, including all resistances from the bulk

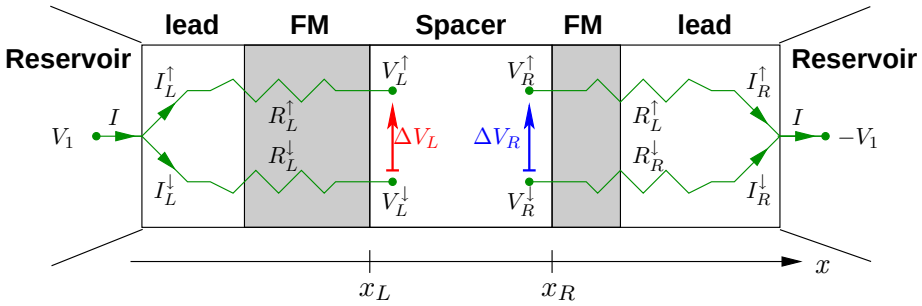

Figure 2.1: Slonczewski's model.

and the interfaces. The V's are the electric potentials at various points (for different spin types). Applying Kirchoff's laws to the circuit gives

$$\Delta V_L = I_L^\downarrow R_L^\downarrow - I_L^\uparrow R_L^\uparrow = -Q_L R_L + I r_L, \tag{2.1a}$$

$$\Delta V_R = I_R^\uparrow R_R^\uparrow - I_R^\downarrow R_R^\downarrow = Q_R R_R - I r_R, \tag{2.1b}$$

where $Q_i = I_i^\uparrow - I_i^\downarrow$ is the spin current at the left/right edge of the spacer layer. $R_i = (R_i^\uparrow + R_i^\downarrow)/2$ is the average resistance for spin-up and spin-down and $r_i = (R_i^\downarrow - R_i^\uparrow)/2$ is the resistance difference between spin-up and spin-down. The relations between $Q_{L,R}$ and $\Delta V_{L,R}$ in Eq. (2.1) are all we need from outside the spacer layer.

2.1.2 Inside the Spacer Layer

Inside the spacer layer, we use a density matrix description to obtain two more relations between $Q_{L,R}$ and $\Delta V_{L,R}$. The two new relations combine with Eq. (2.1) to give four equations with four unknowns ($Q_{L,R}$ and $\Delta V_{L,R}$). From these, we can solve for $Q_{L,R}$, and compute the spin-transfer torque.

We need three steps to find the two new relations: (1) define eigenstates for spin-up and spin-down in the spacer layer using the spin valve's left and right FM layers' spin quantization axes respectively; (2) write down the density matrix using postulated distribution functions with undetermined chemical potentials for each type of spin in the spacer layer; (3) express $Q_{L,R}$ and $\Delta V_{L,R}$ in terms of the chemical potentials, and find the relations between them by eliminating the undetermined chemical potentials.

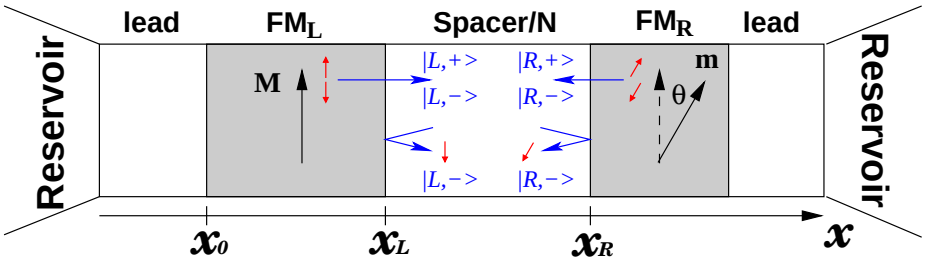

Figure 2.2: States in the spacer layer.

1. Spin states in the spacer layer

In Figure 2.2, the left and right ferromagnetic layers are denoted by $\mathrm{FM_L}$ and $\mathrm{FM_R}$. Their magnetizations are **M** and **m**, respectively, and inclined from one another by an angle θ. $\mathrm{FM_L}$ and $\mathrm{FM_R}$ are separated by a non-magnetic metal spacer layer denoted by N. The two interfaces of the spacer layer, $\mathrm{FM_L/N}$ and $\mathrm{N/FM_R}$, are located at $x = x_L$ and $x = x_R$. We assume there is no scattering within the spacer layer because the spacer layer thickness is much smaller than the mean free path.

The natural electron spin quantization axes in the two ferromagnetic layers align along **M** and **m** respectively. The spin operators for $\mathrm{FM_L}$ and $\mathrm{FM_R}$ can be written as σ_L and σ_R, where $\sigma_L|L,\sigma\rangle = \pm|L,\sigma\rangle$ and $\sigma_R|R,\sigma\rangle = \pm|R,\sigma\rangle$ ($\sigma = \uparrow, \downarrow$). The matrix elements between these spin states are

$$\langle L,\sigma|R,\sigma'\rangle = \begin{bmatrix} \cos(\theta/2) & -\sin(\theta/2) \\ \sin(\theta/2) & \cos(\theta/2) \end{bmatrix} \quad \text{and} \quad \langle i,\sigma|i,\sigma'\rangle = \delta_{\sigma\sigma'} \quad (i = L, R). \tag{2.2}$$

2. Construct a density matrix

We postulate a Fermi distribution function in the spacer layer expanded linearly with respect to one of four chemical potentials μ_σ^γ with $\gamma = \rightarrow$ or $\leftarrow$ and $\sigma = \uparrow$ or $\downarrow$ ($\mu_\sigma^{\rightarrow}$ denotes the potentials for right going electrons from $\mathrm{FM_L}$, $\mu_\sigma^{\leftarrow}$ denotes the potentials for left going electrons from $\mathrm{FM_R}$):

$$f_\sigma^\gamma(\varepsilon) = \left[1 + \exp\left(\frac{\varepsilon_F + \mu_\sigma^\gamma - \varepsilon}{k_B T}\right)\right]^{-1} \approx f^0(\varepsilon) - \left(\frac{\partial f^0}{\partial \varepsilon}\right)_{\varepsilon_F} \mu_\sigma^\gamma. \tag{2.3}$$

In the spacer layer the right going ($\rightarrow$) electrons are either transmitted from $\mathrm{FM_L}$

through the FM_L/N interface or backscattered from N by the FM_L/N interface (see Figure 2.2), so we decompose the right going electron spin using $|L,\uparrow\rangle$ and $|L,\downarrow\rangle$. Similarly, we decompose the left going ($\leftarrow$) electron spin using $|R,\uparrow\rangle$ and $|R,\downarrow\rangle$. Therefore, the density matrix ρ_N in the spacer layer is,

$$\rho_N = \sum_{\sigma=\uparrow,\downarrow} \left(|L,\sigma\rangle \sum_{k_x>0} |\mathbf{k}\rangle f_\sigma^{\rightarrow}(\mathbf{k}) \langle \mathbf{k}|\langle L,\sigma| + |R,\sigma\rangle \sum_{k_x<0} |\mathbf{k}\rangle f_\sigma^{\leftarrow}(\mathbf{k}) \langle \mathbf{k}|\langle R,\sigma| \right). \tag{2.4}$$

3. Two more relations between $Q_{L,R}$ and $\Delta V_{L,R}$

With the density matrix, we can express the number densities for each spin type (n_i^σ) and electric current carried by each spin type (J_i^σ) using either the left ($i = L$) or right ($i = R$) magnetization quantization axis,

$$n_i^\sigma = \langle i,\sigma| \sum_{\mathbf{k}}^{\text{B.Z.}} \langle \mathbf{k}|\rho_N|\mathbf{k}\rangle |i,\sigma\rangle, \tag{2.5a}$$

$$J_i^\sigma = -\frac{e}{m} \langle i,\sigma| \sum_{\mathbf{k}}^{\text{B.Z.}} \langle \mathbf{k}|p_x\rho_N|\mathbf{k}\rangle |i,\sigma\rangle. \tag{2.5b}$$

In Eq. (2.5b) p_x is the x component of the electron momentum.

We assume f^0 is a symmetric function of $\mathbf{k}$ and approximate $\partial_\varepsilon f^0 = -\delta(\varepsilon - \varepsilon_F)$. Let $n_F = -2\sum_k \partial_\epsilon f^0$ be the total electron state density at the Fermi level, and let $n_0 = \sum_{\mathbf{k},\sigma} f^0$

be the electron density. Then Eq. (2.5) can be calculated as

$$
\begin{aligned}
n_i^\sigma &= \langle i,\sigma| \sum_{\mathbf{k}}^{\text{B.Z.}} \langle \mathbf{k}|\rho_N|\mathbf{k}\rangle |i,\sigma\rangle \\
&= \sum_{\sigma'} \langle i,\sigma|L,\sigma'\rangle \sum_{\mathbf{k}}^{\text{B.Z.}} \sum_{\mathbf{k}'}^{\mathbf{k}'_x>0} \langle \mathbf{k}|\mathbf{k}'\rangle f^{\rightarrow}_{\sigma'} \langle \mathbf{k}'|\mathbf{k}\rangle \langle L,\sigma'|i,\sigma\rangle \\
&+ \sum_{\sigma'} \langle i,\sigma|R,\sigma'\rangle \sum_{\mathbf{k}}^{\text{B.Z.}} \sum_{\mathbf{k}'}^{\mathbf{k}'_x<0} \langle \mathbf{k}|\mathbf{k}'\rangle f^{\leftarrow}_{\sigma'} \langle \mathbf{k}'|\mathbf{k}\rangle \langle R,\sigma'|i,\sigma\rangle \\
&= \sum_{\sigma'} \left[\langle i,\sigma|L,\sigma'\rangle^2 \sum_{\mathbf{k},\mathbf{k}'}^{\mathbf{k}'_x>0} \langle \mathbf{k}|\mathbf{k}'\rangle^2 f^{\rightarrow}_{\sigma'} + \langle i,\sigma|R,\sigma'\rangle^2 \sum_{\mathbf{k},\mathbf{k}'}^{\mathbf{k}'_x<0} \langle \mathbf{k}|\mathbf{k}'\rangle^2 f^{\leftarrow}_{\sigma'} \right] \\
&= \sum_{\sigma'} \langle i,\sigma|L,\sigma'\rangle^2 \sum_{\mathbf{k},\mathbf{k}'}^{\mathbf{k}'_x>0} \langle \mathbf{k}|\mathbf{k}'\rangle^2 f^0 + \sum_{\sigma'} \langle i,\sigma|R,\sigma'\rangle^2 \sum_{\mathbf{k},\mathbf{k}'}^{\mathbf{k}'_x<0} \langle \mathbf{k}|\mathbf{k}'\rangle^2 f^0 \\
&+ \sum_{\sigma'} \left[\mu^{\rightarrow}_{\sigma'} \langle i,\sigma|L,\sigma'\rangle^2 \sum_{\mathbf{k}'}^{\mathbf{k}'_x>0} (-\partial_\epsilon f^0)_F + \mu^{\leftarrow}_{\sigma'} \langle i,\sigma|R,\sigma'\rangle^2 \sum_{\mathbf{k}'}^{\mathbf{k}'_x<0} (-\partial_\epsilon f^0)_F \right] \\
&= \frac{1}{2} \sum_{\mathbf{k},\sigma} f^0(\varepsilon) + \frac{1}{2} \sum_{\mathbf{k}'} (-\partial_\epsilon f^0)_F \sum_{\sigma'} \left(\mu^{\rightarrow}_{\sigma'} \langle i,\sigma|L,\sigma'\rangle^2 + \mu^{\leftarrow}_{\sigma'} \langle i,\sigma|R,\sigma'\rangle^2 \right) \\
&= \frac{n_0}{2} + \frac{n_F}{4} \sum_{\sigma'} \left(\mu^{\rightarrow}_{\sigma'} \langle i,\sigma|L,\sigma'\rangle^2 + \mu^{\leftarrow}_{\sigma'} \langle i,\sigma|R,\sigma'\rangle^2 \right). \qquad (2.6)
\end{aligned}
$$

The calculation for J_i^σ is very similar. But to avoid inessential formal integrations, we make the replacement $p_x \to m v_0 \ \text{sgn}(k_x)$ where v_0 is a constant parameter,

$$
\begin{aligned}
J_i^\sigma &= -\frac{e}{m} \langle i,\sigma| \sum_{\mathbf{k}}^{\text{B.Z.}} \langle \mathbf{k}|p_x \rho_N|\mathbf{k}\rangle |i,\sigma\rangle \\
&= -ev_0 \sum_{\sigma'} \langle i,\sigma|L,\sigma'\rangle \sum_{\mathbf{k}}^{\text{B.Z.}} \sum_{\mathbf{k}'}^{\mathbf{k}'_x>0} \langle \mathbf{k}|\mathbf{k}'\rangle \text{sgn}(\mathbf{k}'_x) f^{\rightarrow}_{\sigma'} \langle \mathbf{k}'|\mathbf{k}\rangle \langle L,\sigma'|i,\sigma\rangle \\
&- ev_0 \sum_{\sigma'} \langle i,\sigma|R,\sigma'\rangle \sum_{\mathbf{k}}^{\text{B.Z.}} \sum_{\mathbf{k}'}^{\mathbf{k}'_x<0} \langle \mathbf{k}|\mathbf{k}'\rangle \text{sgn}(\mathbf{k}'_x) f^{\leftarrow}_{\sigma'} \langle \mathbf{k}'|\mathbf{k}\rangle \langle R,\sigma'|i,\sigma\rangle \\
&= \frac{e n_F v_0}{4} \sum_{\sigma'} \left(-\mu^{\rightarrow}_{\sigma'} \langle i,\sigma|L,\sigma'\rangle^2 + \mu^{\leftarrow}_{\sigma'} \langle i,\sigma|R,\sigma'\rangle^2 \right). \qquad (2.7)
\end{aligned}
$$

Plugging Eq. (2.2) into Eq. (2.6) and Eq. (2.7), n_i^σ and J_i^σ can be rewritten in matrix form

in terms of the chemical potentials μ_σ^γ:

$$\begin{bmatrix} n_L^\uparrow \\ n_L^\downarrow \\ n_R^\uparrow \\ n_R^\downarrow \end{bmatrix} = \frac{n_0}{2} + \frac{n_F}{4} \begin{bmatrix} 1 & 0 & \cos^2\frac{\theta}{2} & \sin^2\frac{\theta}{2} \\ 0 & 1 & \sin^2\frac{\theta}{2} & \cos^2\frac{\theta}{2} \\ \cos^2\frac{\theta}{2} & \sin^2\frac{\theta}{2} & 1 & 0 \\ \sin^2\frac{\theta}{2} & \cos^2\frac{\theta}{2} & 0 & 1 \end{bmatrix} \begin{bmatrix} \mu_\uparrow^\rightarrow \\ \mu_\downarrow^\rightarrow \\ \mu_\uparrow^\leftarrow \\ \mu_\downarrow^\leftarrow \end{bmatrix}, \tag{2.8a}$$

$$\begin{bmatrix} J_L^\uparrow \\ J_L^\downarrow \\ J_R^\uparrow \\ J_R^\downarrow \end{bmatrix} = \frac{en_F v_0}{4} \begin{bmatrix} -1 & 0 & \cos^2\frac{\theta}{2} & \sin^2\frac{\theta}{2} \\ 0 & -1 & \sin^2\frac{\theta}{2} & \cos^2\frac{\theta}{2} \\ -\cos^2\frac{\theta}{2} & -\sin^2\frac{\theta}{2} & 1 & 0 \\ -\sin^2\frac{\theta}{2} & -\cos^2\frac{\theta}{2} & 0 & 1 \end{bmatrix} \begin{bmatrix} \mu_\uparrow^\rightarrow \\ \mu_\downarrow^\rightarrow \\ \mu_\uparrow^\leftarrow \\ \mu_\downarrow^\leftarrow \end{bmatrix}. \tag{2.8b}$$

There are four relations between n_i^σ's and J_i^σ's embedded in Eq. (2.8). Two of them are

$$n_R^\uparrow + n_R^\downarrow = n_L^\uparrow + n_L^\downarrow \ , \tag{2.9a}$$

$$J_R^\uparrow + J_R^\downarrow = J_L^\uparrow + J_L^\downarrow \ . \tag{2.9b}$$

These equations say that the total electron density and total charge current do not depend on the choice of quantization axis.

To extract the other two relations, we need two equations: (1) the spin current $Q_i = S(J_i^\uparrow - J_i^\downarrow)$ where S is the cross-sectional area of the device, and (2) the voltage difference near the interfaces for spin-up and spin-down is proportional to the number density difference: $\Delta V_i = (2/en_F)(n_i^\downarrow - n_i^\uparrow)$. Using these two equations, Eq. (2.8) reduces to

$$\begin{bmatrix} Q_L \\ Q_R \\ G\Delta V_L \\ G\Delta V_R \end{bmatrix} = \frac{en_F v_0}{4} \begin{bmatrix} -1 & 1 & \cos\theta & -\cos\theta \\ -\cos\theta & \cos\theta & 1 & -1 \\ -1 & 1 & -\cos\theta & \cos\theta \\ -\cos\theta & \cos\theta & -1 & 1 \end{bmatrix} \begin{bmatrix} \mu_\uparrow^\rightarrow \\ \mu_\downarrow^\rightarrow \\ \mu_\uparrow^\leftarrow \\ \mu_\downarrow^\leftarrow \end{bmatrix}, \tag{2.10}$$

where $G = Se^2k_F^2/4\pi^2\hbar$ and k_F is the Fermi wave vector. From Eq. (2.10), we obtain two more equations that contains Q's and ΔV's by eliminating μ's:

$$0 = Q_L(1+\cos^2\theta) - 2Q_R\cos\theta - G\Delta V_L\sin^2\theta, \tag{2.11a}$$

$$0 = \Delta V_L(1+\cos^2\theta) - 2\Delta V_R\cos\theta - G^{-1}Q_L\sin^2\theta. \tag{2.11b}$$

Note that Q_L and Q_R are the components of the total spin current parallel to the magnetization of the left and right ferromagnet. Therefore, if $\mathbf{Q}$ is the spin current in the spacer layer, $Q_L = \mathbf{Q} \cdot \mathbf{M}$ and $Q_R = \mathbf{Q} \cdot \mathbf{m}$. With Eq. (2.1) and Eq. (2.11), we can express $Q_{L,R}$ in terms of the resistances $r_{L,R}$ and $R_{L,R}$.

2.1.3 Spin-transfer Torque Formula

To relate the spin-transfer torque to $Q_{L,R}$, we examine the total torque acting on the spacer layer and the total spin current injected into it. If $\mathbf{N}_{L,R}$ is the spin-transfer torque acting on the spacer layer at the left/right interface ($\mathrm{FM_L/N}$ interface at x_L and $\mathrm{N/FM_R}$ interface at x_R), the total torque acting on the spacer layer is equal to the total angular momentum deposited by spin current,

$$\mathbf{N}_L + \mathbf{N}_R = \frac{\hbar}{2e}(Q_L\ \hat{\mathbf{M}} - Q_R\ \hat{\mathbf{m}}). \tag{2.12}$$

Since the spin-transfer torque equals the transverse spin current, the torques at the left and right interface should be perpendicular to the adjacent magnetization,

$$\mathbf{N}_L \cdot \hat{\mathbf{M}} = 0 \qquad \text{and} \qquad \mathbf{N}_R \cdot \hat{\mathbf{m}} = 0, \tag{2.13}$$

From Eq. (2.12) and Eq. (2.13), we conclude that the magnitude of the spin-transfer torque that acts on $\mathrm{FM_R}$ is

$$N_{\mathrm{st}}^{\mathrm{R}}(\theta) = -N_R = \frac{\hbar}{2e}\frac{Q_R\cos\theta - Q_L}{\sin\theta} \tag{2.14}$$

Collecting Eq. (2.11), Eq. (2.1), Eq. (2.13) and Eq. (2.14), and solving for $\mathbf{N}_{\mathrm{st}}^R$, gives the spin-transfer torque in the form derived in Chapter 1 [Eq. (1.4)]:

$$\mathbf{N}_{\mathrm{st}}^{\mathrm{R}}(\theta) = \eta(\theta)\frac{\hbar I}{2e}\ \hat{\mathbf{m}} \times (\hat{\mathbf{m}} \times \hat{\mathbf{M}}), \tag{2.15}$$

where

$$\eta(\theta) = \frac{q_+}{A + B\cos\theta} + \frac{q_-}{A - B\cos\theta}, \tag{2.16}$$

and

$$\begin{aligned} q_\pm &= \frac{1}{2}\left[P_L\Lambda_L^2\sqrt{\frac{\Lambda_R^2+1}{\Lambda_L^2+1}} \pm P_R\Lambda_R^2\sqrt{\frac{\Lambda_L^2-1}{\Lambda_R^2-1}}\right], \\ A &= \sqrt{(\Lambda_L^2+1)(\Lambda_R^2+1)} \quad \text{and} \quad B = \sqrt{(\Lambda_L^2-1)(\Lambda_R^2-1)}. \end{aligned} \tag{2.17}$$

The parameters $P_{L,R}$ and $\Lambda_{L,R}$ are defined in terms of the effective resistance parameters $r_{L,R}$ and $R_{L,R}$:

$$P_i = \frac{\frac{1}{2}(R_i^{\downarrow} - R_i^{\uparrow})}{\frac{1}{2}(R_i^{\downarrow} + R_i^{\uparrow})} = \frac{r_i}{R_i} \qquad \text{and} \qquad \Lambda_i^2 = GR_i \qquad (i = L, R), \tag{2.18}$$

If the spin valve is symmetric, *i.e.* both the geometry and the material are the same on both side of the spacer layer, then $\Lambda_L = \Lambda_R = \Lambda$ and $P_L = P_R = P$. This makes $q_- = 0$ and Eq. (2.15) reduces to Slonczewski's formula [9, 20]. An equivalent spin-transfer torque formula was obtained by Manschot *et. al.* [22] independently.

2.1.4 Determine the Parameters in the Spin-transfer Torque Formula

To determine the parameters $\Lambda_{L,R}$ and $P_{L,R}$, we start with an exact expression for the voltage difference ΔV_L in Eq. (2.1): [1]

$$\Delta V_L = \int_{-\infty}^{x_L} dx[I_{\downarrow}(x)\rho_{\downarrow}(x) - I_{\uparrow}(x)\rho_{\uparrow}(x)]. \tag{2.19}$$

$\rho_{\uparrow,\downarrow}(x)$ is the resistivity experienced by spin-up/down electrons at position x. The average resistivity (used below) is $\bar{\rho} = (\rho_{\uparrow} + \rho_{\downarrow})/2$, and the resistivity difference is $\Delta\rho = (\rho_{\downarrow} - \rho_{\uparrow})/2$. Both $\bar{\rho}$ and $\Delta\rho$ contain delta functions at the non-magnet/ferromagnet interfaces to take account of spin-dependent interface scattering.

From the drift-diffusion approximation [23], we know that close to the outer $x = x_0$ interface (see Figure 2.2), $I_{\uparrow}(x)$ and $I_{\downarrow}(x)$ approach the corresponding bulk values exponentially in both directions. [2] The decay length is the spin-flip length in each material, $l_{\rm sf}^{\rm F}$ for the ferromagnet (F) and $l_{\rm sf}^{\rm N}$ for the non-magnet (N), and the thickness of each layer are $t_{\rm N}^{L/R}$ for left/right lead, and $t_{\rm F}^{L/R}$ for left/right ferromagnet. In that case, an approximate expression for Eq. (2.19) can be written as

$$\Delta V_L = Q_0\bar{\rho}_{\rm N}d_{\rm N}^L + Q_0\bar{\rho}_{\rm F}d_{\rm F}^L + I\Delta\rho_{\rm F}d_{\rm F}^L + \Delta V_I + \Delta V_C. \tag{2.20}$$

[1] Here, we are working in the Ohmic limit and not the ballistic limit.

[2] If $I_{\downarrow}(x)$ and $I_{\uparrow}(x)$ take the bulk value, either in non-magnet or ferromagnet, then $I_{\downarrow}(x)\rho_{\downarrow}(x) = I_{\uparrow}(x)\rho_{\uparrow}(x)$. So the non-zero contribution to Eq. (2.19) comes from the region where $I_{\uparrow,\downarrow}$ has deviation from its bulk value, which is corresponding to the spin accumulation region.

Table 2.1: Material parameters used in circuit theory.

Parameter	Material	Value	Units	Reference
ρ	Cu	6	nΩ·m	[24]
$\rho_\uparrow$	Co	40.5	nΩ·m	[24]
$\rho_\downarrow$	Co	109.5	nΩ·m	[24]
$R_I^\uparrow$	Co/Cu	0.117	fΩ·m^2	[24]
$R_I^\downarrow$	Co/Cu	0.903	fΩ·m^2	[24]
$l_{\rm sf}$	Cu	450	nm	[25]
$l_{\rm sf}$	Co	59	nm	[26]
G	Cu	$2.3 \cdot 10^{-15}$	Ω^{-1}·m^{-2}	
$\bar{R}_I$	Co/Cu	0.51	fΩ·m	
ΔR_I	Co/Cu	0.393	fΩ·m	
$\bar{\rho}$	Co	75	nΩ·m	
$\Delta\rho$	CO	34.5	nΩ·m	

$Q_0 = Q(x_0)$, ΔV_I and ΔV_C are voltage drops at the internal interfaces and at the reservoir contact. The effective lengths

$$d_{\rm F}^L = l_{\rm sf}^{\rm F}\left[1 - \exp(-t_{\rm F}^L/l_{\rm sf}^{\rm F})\right] \quad \text{and} \quad d_{\rm N}^L = l_{\rm sf}^{\rm N}\left[1 - \exp(-t_{\rm N}^L/l_{\rm sf}^{\rm N})\right], \tag{2.21}$$

appear because, due to spin-flip scattering, only electrons within $d_{\rm F}$ or $d_{\rm N}$ of the ferromagnetic interfaces can accommodate the dissimilar spin-currents characteristic of the ferromagnets and the non-magnets in equilibrium.

The relationship between Q_0 and $Q_L(x)$ is nontrivial [23] except when the ferromagnet is very thin ($t_{\rm F}^{\rm L} \ll l_{\rm sf}^{\rm F}$). In that case, $Q_0 = Q_L(x_0) \simeq Q_L(x)$, and we can connect Eq. (2.20) to Eq. (2.1) and Eq. (2.15) to get

$$\Lambda_L^2 = G(\bar{\rho}_{\rm N} d_{\rm N}^L + \bar{\rho}_{\rm F} t_{\rm F}^L + \bar{R}_I + \bar{R}_C) \quad \text{and} \quad P_L = G\Lambda_L^{-2}(\Delta\rho_{\rm F} t_{\rm F}^L + \Delta R_I + \Delta R_C). \tag{2.22}$$

Here, the interface resistances $\bar{R}_I$, and ΔR_I and the contact resistance $\bar{R}_C$, and ΔR_C are defined similar to $\bar{\rho}$ and $\Delta\rho$. These two formulas (and similar ones for Λ_R and P_R), together with Eq. (2.15) and Eq. (2.17) are the principal results of this section. The numerical values for the various parameters used in Eq. (2.21) and Eq. (2.22) for a spin valve are listed in Table. 2.1.

2.2 Boltzmann Approach

This section describes a method to calculate spin-transfer torque in spin valve systems using a matrix Boltzmann equation. [3] The main improvement over the circuit theory is a consideration of the differences between the electrons from different parts of the Fermi surface.

The calculation proceeds in eight steps: (1) make simplifications for the Fermi surfaces; (2) construct a matrix distribution function and a matrix Boltzmann equation to handle the ferromagnetic layers and discretize the Boltzmann equation on the Fermi sphere; (3) solve the Boltzmann equation for the eigensolutions in the non-magnetic bulk and the ferromagnetic bulk; (4) use the eigensolutions to construct a scattering matrix for each bulk layer in the spin valve; (5) construct the scattering matrix for each interface in the spin valve; (6) connect the bulk and interface scattering matrices into a single system-wide scattering matrix; (7) apply boundary conditions from the reservoirs to the system-wide scattering matrix to calculate the coefficients of the distribution function expansion; (8) calculate the spin density (spin accumulation), spin current and spin-transfer torque using the distribution function. [4]

2.2.1 Approximations

The actual shape and/or size of the Fermi surface is not so important, as long as we allow different electrons to have different quasi-momentum vectors $\mathbf{k}$ in a Boltzmann equation calculation. Therefore, to simplify calculations, we assume that the Fermi surfaces in both the non-magnet and the ferromagnet (both spin up and spin-down) are the same and are perfectly spherical. We will use different mean free paths to distinguish the differences between the electrons in the non-magnet and the ferromagnet: l_{N} for non-magnet, $l_{\mathrm{F}}^{\uparrow,\downarrow}$ for spin-up and spin-down electrons in ferromagnet. Another commonly used approximation in Boltzmann equation studies is the relaxation-time approximation. We will use this also.

[3] Many of the results of this section were obtained by Dr. Mark Stiles (NIST) for a three-layer geometry. I confirmed his (unpublished) results and extended them to a five-layer geometry with new boundary conditions appropriate to the presence of reservoirs (see Figure 2.3 below).

[4] Spin accumulation is the spin density that deviates from its equilibrium value.

2.2.2 Matrix Distribution Function and Matrix Boltzmann Equation

The usual spin independent Boltzmann equation is

$$\mathbf{v_k} \cdot \frac{\partial f(\mathbf{r},\mathbf{k})}{\partial \mathbf{r}} - e\mathbf{E} \cdot \mathbf{v_k} = \int d\mathbf{k}' P_{\mathbf{k},\mathbf{k}'}[f(\mathbf{r},\mathbf{k}') - f(\mathbf{r},\mathbf{k})]. \tag{2.23}$$

where $f(\mathbf{r},\mathbf{k})$ is a spin independent distribution function, and $P_{\mathbf{k},\mathbf{k}'}$ is the probability that an electron scatters from $\mathbf{k}'$ to an empty state $\mathbf{k}$. The principle of microscopic reversibility tells us that $P_{\mathbf{k},\mathbf{k}'} = P_{\mathbf{k}',\mathbf{k}}$.

Matrix Distribution function

The spin valve structure contains ferromagnetic layers that are spin dependent. To use the Boltzmann equation in ferromagnetic materials, we generalize the distribution function and the Boltzmann equation to be spin dependent. First, the spin dependent distribution function is constructed in matrix form

$$\hat{f}(\mathbf{r},\mathbf{k}) = \begin{bmatrix} f^{\uparrow}(\mathbf{r},\mathbf{k}) & 0 \\ 0 & f^{\downarrow}(\mathbf{r},\mathbf{k}) \end{bmatrix} = f^{\uparrow}(\mathbf{r},\mathbf{k})\sigma_{\uparrow} + f^{\downarrow}(\mathbf{r},\mathbf{k})\sigma_{\downarrow} \quad \text{with} \quad \sigma_{\uparrow,\downarrow} = \frac{1}{2}(1 \pm \sigma_z). \tag{2.24}$$

Here, $(\sigma_x, \sigma_y, \sigma_z)$ are the Pauli matrices, and $f^{\uparrow,\downarrow}(\mathbf{r},\mathbf{k})$ describes the occupancy of spin-up and spin-down electrons in the phase space volume $d\mathbf{r}d\mathbf{k}$. If we choose a quantization axis other than the one that aligns to spin-up/down as in Eq. (2.24), the distribution function is generally written

$$\hat{f}(\mathbf{r},\mathbf{k}) = \hat{U} \begin{bmatrix} f^{\uparrow}(\mathbf{r},\mathbf{k}) & 0 \\ 0 & f^{\downarrow}(\mathbf{r},\mathbf{k}) \end{bmatrix} \hat{U}^{\dagger} = f^0 + f^x\sigma_x + f^y\sigma_y + f^z\sigma_z, \tag{2.25}$$

where U is the unitary rotation matrix

$$\hat{U}(\theta,\phi) = \begin{bmatrix} \cos(\theta/2)e^{-i\phi/2} & -\sin(\theta/2)e^{-i\phi/2} \\ \sin(\theta/2)e^{i\phi/2} & \cos(\theta/2)e^{i\phi/2} \end{bmatrix}. \tag{2.26}$$

θ and ϕ are the polar angle and azimuthal angle that describe the quantization axis. In all of our later discussions, we have $\phi = 0$, which means the magnetizations always lie in x-z

plane. In that case,

$$\hat{U}\begin{bmatrix}\sigma_0\\ \sigma_x\\ \sigma_y\\ \sigma_z\end{bmatrix}\hat{U}^\dagger = \begin{bmatrix}1 & 0 & 0 & 0\\ 0 & \cos\theta & 0 & -\sin\theta\\ 0 & 0 & 1 & 0\\ 0 & \sin\theta & 0 & \cos\theta\end{bmatrix}\begin{bmatrix}\sigma_0\\ \sigma_x\\ \sigma_y\\ \sigma_z\end{bmatrix}. \tag{2.27}$$

Consequently, the rotation of quantization axis transforms (ignoring the y component, since it won't appear in later calculations)

$$\begin{bmatrix}f^0\\ f^x\\ f^z\end{bmatrix} \longrightarrow \begin{bmatrix}f'^0\\ f'^x\\ f'^z\end{bmatrix} = \begin{bmatrix}1 & 0 & 0\\ 0 & \cos\theta & \sin\theta\\ 0 & -\sin\theta & \cos\theta\end{bmatrix}\begin{bmatrix}f^0\\ f^x\\ f^z\end{bmatrix} \equiv \hat{\mathbb{U}}\begin{bmatrix}f^0\\ f^x\\ f^z\end{bmatrix}. \tag{2.28}$$

Matrix Boltzmann Equation

Taking into account both spin-conserving scattering and spin flip scattering, the analog of the spin independent Boltzmann equation Eq. (2.23) for a spin dependent distribution function f^σ ($\sigma = \uparrow, \downarrow$) is

$$\mathbf{v}_\mathbf{k}\cdot\frac{\partial f^\sigma(\mathbf{k})}{\partial \mathbf{r}} - e\mathbf{E}\cdot\mathbf{v}_\mathbf{k} = \int d\mathbf{k}' P^\sigma_{\mathbf{k},\mathbf{k}'}[f^\sigma(\mathbf{k}') - f^\sigma(\mathbf{k})] + \int d\mathbf{k}' P^{\mathrm{sf}}_{\mathbf{k},\mathbf{k}'}[f^{\sigma'}(\mathbf{k}') - f^\sigma(\mathbf{k})]. \tag{2.29}$$

Similar to the definition of $P^\sigma_{\mathbf{k},\mathbf{k}'}$, $P^{\mathrm{sf}}_{\mathbf{k},\mathbf{k}'}$ is the probability that an electron scatters from $\mathbf{k}'$ to an empty state $\mathbf{k}$ but with spin-flip. We assume that the probability is the same for spin flip in both directions, up to down or down to up. Eq. (2.29) is used for both the non-magnetic bulk and the ferromagnetic bulk in the spin valve.

The Boltzmann equation is analytically solvable only in a few very limited cases; otherwise, we must rely on numerical solutions. The first thing we need for a numerical calculation is an angular mesh for the Fermi sphere. We define θ as the polar angle measured from the external electric field $\mathbf{E} = E\hat{\mathbf{x}}$, and ϕ is the azimuthal angle. [5] For perpendicular transport, transport properties are independent of the azimuthal angle ϕ, hence the integration of

[5] Here, the θ and ϕ are used to describe the angle on Fermi sphere, they are different from the θ and ϕ used before for the spin quantization axis, which is in spin space.

some transport property $h(\mathbf{k}) = h(\theta)$ over the Fermi sphere is [6]

$$\int_{\mathrm{FS}} h(\mathbf{k}) d\mathbf{k} = \int_0^{2\pi} d\phi \int_0^{\pi} h(\theta, \phi) \sin\theta d\theta = 2\pi \int_{-1}^{1} h(\mu) d\mu, \tag{2.30}$$

where we assume $k_F = 1$ and substitute $\mu = \cos\theta$. To discretize the integration in Eq. (2.30), we use Gauss-Legendre integration [27] with sampling poinst $\{\mu_i\}$ ($-1 \leq \mu_i \leq 1$) and weighting $\{w_i\}$, such that

$$\int_{-1}^{1} h(\mu) d\mu = \sum_{i=1}^{N} w_i h(\mu_i). \tag{2.31}$$

N is the number of sampling points. $\{w_i\}$ is the weighting when taking integrations over the Fermi sphere. $\{\mu_i\}$ is the angular mesh on the Fermi sphere. The half of the μ_i that are positive ($i = 1$ to $N/2$) are denoted by μ_i^+; the half that are negative ($i = N/2 + 1$ to N) are denoted by μ_i^-.

Since the external electric field is along $\hat{\mathbf{x}}$, $f^\sigma(\mathbf{r}, \mathbf{k}) = f^\sigma(x, k_x)$, and the Boltzmann equation Eq. (2.29) becomes

$$v_{\mathbf{k}}^x \frac{\partial}{\partial x} f^\sigma(k_x) - eE_x v_{\mathbf{k}}^x = \int d\mathbf{k}' P_{\mathbf{k},\mathbf{k}'}^\sigma [f^\sigma(k_x') - f^\sigma(k_x)] + \int d\mathbf{k}' P_{\mathbf{k},\mathbf{k}'}^{\mathrm{sf}} [f^{\sigma'}(k_x') - f^\sigma(k_x)]. \tag{2.32}$$

We use Eq. (2.31) to discretize the integrals in Eq. (2.32), *i.e.* $k_x \to \mu_i$, $k_x' \to \mu_j$ and $P_{\mathbf{k},\mathbf{k}'}^\sigma \to P_{ij}^\sigma$, etc. The discretized version of Boltzmann equation is

$$\frac{\partial f_i^\sigma}{\partial x} - eE_x = \sum_{j,\sigma'} [\hat{V}^{-1} \hat{B}]_{ij}^{\sigma\sigma'} f_j^{\sigma'}, \tag{2.33}$$

where $\hat{V}$ and $\hat{B}$ are $2N \times 2N$ (2 from spin index, N from μ_i index) matrices with matrix elements

$$V_{ij}^{\sigma\sigma'} = v_i^x \delta_{ij}^{\sigma\sigma'}, \tag{2.34a}$$

$$B_{ij}^{\sigma\sigma'} = w_j P_{ij}^\sigma \delta_{\sigma\sigma'} - \frac{\delta_{ij}^{\sigma\sigma'}}{\tau_i^\sigma} + w_j P_{ij}^{\mathrm{sf}} (1 - \delta_{\sigma\sigma'}) - \frac{\delta_{ij}^{\sigma\sigma'}}{\tau_i^{\mathrm{sf}}}, \tag{2.34b}$$

where $1/\tau_i^\sigma = \sum_j w_j P_{ij}^\sigma$, $1/\tau_i^{\mathrm{sf}} = \sum_j w_j P_{ij}^{\mathrm{sf}}$, and $\delta_{ij}^{\sigma\sigma'} = \delta_{ij}\delta_{\sigma\sigma'}$.

[6] To calculate spin density $h(\mathbf{k}) = f^\sigma(\mathbf{k})$, to calculate spin current $h(\mathbf{k}) = k_x f^\sigma(\mathbf{k})$.

2.2.3 Numerical Solutions to the Boltzmann Equation

The Appendix in Ref. [28] describes how to solve a Boltzmann equation like Eq. (2.33). Basically, one solves the particular equation,

$$\sum_{j,\sigma'} [\hat{V}^{-1}\hat{B}]_{ij}^{\sigma\sigma'} f_j^{\sigma'} = -eE_x, \tag{2.35}$$

and the homogeneous equation,

$$\sum_{j,\sigma'} \left\{ \delta_{ij}^{\sigma\sigma'} \frac{\partial}{\partial x} - [\hat{V}^{-1}\hat{B}]_{ij}^{\sigma\sigma'} \right\} f_j^{\sigma'} = 0. \tag{2.36}$$

Adding solutions to the particular and homogeneous equations, and assuming $P_{ij}^{\sigma} = P^{\sigma} = 1/\tau^{\sigma}$ and $P_{ij}^{\rm sf} = P^{\rm sf} = 1/\tau^{\rm sf}$ (relaxation time approximation),[7] the solutions for the distribution function have the form:

$$\hat{f}(x,\mu_i) = f^{\uparrow}\sigma_{\uparrow} + f^{\downarrow}\sigma_{\downarrow} \quad \text{with} \quad f^{\sigma} = \sum_{n=1}^{2N} \alpha_n F_n^{\sigma}(x,\mu_i) \qquad (\sigma = \uparrow, \downarrow), \tag{2.38}$$

where

$$\begin{aligned} &F_1^{\sigma}(x,\mu_i) = 1 \qquad \text{and} \qquad F_2^{\sigma}(x,\mu_i) = x - l^{\sigma}\mu_i, \\ &F_n^{\sigma}(x,\mu_i) = g_n^{\sigma}(\mu_i) e^{\lambda_n x} \quad \text{with} \quad n \in [3, 2N]. \end{aligned} \tag{2.39}$$

In the equation above, $l^{\sigma} = v_{\rm F}^{\sigma}\tau^{\sigma}$ is the mean free path for spin-up ($\sigma = \uparrow$) and spin-down ($\sigma = \downarrow$) electrons.[8] $g_n^{\sigma}(\mu_i) = g_n^{i\sigma}$ and λ_n are the n-th eigenvector and eigenvalue of $\hat{V}^{-1}\hat{B}$:[9]

$$\sum_{j,\sigma'} [\hat{V}^{-1}\hat{B}]_{i\sigma,j\sigma'} g_n^{j\sigma'} = \lambda_n g_n^{i\sigma}. \tag{2.40}$$

Half of the eigenvalues are positive; and the other half are negative. The $2N$ unknown coefficients α_n in Eq. (2.38) are to be determined (N unknowns for each of $f^{\uparrow}$ and $f^{\downarrow}$). We

[7] $\tau^{\rm sf}$ and τ^{σ} are related to spin diffusion length $l_{\rm sf}$ by $l_{\rm sf}^2 = D\tau_{\rm sf} = (v_F^2\tau/3)\tau_{\rm sf}$, therefore,

$$\tau^{\rm sf} = 3\frac{l_{\rm sf}^2}{v_F}\left(\frac{1}{l^{\uparrow}} + \frac{1}{l^{\downarrow}}\right) \quad \text{in FM} \quad \text{and} \quad \tau^{\rm sf} = 3\frac{l_{\rm sf}^2}{v_F}\frac{1}{l} \quad \text{in NM}, \tag{2.37}$$

where $l^{\sigma} = v_F\tau^{\sigma}$ and $l = v_F\tau$, $l_{\rm sf} = v_F\tau_{\rm sf}$.

[8] $v_{\rm F}^{\sigma}$ is the Fermi velocity for $\sigma = \uparrow$ or $\downarrow$ electrons. But in our calculation we chose the identical Fermi sphere for up and down electrons, so $v_{\rm F}^{\uparrow} = v_{\rm F}^{\downarrow}$. However, the mean free path for up and down electrons is still different.

[9] Notice the matrices $\hat{B}$ and $\hat{V}^{-1}\hat{B}$ are both asymmetric and singular, since $\sum_{j,\sigma'} B_{ij}^{\sigma\sigma'} = 0$. This leads to the eigenvectors F_0^{σ} and F_1^{σ} with zero eigenvalue being degenerate. See the Appendix in Ref. [28] for more details.

use Eq. (2.39) as the basis for the distribution functions in the ferromagnet, in which $f^{\uparrow,\downarrow}$ are used to represent the distribution function as in Eq. (2.24).

In the non-magnet layers, we use $f^{0,x,y,z}$ to represent the distribution function as in Eq. (2.25), so we can construct a different basis set for the non-magnet ($l^{\uparrow} = l^{\downarrow} = l$ in non-magnet):

$$F_n^0(x,\mu_i) = \frac{1}{2}[F_n^{\uparrow}(x,\mu_i) + F_n^{\downarrow}(x,\mu_i)] \qquad n \in [1,2N], \tag{2.41a}$$

$$F_n^z(x,\mu_i) = \frac{1}{2}[F_n^{\uparrow}(x,\mu_i) - F_n^{\downarrow}(x,\mu_i)] \qquad n \in [1,2N], \tag{2.41b}$$

$$F_n^x(x,\mu_i) = F_n^z(x,\mu_i) \qquad n \in [1,2N]. \tag{2.41c}$$

Therefore, in the non-magnet layers (especially in the spacer layer), the general solution for distribution function is

$$\hat{f}(x,\mu_i) = f^0\sigma_0 + f^x\sigma_x + f^z\sigma_z \quad \text{with} \quad f^s = \sum_{n=1}^{2N} \alpha_n^s F_n^s(x,\mu_i) \quad (s = 0,x,z). \tag{2.42}$$

Eq. (2.41) tells us that f^x and f^z share the same set of eigenvectors. This is reasonable because the Boltzmann solution does not depend on the choice of spin quantization axis, which also implies that f^x, f^z, $f^{x'}$, and $f^{z'}$ all share the same set of eigenvectors.

At first glance, Eq. (2.42) doubles the number of unknown coefficients in the expansion: $2N$ instead of N for each of f^0, f^x, and f^z. But it is not the case because of the following: The eigenvectors $F_n^{\sigma}(x,\mu_i)$ break up into separate eigenvectors for charge transport and spin transport, for instance the eigenvectors with $n = 1$ and 2 correspond to charge transport because $F_{1,2}^{\uparrow} = F_{1,2}^{\downarrow}$. In general, half of the eigenvectors (assume for the first half: $n \in [1,N]$) corresponds to the charge transport with $F_n^{\uparrow} = F_n^{\downarrow}$, the other half (for the second half: $n \in [N+1,2N]$) is for the spin transport with $F_n^{\uparrow} = -F_n^{\downarrow}$. This fact implies that

$$F_n^0(x,\mu_i) = 0 \quad \text{for} \quad n \in [N+1,2N], \tag{2.43a}$$

$$F_n^x(x,\mu_i) = F_n^z(x,\mu_i) = 0 \quad \text{for} \quad n \in [1,N]. \tag{2.43b}$$

Therefore, we still have exactly N unknown coefficients for each of f^0, f^x, and f^z.

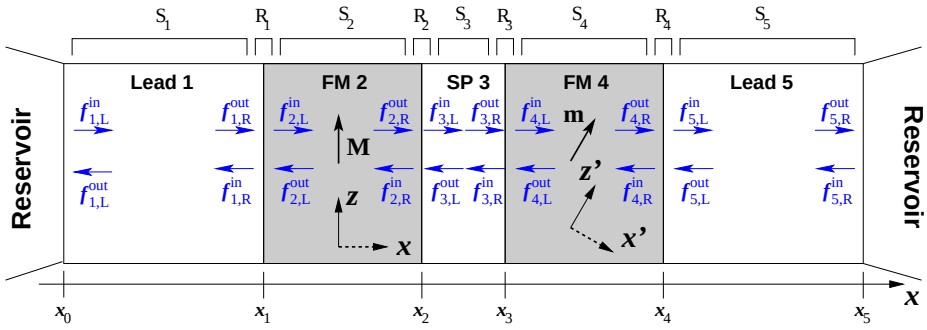

Figure 2.3: Schematic view of spin valve structure.

2.2.4 Layer Scattering Matrix

Figure 2.3 shows a schematic picture of a spin valve, where lead/FM/spacer/FM/lead are labeled by layer 1 to layer 5, and $x_{0,1,2,3,4,5}$ denotes the x coordinate of each interface. In the ferromagnetic layers (layer 2 and layer 4), we choose the magnetization direction (z-direction in layer 2 and z' in layer 4) as the natural spin quantization axis, *i.e.* $\hat{f} = f^{\uparrow}\sigma_{\uparrow} + f^{\downarrow}\sigma_{\downarrow}$ for layer 2, and $\hat{f} = f^{\uparrow'}\sigma_{\uparrow'} + f^{\downarrow'}\sigma_{\downarrow'}$ for layer 4. [10]

For non-magnetic layers, there is no spontaneous magnetization to keep the electron spin aligned to some axis. Therefore, we write $\hat{f} = f^0\sigma_0 + f^x\sigma_x + f^z\sigma_z$ in the non-magnetic layers. The σ_y term does not appear because the magnetizations of the FM layers are confined to the x-z plane. Since the magnetization of layer 2 is along z and layer 1 is connected to layer 2, the natural spin quantization axis in layer 1 is chosen as the z axis. Hence, there is no σ_x term in the distribution function in layer 1. Similarly, there is no $\sigma_{x'}$ term in layer 5. The spacer layer (layer 3) connects to two non-collinear FM layers, the natural quantization direction varies along x, so the distribution function in the spacer layer has both σ_x and σ_z terms.

We now focus on the values of the distribution functions near each interface. These are denoted by $f^{\text{in/out}}_{\text{m,L/R}}$ in Figure 2.3. These are evaluated inside the m-th layer at its left(L)/right(R) edge [11] for electrons moving into/out-of layer m. The unprimed ($f^{\text{in/out}}_{\text{m,L/R}}$) and the primed ($f^{\text{in/out}'}_{\text{m,L/R}}$) versions mean the distribution functions using z and z' as the

[10] $\uparrow$ and $\downarrow$ denote the up and down relative to z, $\uparrow'$ and $\downarrow'$ denote the up and down relative to z'.
[11] Evaluated at $x^{+}_{\text{m}-1}$ and x^{-}_{m}, where $x^{\pm}_{m}$ denotes the immediate vicinity at right(+)/left(-) side of x_m.

spin quantization axes respectively. We use the unprimed version for layer 1 and 2, and the primed version for layers 3, 4, and 5 (see Figure 2.3). However, layer 3 uses both depending on which side it attaches to in the calculation. Since we expand the distribution function differently in ferromagnetic and non-magnetic layers, $f^{\text{in/out}}_{\text{m,L/R}}$ takes different forms in them:

ferromagnet (m = 2, 4)	non-magnet (m = 1, 3, 5)
$f^{\text{in/out}}_{\text{m,L/R}} = \begin{bmatrix} f^{\text{in/out},\uparrow}_{\text{m,L/R}} \\ f^{\text{in/out},\downarrow}_{\text{m,L/R}} \end{bmatrix}$	$f^{\text{in/out}}_{\text{m,L/R}} = \begin{bmatrix} f^{\text{in/out,0}}_{\text{m,L/R}} \\ f^{\text{in/out,x}}_{\text{m,L/R}} \\ f^{\text{in/out,z}}_{\text{m,L/R}} \end{bmatrix}$.

(2.44)

What we want to calculate next is the layer scattering matrix S_{m} that relates the incoming and outgoing distribution functions for layer m:

$$\begin{bmatrix} f^{\text{out}}_{\text{m,L}} \\ f^{\text{out}}_{\text{m,R}} \end{bmatrix} = \begin{bmatrix} S^{\text{LL}}_{\text{m}} & S^{\text{LR}}_{\text{m}} \\ S^{\text{RL}}_{\text{m}} & S^{\text{RR}}_{\text{m}} \end{bmatrix} \begin{bmatrix} f^{\text{in}}_{\text{m,L}} \\ f^{\text{in}}_{\text{m,R}} \end{bmatrix} \equiv S_{\text{m}} \begin{bmatrix} f^{\text{in}}_{\text{m,L}} \\ f^{\text{in}}_{\text{m,R}} \end{bmatrix}, \tag{2.45}$$

S^{LR}_{m} accounts for the scattering from the right side to the left side of the layer (from $f^{\text{in}}_{\text{m,R}}$ to $f^{\text{out}}_{\text{m,L}}$).

S_{m} for Ferromagnetic Layers (m = 2, 4)

For the left FM layer (m = 2), using the solutions in Eq. (2.38), we have,

$$\begin{bmatrix} f^{\text{in}}_{2,\text{L}} \\ f^{\text{in}}_{2,\text{R}} \end{bmatrix} = \begin{bmatrix} f^{\uparrow}_{2,\text{L}}(\mu_i^+) \\ f^{\downarrow}_{2,\text{L}}(\mu_i^+) \\ f^{\uparrow}_{2,\text{R}}(\mu_i^-) \\ f^{\downarrow}_{2,\text{R}}(\mu_i^-) \end{bmatrix} = \begin{bmatrix} F^{\uparrow}_1(x_1,\mu_i^+) & \cdots & F^{\uparrow}_{2N}(x_1,\mu_i^+) \\ F^{\downarrow}_1(x_1,\mu_i^+) & \cdots & F^{\downarrow}_{2N}(x_1,\mu_i^+) \\ F^{\uparrow}_1(x_2,\mu_i^-) & \cdots & F^{\uparrow}_{2N}(x_2,\mu_i^-) \\ F^{\downarrow}_1(x_2,\mu_i^-) & \cdots & F^{\downarrow}_{2N}(x_2,\mu_i^-) \end{bmatrix} \begin{bmatrix} \alpha_1 \\ \alpha_2 \\ \vdots \\ \alpha_{2N} \end{bmatrix}, \tag{2.46a}$$

$$\begin{bmatrix} f^{\text{out}}_{2,\text{L}} \\ f^{\text{out}}_{2,\text{R}} \end{bmatrix} = \begin{bmatrix} f^{\uparrow}_{2,\text{L}}(\mu_i^-) \\ f^{\downarrow}_{2,\text{L}}(\mu_i^-) \\ f^{\uparrow}_{2,\text{R}}(\mu_i^+) \\ f^{\downarrow}_{2,\text{R}}(\mu_i^+) \end{bmatrix} = \begin{bmatrix} F^{\uparrow}_1(x_1,\mu_i^-) & \cdots & F^{\uparrow}_{2N}(x_1,\mu_i^-) \\ F^{\downarrow}_1(x_1,\mu_i^-) & \cdots & F^{\downarrow}_{2N}(x_1,\mu_i^-) \\ F^{\uparrow}_1(x_2,\mu_i^+) & \cdots & F^{\uparrow}_{2N}(x_2,\mu_i^+) \\ F^{\downarrow}_1(x_2,\mu_i^+) & \cdots & F^{\downarrow}_{2N}(x_2,\mu_i^+) \end{bmatrix} \begin{bmatrix} \alpha_1 \\ \alpha_2 \\ \vdots \\ \alpha_{2N} \end{bmatrix}. \tag{2.46b}$$

As we defined previously $\mu_i^{\pm}$ denotes $\mu_i > 0$ and $\mu_i < 0$, or right going and left going

wave-vectors. By canceling α_n's in the equation above, we get the layer scattering matrix

$$S_2 = \begin{bmatrix} F_1^{\uparrow}(x_1,\mu_i^-) & \cdots & F_{2N}^{\uparrow}(x_1,\mu_i^-) \\ F_1^{\downarrow}(x_1,\mu_i^-) & \cdots & F_{2N}^{\downarrow}(x_1,\mu_i^-) \\ F_1^{\uparrow}(x_2,\mu_i^+) & \cdots & F_{2N}^{\uparrow}(x_2,\mu_i^+) \\ F_1^{\downarrow}(x_2,\mu_i^+) & \cdots & F_{2N}^{\downarrow}(x_2,\mu_i^+) \end{bmatrix} \begin{bmatrix} F_1^{\uparrow}(x_1,\mu_i^+) & \cdots & F_{2N}^{\uparrow}(x_1,\mu_i^+) \\ F_1^{\downarrow}(x_1,\mu_i^+) & \cdots & F_{2N}^{\downarrow}(x_1,\mu_i^+) \\ F_1^{\uparrow}(x_2,\mu_i^-) & \cdots & F_{2N}^{\uparrow}(x_2,\mu_i^-) \\ F_1^{\downarrow}(x_2,\mu_i^-) & \cdots & F_{2N}^{\downarrow}(x_2,\mu_i^-) \end{bmatrix}^{-1} . \quad (2.47)$$

The layer scattering matrix for the right ferromagnet S_4 (m = 4) is obtained similarly by replacing $[x_1, x_2] \to [x_3, x_4]$. For ferromagnetic layers (m = 2, 4), since each element like $F_n^{\uparrow}(x_1, \mu_i^+)$ is a $1 \times \frac{N}{2}$ matrix, the layer scattering matrix $S_{\rm m}$ is a $2N \times 2N$ matrix. It is worth mentioning that the scattering matrix is independent of the choice of the origin for x, so we choose $x_1 = 0$ when calculating S_2 and choose $x_3 = 0$ when calculating S_4. [12]

$S_{\rm m}$ for Non-magnetic Layers (m = 1, 3, 5)

For the left lead (m = 1), using the solutions in Eq. (2.42), we have

$$\begin{bmatrix} f_{1,\rm L}^{\rm in} \\ f_{1,\rm R}^{\rm in} \end{bmatrix} = \begin{bmatrix} f_{1,\rm L}^{0}(\mu_i^+) \\ f_{1,\rm L}^{x}(\mu_i^+) \\ f_{1,\rm L}^{z}(\mu_i^+) \\ f_{1,\rm R}^{0}(\mu_i^-) \\ f_{1,\rm R}^{x}(\mu_i^-) \\ f_{1,\rm R}^{z}(\mu_i^-) \end{bmatrix} = \begin{bmatrix} F_n^0(x_0,\mu_i^+) & 0 & 0 \\ 0 & F_{n'}^x(x_0,\mu_i^+) & 0 \\ 0 & 0 & F_{n'}^z(x_0,\mu_i^+) \\ F_n^0(x_1,\mu_i^-) & 0 & 0 \\ 0 & F_{n'}^x(x_1,\mu_i^-) & 0 \\ 0 & 0 & F_{n'}^z(x_1,\mu_i^-) \end{bmatrix} \begin{bmatrix} \alpha_n^0 \\ \alpha_{n'}^x \\ \alpha_{n'}^z \end{bmatrix}, \quad (2.48a)$$

$$\begin{bmatrix} f_{1,\rm L}^{\rm out} \\ f_{1,\rm R}^{\rm out} \end{bmatrix} = \begin{bmatrix} f_{1,\rm L}^{0}(\mu_i^-) \\ f_{1,\rm L}^{x}(\mu_i^-) \\ f_{1,\rm L}^{z}(\mu_i^-) \\ f_{1,\rm R}^{0}(\mu_i^+) \\ f_{1,\rm R}^{x}(\mu_i^+) \\ f_{1,\rm R}^{z}(\mu_i^+) \end{bmatrix} = \begin{bmatrix} F_n^0(x_0,\mu_i^-) & 0 & 0 \\ 0 & F_{n'}^x(x_0,\mu_i^-) & 0 \\ 0 & 0 & F_{n'}^z(x_0,\mu_i^-) \\ F_n^0(x_1,\mu_i^+) & 0 & 0 \\ 0 & F_{n'}^x(x_1,\mu_i^+) & 0 \\ 0 & 0 & F_{n'}^z(x_1,\mu_i^+) \end{bmatrix} \begin{bmatrix} \alpha_n^0 \\ \alpha_{n'}^x \\ \alpha_{n'}^z \end{bmatrix}, \quad (2.48b)$$

where n runs from 1 to N and n' runs from $N+1$ to $2N$. We omit the zero eigenvectors due to Eq. (2.43). By canceling α_n's in the equation above, we have the $3N \times 3N$ layer

[12] μ_i^+ runs from $i = 1$ to $i = N/2$ and μ_i^- runs from $i = N/2 + 1$ to $i = N$.

scattering matrix:

$$S_1 = \begin{bmatrix} F_n^0(x_0,\mu_i^-) & 0 & 0 \\ 0 & F_{n'}^x(x_0,\mu_i^-) & 0 \\ 0 & 0 & F_{n'}^z(x_0,\mu_i^-) \\ F_n^0(x_1,\mu_i^+) & 0 & 0 \\ 0 & F_{n'}^x(x_1,\mu_i^+) & 0 \\ 0 & 0 & F_{n'}^z(x_1,\mu_i^+) \end{bmatrix} \begin{bmatrix} F_n^0(x_0,\mu_i^+) & 0 & 0 \\ 0 & F_{n'}^x(x_0,\mu_i^+) & 0 \\ 0 & 0 & F_{n'}^z(x_0,\mu_i^+) \\ F_n^0(x_1,\mu_i^-) & 0 & 0 \\ 0 & F_{n'}^x(x_1,\mu_i^-) & 0 \\ 0 & 0 & F_{n'}^z(x_1,\mu_i^-) \end{bmatrix}^{-1}. \tag{2.49}$$

The layer scattering matrix for the spacer layer S_3 (m = 3) and the right lead S_5 (m = 5) are obtained similarly by replacing $[x_0, x_1] \to [x_2, x_3]$ and $[x_0, x_1] \to [x_4, x_5]$. For the non-magnetic layers (m = 1, 3, 5), the layer scattering matrix $S_{\rm m}$ is a $3N \times 3N$ matrix.

2.2.5 Interface Scattering Matrix

Similar to the layer scattering matrix, the interface scattering matrix $R_{\rm m}$ relates the outgoing and the incoming distribution functions at the interface between layer m and layer m+1: [13]

$$\begin{bmatrix} f_{\rm m,R}^{\rm in} \\ f_{\rm m+1,L}^{\rm in} \end{bmatrix} = \begin{bmatrix} R_{\rm m}^{\rm LL} & R_{\rm m}^{\rm LR} \\ R_{\rm m}^{\rm RL} & R_{\rm m}^{\rm RR} \end{bmatrix} \begin{bmatrix} f_{\rm m,R}^{\rm out} \\ f_{\rm m+1,L}^{\rm out} \end{bmatrix} = R_{\rm m} \begin{bmatrix} f_{\rm m,R}^{\rm out} \\ f_{\rm m+1,L}^{\rm out} \end{bmatrix}. \tag{2.50}$$

$R_{\rm m}^{\rm LR}$ accounts for the scattering from the right side to the left side of the interface (from $f_{\rm m+1,L}^{\rm out}$ to $f_{\rm m,R}^{\rm in}$).

All the interfaces in our problem are non-magnet/ferromagnet interfaces, so we consider the interface shown in Figure 2.4. Suppose there is an electron with a longitudinal wave-vector $k_x = \mu_i$ injected from the non-magnet (N) side onto the interface. If its wave-function is

$$|\phi_{\rm N}^{\rm out}(\mu_i)\rangle = \begin{bmatrix} a(\mu_i) \\ b(\mu_i) \end{bmatrix}, \tag{2.51}$$

the wave-functions for the reflected state (with $k_x = -\mu_i$) in the non-magnet and for the

[13] Notice the incoming and outgoing relative to the interface are opposite to the incoming and outgoing relative to the layers.

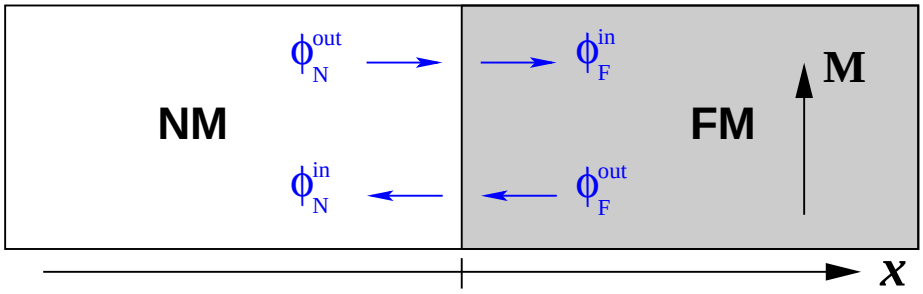

Figure 2.4: Wave functions at a non-magnet/ferromagnet interface.

transmitted state (with $k_x = \mu_i$) in the ferromagnet are [14]

$$|\phi_{\rm N}^{\rm in}(-\mu_i)\rangle = \hat{R}_{\rm NN}(\mu_i)|\phi_{\rm N}^{\rm out}(\mu_i)\rangle \qquad \text{and} \qquad |\phi_{\rm F}^{\rm in}(\mu_i)\rangle = \hat{T}_{\rm NF}(\mu_i)|\phi_{\rm N}^{\rm out}(\mu_i)\rangle, \tag{2.52}$$

where $\hat{R}_{\rm NN}$ and $\hat{T}_{\rm NF}$ are reflection and transmission scattering matrices:

$$\hat{R}_{\rm NN}(\mu_i) = \begin{bmatrix} R_{\rm NN}^{\uparrow}(\mu_i) & 0 \\ 0 & R_{\rm NN}^{\downarrow}(\mu_i) \end{bmatrix} \quad \text{and} \quad \hat{T}_{\rm NF}(\mu_i) = \begin{bmatrix} T_{\rm NF}^{\uparrow}(\mu_i) & 0 \\ 0 & T_{\rm NF}^{\downarrow}(\mu_i) \end{bmatrix}. \tag{2.53}$$

The off-diagonal elements in these scattering matrices are zero, because we assume there is no spin flip scattering at the interface. [15] The subscript in $\hat{R}_{\rm NN}$ means the reflection is from non-magnet (N) to non-magnet (N), and in $\hat{T}_{\rm NF}$ it means the transmission is from non-magnet (N) to ferromagnet (F). We define $\hat{R}_{\rm FF}$ and $\hat{T}_{\rm FN}$ in the same way. Due to the conservation law, these scattering matrices satisfy

$$\hat{R}_{\rm NN}\hat{R}_{\rm NN}^{\dagger} + \hat{T}_{\rm NF}\hat{T}_{\rm NF}^{\dagger} = \hat{I} \qquad \text{and} \qquad \hat{R}_{\rm FF}\hat{R}_{\rm FF}^{\dagger} + \hat{T}_{\rm FN}\hat{T}_{\rm FN}^{\dagger} = \hat{I}. \tag{2.54}$$

The matrix elements in $\hat{R}$'s and $\hat{T}$'s are calculated in Ref. [29]:

$$|T_{\rm NF}^{\sigma}(\mu_i)|^2 = |T_{\rm FN}^{\sigma}(\mu_i)|^2 = \frac{\mu_i^2}{\alpha_\sigma + \mu_i^2} \quad \text{and} \quad |R_{\rm NN}^{\sigma}(\mu_i)|^2 = |R_{\rm FF}^{\sigma}(\mu_i)|^2 = \frac{\alpha_\sigma}{\alpha_\sigma + \mu_i^2}, \tag{2.55}$$

where $\sigma = \uparrow$ or $\downarrow$, and the dimensionless number α_σ is proportional to the square root of the strength of the δ-function like interface potential, which can be read off from the horizontal axis of Fig. 1 of Ref. [29] using experimental spin dependent interface resistance data.

[14] We've made the approximation that the transmitted state has the same transverse and longitudinal wave-vector $(\mathbf{k}_\perp, k_x)$ in the ferromagnet as in the non-magnet because in the previous subsection we assumed that electrons at both sides of the interface have the same Fermi surface. This approximation is good as long as the interfaces are not too close to each other.

[15] Because the spin flip scattering is mainly due to spin-orbit interaction. And at an interface, the situation that a spin encounters is a discontinuity of the Fermi levels from one side to the other. Therefore, we assume there is no spin flip scattering at the interface.

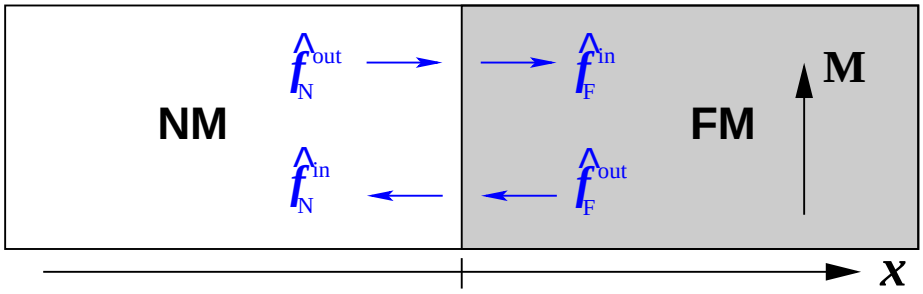

Figure 2.5: Distribution functions at a non-magnet/ferromagnet interface.

Using the wave-functions, we can construct the corresponding distribution functions depicted in Figure 2.5 by using a density matrix:

$$\hat{f}_{\rm N}^{\rm out}(\mu_i) = |\phi_{\rm N}^{\rm out}\rangle\langle\phi_{\rm N}^{\rm out}|, \qquad \hat{f}_{\rm N}^{\rm in}(-\mu_i) = |\phi_{\rm N}^{\rm in}\rangle\langle\phi_{\rm N}^{\rm in}|, \quad \text{and} \quad \hat{f}_{\rm F}^{\rm in}(\mu_i) = |\phi_{\rm F}^{\rm in}\rangle\langle\phi_{\rm F}^{\rm in}|. \tag{2.56}$$

From Eq. (2.52), it is easy to check that

$$\hat{f}_{\rm N}^{\rm in} = \hat{R}_{\rm NN}\hat{f}_{\rm N}^{\rm out}\hat{R}_{\rm NN}^{\dagger}, \qquad \text{and} \qquad \hat{f}_{\rm F}^{\rm in} = \hat{T}_{\rm NF}\hat{f}_{\rm N}^{\rm out}\hat{T}_{\rm NF}^{\dagger}. \tag{2.57}$$

Similarly, if we start with an incoming electron from the FM side, we will have

$$\hat{f}_{\rm F}^{\rm in} = \hat{R}_{\rm FF}\hat{f}_{\rm F}^{\rm out}\hat{R}_{\rm FF}^{\dagger}, \qquad \text{and} \qquad \hat{f}_{\rm N}^{\rm in} = \hat{T}_{\rm FN}\hat{f}_{\rm F}^{\rm out}\hat{T}_{\rm FN}^{\dagger}. \tag{2.58}$$

Since the electrons are injected from both sides, we combine Eq. (2.57) and Eq. (2.58) to get

$$\hat{f}_{\rm N}^{\rm in} = \hat{R}_{\rm NN}\hat{f}_{\rm N}^{\rm out}\hat{R}_{\rm NN}^{\dagger} + \hat{T}_{\rm FN}\hat{f}_{\rm F}^{\rm out}\hat{T}_{\rm FN}^{\dagger}, \quad \text{and} \quad \hat{f}_{\rm F}^{\rm in} = \hat{T}_{\rm NF}\hat{f}_{\rm N}^{\rm out}\hat{T}_{\rm NF}^{\dagger} + \hat{R}_{\rm FF}\hat{f}_{\rm F}^{\rm out}\hat{R}_{\rm FF}^{\dagger}. \tag{2.59}$$

By expanding all the $\hat{f}$'s above using Pauli matrices as in Eq. (2.25), we can rewrite Eq. (2.59) in terms of $f^{0,x,y,z}$. But before that, we need the following identity (let $\hat{X}$ be any one of $\hat{R}_{\rm NN}$, $\hat{R}_{\rm FF}$, $\hat{T}_{\rm NF}$, and $\hat{T}_{\rm FN}$, and let $\sigma_1 = \sigma_x$, $\sigma_2 = \sigma_y$, and $\sigma_3 = \sigma_z$):

$$\hat{X}\sigma_i\hat{X}^{\dagger} = \sum_{j=0}^{3} \mathbb{X}_i^j\sigma_j \qquad \text{with} \qquad (i = 0, 1, 2, 3), \tag{2.60}$$

where

$$\mathbb{X} = \begin{bmatrix} X^{\Pi}(\mu_i) & 0 & 0 & X^{\Delta}(\mu_i) \\ 0 & X^{\perp}(\mu_i) & -X^{\times}(\mu_i) & 0 \\ 0 & X^{\times}(\mu_i) & X^{\perp}(\mu_i) & 0 \\ X^{\Delta}(\mu_i) & 0 & 0 & X^{\Pi}(\mu_i) \end{bmatrix}, \tag{2.61}$$

with

$$X^{\Pi}(\mu_i) = \frac{1}{2}[|X_\uparrow(\mu_i)|^2 + |X_\downarrow(\mu_i)|^2], \quad X^{\perp}(\mu_i) = \mathrm{Re}[X_\uparrow(\mu_i)X_\downarrow^*(\mu_i)] \simeq 0,$$
$$X^{\Delta}(\mu_i) = \frac{1}{2}[|X_\uparrow(\mu_i)|^2 - |X_\downarrow(\mu_i)|^2], \quad X^{\times}(\mu_i) = \mathrm{Im}[X_\uparrow(\mu_i)X_\downarrow^*(\mu_i)] \simeq 0. \tag{2.62}$$

In the ferromagnet, the transverse component of the distribution function is ignored, [16] so $f_{\rm F}^{x,y} = 0$ ($f_{\rm F}^{x',y'} = 0$ if the magnetization aligns z' axis). We also ignore the y component in the non-magnet, since the magnetization of the FM layer is always in the x-z plane. By using the orthogonality between the σ_i's, Eq. (2.59) can be written in terms of $f^{0,x,y,z}$ in the non-magnet and in terms of $f^{\uparrow,\downarrow}$ in the ferromagnet as: [17].

$$\begin{bmatrix} f_{\rm N}^0(\mu_i^-) \\ f_{\rm N}^x(\mu_i^-) \\ f_{\rm N}^z(\mu_i^-) \\ f_{\rm F}^\uparrow(\mu_i^+) \\ f_{\rm F}^\downarrow(\mu_i^+) \end{bmatrix} = \left[\begin{array}{ccc|cc} R_{\rm NN}^{\Pi} & 0 & R_{\rm NN}^{\Delta} & \frac{1}{2}|T_{\rm FN}^\uparrow|^2 & \frac{1}{2}|T_{\rm FN}^\downarrow|^2 \\ 0 & R_{\rm NN}^{\perp} & 0 & 0 & 0 \\ R_{\rm NN}^{\Delta} & 0 & R_{\rm NN}^{\Pi} & \frac{1}{2}|T_{\rm FN}^\uparrow|^2 & -\frac{1}{2}|T_{\rm FN}^\downarrow|^2 \\ \hline |T_{\rm NF}^\uparrow|^2 & 0 & |T_{\rm NF}^\uparrow|^2 & |R_{\rm FF}^\uparrow|^2 & 0 \\ |T_{\rm NF}^\downarrow|^2 & 0 & -|T_{\rm NF}^\downarrow|^2 & 0 & |R_{\rm FF}^\downarrow|^2 \end{array}\right] \begin{bmatrix} f_{\rm N}^0(\mu_i^+) \\ f_{\rm N}^x(\mu_i^+) \\ f_{\rm N}^z(\mu_i^+) \\ f_{\rm F}^\uparrow(\mu_i^-) \\ f_{\rm F}^\downarrow(\mu_i^-) \end{bmatrix}. \tag{2.63}$$

If the FM layer is on the left side of the NM layer, we should make some appropriate rearrangement of the rows and columns in Eq. (2.63):

$$\begin{bmatrix} f_{\rm F}^\uparrow(\mu_i^-) \\ f_{\rm F}^\downarrow(\mu_i^-) \\ f_{\rm N}^0(\mu_i^+) \\ f_{\rm N}^x(\mu_i^+) \\ f_{\rm N}^z(\mu_i^+) \end{bmatrix} = \left[\begin{array}{cc|ccc} |R_{\rm FF}^\uparrow|^2 & 0 & |T_{\rm NF}^\uparrow|^2 & 0 & |T_{\rm NF}^\uparrow|^2 \\ 0 & |R_{\rm FF}^\downarrow|^2 & |T_{\rm NF}^\downarrow|^2 & 0 & -|T_{\rm NF}^\downarrow|^2 \\ \hline \frac{1}{2}|T_{\rm FN}^\uparrow|^2 & \frac{1}{2}|T_{\rm FN}^\downarrow|^2 & R_{\rm NN}^{\Pi} & 0 & R_{\rm NN}^{\Delta} \\ 0 & 0 & 0 & R_{\rm NN}^{\perp} & 0 \\ \frac{1}{2}|T_{\rm FN}^\uparrow|^2 & -\frac{1}{2}|T_{\rm FN}^\downarrow|^2 & R_{\rm NN}^{\Delta} & 0 & R_{\rm NN}^{\Pi} \end{array}\right] \begin{bmatrix} f_{\rm F}^\uparrow(\mu_i^+) \\ f_{\rm F}^\downarrow(\mu_i^+) \\ f_{\rm N}^0(\mu_i^-) \\ f_{\rm N}^x(\mu_i^-) \\ f_{\rm N}^z(\mu_i^-) \end{bmatrix}. \tag{2.64}$$

All quantities in these equations are μ_i dependent. If we expand the μ_i index, the matrix on the LHS has dimension $\frac{5}{2}N \times 1$, and the matrices on the RHS have dimensions $\frac{5}{2}N \times \frac{5}{2}N$

[16] If there is any transverse component, it disappears due to the damping towards the magnetization of the ferromagnet [8].

[17] We need to make linear combinations: $f_{\rm F}^\uparrow = f_{\rm F}^0 + f_{\rm F}^z$ and $f_{\rm F}^\downarrow = f_{\rm F}^0 - f_{\rm F}^z$, and make the replacements like $f_{\rm N}^{{\rm in},0} \to f_{\rm N}^0(\mu_i^-)$

and $\frac{5}{2}N \times 1$. Each element like R^{Π}_{NN} becomes a $\frac{1}{2}N \times \frac{1}{2}N$ matrix:

$$R^{\Pi}_{\mathrm{NN}} = \begin{bmatrix} R^{\Pi}_{\mathrm{NN}}(\mu_1) & 0 & \cdots & 0 \\ 0 & R^{\Pi}_{\mathrm{NN}}(\mu_2) & \cdots & 0 \\ \vdots & \vdots & \vdots & \vdots \\ 0 & 0 & \cdots & R^{\Pi}_{\mathrm{NN}}(\mu_{\frac{N}{2}}) \end{bmatrix}. \tag{2.65}$$

Similar expansion can be made for other R's and T's.

From Eq. (2.63) we have the interface scattering matrices for the NM/FM type interfaces at x_1 and x_3 and for FM/NM type interfaces at x_2 and x_4,

$$R_3 = R_1 = \left[\begin{array}{c|c} R^{\mathrm{LL}}_1 & R^{\mathrm{LR}}_1 \\ \hline R^{\mathrm{RL}}_1 & R^{\mathrm{RR}}_1 \end{array}\right] = \left[\begin{array}{ccc|cc} R^{\Pi}_{\mathrm{NN}} & 0 & R^{\Delta}_{\mathrm{NN}} & \frac{1}{2}|T^{\uparrow}_{\mathrm{FN}}|^2 & \frac{1}{2}|T^{\downarrow}_{\mathrm{FN}}|^2 \\ 0 & R^{\perp}_{\mathrm{NN}} & 0 & 0 & 0 \\ R^{\Delta}_{\mathrm{NN}} & 0 & R^{\Pi}_{\mathrm{NN}} & \frac{1}{2}|T^{\uparrow}_{\mathrm{FN}}|^2 & -\frac{1}{2}|T^{\downarrow}_{\mathrm{FN}}|^2 \\ \hline |T^{\uparrow}_{\mathrm{NF}}|^2 & 0 & |T^{\uparrow}_{\mathrm{NF}}|^2 & |R^{\uparrow}_{\mathrm{FF}}|^2 & 0 \\ |T^{\downarrow}_{\mathrm{NF}}|^2 & 0 & -|T^{\downarrow}_{\mathrm{NF}}|^2 & 0 & |R^{\downarrow}_{\mathrm{FF}}|^2 \end{array}\right], \tag{2.66a}$$

$$R_4 = R_2 = \left[\begin{array}{c|c} R^{\mathrm{LL}}_2 & R^{\mathrm{LR}}_2 \\ \hline R^{\mathrm{RL}}_2 & R^{\mathrm{RR}}_2 \end{array}\right] = \left[\begin{array}{cc|ccc} |R^{\uparrow}_{\mathrm{FF}}|^2 & 0 & |T^{\uparrow}_{\mathrm{NF}}|^2 & 0 & |T^{\uparrow}_{\mathrm{NF}}|^2 \\ 0 & |R^{\downarrow}_{\mathrm{FF}}|^2 & |T^{\downarrow}_{\mathrm{NF}}|^2 & 0 & -|T^{\downarrow}_{\mathrm{NF}}|^2 \\ \hline \frac{1}{2}|T^{\uparrow}_{\mathrm{FN}}|^2 & \frac{1}{2}|T^{\downarrow}_{\mathrm{FN}}|^2 & R^{\Pi}_{\mathrm{NN}} & 0 & R^{\Delta}_{\mathrm{NN}} \\ 0 & 0 & 0 & R^{\perp}_{\mathrm{NN}} & 0 \\ \frac{1}{2}|T^{\uparrow}_{\mathrm{FN}}|^2 & -\frac{1}{2}|T^{\downarrow}_{\mathrm{FN}}|^2 & R^{\Delta}_{\mathrm{NN}} & 0 & R^{\Pi}_{\mathrm{NN}} \end{array}\right]. \tag{2.66b}$$

2.2.6 System Scattering Matrix

We now have all the layer and interface scattering matrices $S_{1,2,3,4,5}$ and $R_{1,2,3,4}$ as indicated at the top of Figure 2.3, so we are ready to construct a system-wide scattering matrix that relates the incoming and outgoing distribution functions at the left and right reservoir. The system scattering matrix is obtained by joining all the layer scattering matrices and interface scattering matrices. But when joining the matrices, we must be careful at the spacer layer, because the scattering matrices on the left and right side of the spacer layer use different spin quantization directions: left side uses z, right side uses z'. So we make a rotation at the spacer layer to match the quantization axis at two sides.

The scattering matrix joining procedure is follows. First we join S_1 to R_1 (see Figure 2.3). S_1 is a $3N \times 3N$ matrix, and relates the distribution functions:

$$\begin{bmatrix} f_{1,\mathrm{L}}^{\mathrm{out}} \\ f_{1,\mathrm{R}}^{\mathrm{out}} \end{bmatrix} = \begin{bmatrix} S_1^{\mathrm{LL}} & S_1^{\mathrm{LR}} \\ S_1^{\mathrm{RL}} & S_1^{\mathrm{RR}} \end{bmatrix} \begin{bmatrix} f_{1,\mathrm{L}}^{\mathrm{in}} \\ f_{1,\mathrm{R}}^{\mathrm{in}} \end{bmatrix}. \tag{2.67}$$

R_1 is a $\frac{5}{2}N \times \frac{5}{2}N$ matrix, and relates the distribution functions:

$$\begin{bmatrix} f_{1,\mathrm{R}}^{\mathrm{in}} \\ f_{2,\mathrm{L}}^{\mathrm{in}} \end{bmatrix} = \begin{bmatrix} R_1^{\mathrm{LL}} & R_1^{\mathrm{LR}} \\ R_1^{\mathrm{RL}} & R_1^{\mathrm{RR}} \end{bmatrix} \begin{bmatrix} f_{1,\mathrm{R}}^{\mathrm{out}} \\ f_{2,\mathrm{L}}^{\mathrm{out}} \end{bmatrix}. \tag{2.68}$$

To have a joint scattering matrix S_{lr} [18] covering the left lead (layer 1) and the interface at x_1, we have to eliminate the intermediate distribution functions $f_{1,\mathrm{R}}^{\mathrm{in/out}}$ in Eq. (2.67) and Eq. (2.68), to get

$$\begin{bmatrix} f_{1,\mathrm{L}}^{\mathrm{out}} \\ f_{2,\mathrm{L}}^{\mathrm{in}} \end{bmatrix} = S_{\mathrm{lr}} \begin{bmatrix} f_{1,\mathrm{L}}^{\mathrm{in}} \\ f_{2,\mathrm{L}}^{\mathrm{out}} \end{bmatrix}, \tag{2.69}$$

with

$$S_{\mathrm{lr}} = \begin{bmatrix} S_1^{\mathrm{LL}} + S_1^{\mathrm{LR}}(1 - R_1^{\mathrm{LL}} S_1^{\mathrm{RR}})^{-1} R_1^{\mathrm{LL}} S_1^{\mathrm{RL}} & S_1^{\mathrm{LR}}(1 - R_1^{\mathrm{LL}} S_1^{\mathrm{RR}})^{-1} R_1^{\mathrm{LR}} \\ R_1^{\mathrm{RL}}(1 - S_1^{\mathrm{RR}} R_1^{\mathrm{LL}})^{-1} S_1^{\mathrm{RL}} & R_1^{\mathrm{RR}} + R_1^{\mathrm{RL}}(1 - S_1^{\mathrm{RR}} R_1^{\mathrm{LL}})^{-1} S_1^{\mathrm{RR}} R_1^{\mathrm{LR}} \end{bmatrix}. \tag{2.70}$$

This is a $\frac{5}{2}N \times \frac{5}{2}N$ matrix. [19]

Using the same routine, we join the scattering matrix R_{lr} with S_2 to have the joint matrix S_{lrf} that covers the space (x_0^+, x_2^-) (including the left lead (layer 1), lead/FM interface (interface at x_1), and left FM layer (layer 2)). We keep on going to include the interface at x_2, then the scattering matrix becomes S_{lrfr} and covers the space (x_0^+, x_2^+).

Since the scattering matrix S_3 for the spacer layer uses z' axis instead of z as its spin quantization axis, we need to make a rotation to join S_{lrfr} with S_3. Using the left quantization axis z and the right quantization axis z', respectively, the scattering matrix S_{lrfr} and

[18] We continue to construct S_{lrf}, S_{lrfr}, S_{lrfrn}, S_{lrfrnr}, S_{lrfrnrf}, S_{lrfrnrfr}, and $S_{\mathrm{lrfrnrfrl}}$, where the last one is the system-wide scattering matrix we want. The subscript "l" denotes a lead, "r" denotes an NM/FM or FM/NM interface, "f" denotes a ferromagnet, and "n" denote the spacer layer.

[19] R_{lr} can also take the following form, which is used in the program,

$$R_{\mathrm{lr}} = \begin{bmatrix} S_1^{\mathrm{LL}} + S_1^{\mathrm{LR}} R_1^{\mathrm{LL}}(1 - S_1^{\mathrm{RR}} R_1^{\mathrm{LL}})^{-1} S_1^{\mathrm{RL}} & S_1^{\mathrm{LR}}[1 + R_1^{\mathrm{LL}}(1 - S_1^{\mathrm{RR}} R_1^{\mathrm{LL}})^{-1} S_1^{\mathrm{RR}}] R_1^{\mathrm{LR}} \\ R_1^{\mathrm{RL}}(1 - S_1^{\mathrm{RR}} R_1^{\mathrm{LL}})^{-1} S_1^{\mathrm{RL}} & R_1^{\mathrm{RR}} + R_1^{\mathrm{RL}}(1 - S_1^{\mathrm{RR}} R_1^{\mathrm{LL}})^{-1} S_1^{\mathrm{RR}} R_1^{\mathrm{LR}} \end{bmatrix}.$$

S_3, relate

$$\begin{bmatrix} f_{1,\mathrm{L}}^{\mathrm{out}} \\ f_{3,\mathrm{L}}^{\mathrm{in}} \end{bmatrix} = S_{\mathrm{lrfr}} \begin{bmatrix} f_{1,\mathrm{L}}^{\mathrm{in}} \\ f_{3,\mathrm{L}}^{\mathrm{out}} \end{bmatrix} \quad \text{and} \quad \begin{bmatrix} f_{3,\mathrm{L}}^{\mathrm{out}'} \\ f_{3,\mathrm{R}}^{\mathrm{out}'} \end{bmatrix} = S_3 \begin{bmatrix} f_{3,\mathrm{L}}^{\mathrm{in}'} \\ f_{3,\mathrm{R}}^{\mathrm{in}'} \end{bmatrix}. \tag{2.71}$$

To join S_{lrfr} with S_3, we write $f_{3,\mathrm{L}}^{\mathrm{in/out}}$ in terms of $f_{3,\mathrm{L}}^{\mathrm{in/out}'}$ in the left equation of Eq. (2.71). From Eq. (2.28), we have $f_{3,\mathrm{L}}^{\mathrm{in/out}'} = \hat{\mathbb{U}} f_{3,\mathrm{L}}^{\mathrm{in/out}}$, therefore

$$\begin{bmatrix} f_{1,\mathrm{L}}^{\mathrm{out}} \\ \hat{\mathbb{U}}^\dagger f_{3,\mathrm{L}}^{\mathrm{in}'} \end{bmatrix} = S_{\mathrm{lrfr}} \begin{bmatrix} f_{1,\mathrm{L}}^{\mathrm{in}} \\ \hat{\mathbb{U}}^\dagger f_{3,\mathrm{L}}^{\mathrm{out}'} \end{bmatrix} \Longrightarrow \begin{bmatrix} f_{1,\mathrm{L}}^{\mathrm{out}} \\ f_{3,\mathrm{L}}^{\mathrm{in}'} \end{bmatrix} = S'_{\mathrm{lrfr}} \begin{bmatrix} f_{1,\mathrm{L}}^{\mathrm{in}} \\ f_{3,\mathrm{L}}^{\mathrm{out}'} \end{bmatrix}, \tag{2.72}$$

with the rotated scattering matrix

$$S'_{\mathrm{lrfr}} = \begin{bmatrix} 1 & 0 \\ 0 & \hat{\mathbb{U}} \end{bmatrix} S_{\mathrm{lrfr}} \begin{bmatrix} 1 & 0 \\ 0 & \hat{\mathbb{U}}^\dagger \end{bmatrix}, \tag{2.73}$$

which can be joined with S_3 using the same joining procedure as described above, and becomes S_{lrfrn}. After joining all the scattering matrices, we will have a system wide $3N \times 3N$ scattering matrix $\mathbb{S} = S_{\mathrm{lrfrnrfrl}}$ which relates

$$\begin{bmatrix} f_{1,\mathrm{L}}^{\mathrm{out}} \\ f_{5,\mathrm{R}}^{\mathrm{out}'} \end{bmatrix} = \begin{bmatrix} \mathbb{S}_{\mathrm{LL}} & \mathbb{S}_{\mathrm{LR}} \\ \mathbb{S}_{\mathrm{RL}} & \mathbb{S}_{\mathrm{RR}} \end{bmatrix} \begin{bmatrix} f_{1,\mathrm{L}}^{\mathrm{in}} \\ f_{5,\mathrm{R}}^{\mathrm{in}'} \end{bmatrix} \equiv \mathbb{S} \begin{bmatrix} f_{1,\mathrm{L}}^{\mathrm{in}} \\ f_{5,\mathrm{R}}^{\mathrm{in}'} \end{bmatrix}. \tag{2.74}$$

2.2.7 Boundary Condition and System-wide Solutions

If we use Eq. (2.41) as the basis to expand the distribution functions $f_{1,\mathrm{L}}^{\mathrm{in/out}}$ and $f_{5,\mathrm{R}}^{\mathrm{in/out}'}$ in Eq. (2.74), there are in total $6N$ unknown coefficients, $3N$ for $f_{1,\mathrm{L}}^{\mathrm{in/out}}$ and $3N$ for $f_{5,\mathrm{R}}^{\mathrm{in/out}'}$. But there are only $3N$ equations in Eq. (2.74). The equations related to the x component of the distribution functions are all useless because there is no σ_x (or $\sigma_{x'}$) term in the distribution functions in layer 1 or layer 5. So if we ignore the x component, there are $2N$ equations, and $4N$ unknowns.

To reduce the number of unknowns, we examine the properties of the distribution functions near the reservoirs. Specifically, electrons that leave the reservoirs have a bulk-like distribution function and electrons with any distribution function can be absorbed by the reservoir. Based on these two facts, we propose that the distribution function near the reservoirs should satisfy: (1) for the electrons going from the reservoir to the lead, the

distribution function is bulk-like, namely $f^{\rm in}_{1,\rm L}$ and $f^{\rm in'}_{5,\rm R}$ have only the contributions from F^0_1 and F^0_2 in the basis for non-magnet Eq. (2.41);[20] and (2) for the electrons going from the lead to the reservoir, the distribution function has whatever structure it wants to have, namely $f^{\rm out}_{1,\rm L}$ and $f^{\rm out'}_{5,\rm R}$ have contributions from all $F^{0,z}_n$.

To determine the form of the distribution functions near the reservoirs, we need a new set of basis $G^{0,z}_n$ constructed from linear combinations of the old basis $F^{0,z}_n(x,\mu_i)$, so each $G^{0,z}_n$ meets the constraints above. Since the constraints are required only at the boundaries at x^+_0 and x^-_5, the new basis $G^{0,x,z}_n = G^{0,x,z}_n(\mu_i)$ is not a function of x but is evaluated at the boundaries. Without loss of generality, we let all the following functions be evaluated at $x = 0$.

First, we write down the old basis $F^{0,z}_n(x,\mu_i)$ in the following form,

$$\begin{bmatrix} F^s_1 \\ F^s_2 \\ F^s_p \\ F^s_q \end{bmatrix} = \left[\begin{array}{c|c|c|c} F^0_1(\mu^+_i) & F^0_1(\mu^-_i) & F^z_1(\mu^+_i) & F^z_1(\mu^-_i) \\ F^0_2(\mu^+_i) & F^0_2(\mu^-_i) & F^z_2(\mu^+_i) & F^z_2(\mu^-_i) \\ \hline F^0_p(\mu^+_i) & F^0_p(\mu^-_i) & F^z_p(\mu^+_i) & F^z_p(\mu^-_i) \\ \hline F^0_q(\mu^+_i) & F^0_q(\mu^-_i) & F^z_q(\mu^+_i) & F^z_q(\mu^-_i) \end{array}\right], \tag{2.75}$$

where $F^{0,z}_p$ denotes the $N-1$ eigenvectors with positive eigenvalues: $\lambda_p > 0$; and $F^{0,z}_p$ denotes the $N-1$ eigenvectors with negative eigenvalues: $\lambda_q < 0$.[21] The new basis G^s_n can be constructed using linear combinations of F^s_n as following:

$$\begin{bmatrix} G^s_1 \\ G^s_2 \\ G^s_p \\ G^s_q \end{bmatrix} = \left[\begin{array}{c|c|c|c} F^0_1(\mu^+_i) & F^0_1(\mu^-_i) & F^z_1(\mu^+_i) & F^z_1(\mu^-_i) \\ F^0_2(\mu^+_i) & F^0_2(\mu^-_i) & F^z_2(\mu^+_i) & F^z_2(\mu^-_i) \\ \hline 0 & G^0_p(\mu^-_i) & 0 & G^z_p(\mu^-_i) \\ \hline G^0_q(\mu^+_i) & 0 & G^z_q(\mu^+_i) & 0 \end{array}\right], \tag{2.76}$$

[20] $F^0_1(x,\mu_i)$ accounts for the uniform shift of the chemical potential, $F^0_2(x,\mu_i)$ accounts for the charge current.

[21] The eigenvalues of $F^{0,z}_1(x,\mu_i)$ and $F^{0,z}_2(x,\mu_i)$ are zero. And many elements in Eq. (2.75) are zero due to Eq. (2.43).

with

$$\begin{bmatrix} \star \\ G_p^s \end{bmatrix} = \begin{bmatrix} F_1^s \\ F_p^s \end{bmatrix} - \begin{bmatrix} F_1^0(\mu_i^+) & F_1^z(\mu_i^+) \\ F_p^0(\mu_i^+) & F_p^z(\mu_i^+) \end{bmatrix} \begin{bmatrix} F_1^0(\mu_i^+) & F_1^z(\mu_i^+) \\ F_q^0(\mu_i^+) & F_q^z(\mu_i^+) \end{bmatrix}^{-1} \begin{bmatrix} F_1^s \\ F_q^s \end{bmatrix}, \quad (2.77a)$$

$$\begin{bmatrix} \star \\ G_q^s \end{bmatrix} = \begin{bmatrix} F_1^s \\ F_q^s \end{bmatrix} - \begin{bmatrix} F_1^0(\mu_i^-) & F_1^z(\mu_i^-) \\ F_q^0(\mu_i^-) & F_q^z(\mu_i^-) \end{bmatrix} \begin{bmatrix} F_1^0(\mu_i^-) & F_1^z(\mu_i^-) \\ F_p^0(\mu_i^-) & F_p^z(\mu_i^-) \end{bmatrix}^{-1} \begin{bmatrix} F_1^s \\ F_p^s \end{bmatrix}, \quad (2.77b)$$

where $\star$ represents the first element in the column which we are not going to use.

We see that the new basis is constructed such that half of the basis vectors have bulk like right going behavior ($G_p^0(\mu_i^+) = G_p^z(\mu_i^+) = 0$), and the other half have bulk like left going behavior ($G_q^0(\mu_i^-) = G_q^z(\mu_i^-) = 0$). The value of the distribution function at the boundary is taken as a linear combination of the new basis G_σ^n to satisfy the constraints of the reservoir:

$$f_{1,\mathrm{L}}^0(\mu_i) = \alpha_0 G_0^0(\mu_i) + G_1^0(\mu_i) + \sum_p \alpha_p G_p^0(\mu_i), \quad (2.78a)$$

$$f_{1,\mathrm{L}}^z(\mu_i) = \alpha_0 G_0^z(\mu_i) + G_1^z(\mu_i) + \sum_p \alpha_p G_p^z(\mu_i), \quad (2.78b)$$

$$f_{5,\mathrm{R}}^{0'}(\mu_i) = \beta_1 G_1^0(\mu_i) + \sum_q \beta_q G_q^0(\mu_i), \quad (2.78c)$$

$$f_{5,\mathrm{R}}^{z'}(\mu_i) = \beta_1 G_1^z(\mu_i) + \sum_q \beta_q G_q^z(\mu_i), \quad (2.78d)$$

The incoming and outgoing states are determined by their side (L or R) and the sign of μ_i. In these equations, $\alpha_1 = 1$ fixes the current, and $\beta_0 = 0$ fixes the chemical potential at the right boundary to be zero. Since the indexes p and q each have $N-1$ numbers, the total number of unknown coefficients are $2N$, instead of $4N$ when using F_n^s as basis. Therefore, using Eq. (2.78) as the boundary distribution functions, we can solve for the coefficients $\alpha_0, \beta_1, \alpha_p$, and β_q using Eq. (2.74).

If we make the replacements

$$G_n(\mu_i) \equiv \begin{bmatrix} G_n^0(\mu_i) \\ G_n^z(\mu_i) \end{bmatrix}, \quad (2.79)$$

then Eq. (2.78) can be written as

$$f_{1,\mathrm{L}}(\mu_i) = \alpha_0 G_0(\mu_i) + G_1(\mu_i) + \sum_p \alpha_p G_p(\mu_i), \tag{2.80a}$$

$$f'_{5,\mathrm{R}}(\mu_i) = \beta_1 G_1(\mu_i) + \sum_q \beta_q G_q(\mu_i). \tag{2.80b}$$

To simplify the notation, we abbreviate $G_n^{\pm} \equiv G_n(\mu_i^{\pm})$, and use the Einstein convention (repeated indexes, p and q, are summed over). By plugging the boundary states Eq. (2.80) into Eq. (2.74),[22] we have

$$\begin{bmatrix} \alpha_0 G_0^- + G_1^- + \alpha_p G_p^- \\ \beta_1 G_1^+ + \beta_q G_q^+ \end{bmatrix} = \begin{bmatrix} \mathbb{S}_{\mathrm{LL}} & \mathbb{S}_{\mathrm{LR}} \\ \mathbb{S}_{\mathrm{RL}} & \mathbb{S}_{\mathrm{RR}} \end{bmatrix} \begin{bmatrix} \alpha_0 G_0^+ + G_1^+ + \alpha_p G_p^+ \\ \beta_1 G_1^- + \beta_q G_q^- \end{bmatrix}, \tag{2.81}$$

The LHS of Eq. (2.81):

$$\mathrm{LHS} = \begin{bmatrix} G_1^- \\ 0 \end{bmatrix} + \begin{bmatrix} G_0^- & G_p^- & 0 & 0 \\ 0 & 0 & G_1^+ & G_q^+ \end{bmatrix} \begin{bmatrix} \alpha_0 \\ \alpha_p \\ \beta_1 \\ \beta_q \end{bmatrix}, \tag{2.82}$$

and the RHS of Eq. (2.81):

$$\begin{aligned} \mathrm{RHS} &= \begin{bmatrix} \mathbb{S}_{\mathrm{LL}} G_1^+ \\ \mathbb{S}_{\mathrm{RL}} G_1^+ \end{bmatrix} + \begin{bmatrix} \mathbb{S}_{\mathrm{LL}} & \mathbb{S}_{\mathrm{LR}} \\ \mathbb{S}_{\mathrm{RL}} & \mathbb{S}_{\mathrm{RR}} \end{bmatrix} \begin{bmatrix} G_0^+ & G_p^+ & 0 & 0 \\ 0 & 0 & G_1^- & G_q^- \end{bmatrix} \begin{bmatrix} \alpha_0 \\ \alpha_p \\ \beta_1 \\ \beta_q \end{bmatrix} \\ &= \begin{bmatrix} \mathbb{S}_{\mathrm{LL}} G_1^+ \\ \mathbb{S}_{\mathrm{RL}} G_1^+ \end{bmatrix} + \begin{bmatrix} \mathbb{S}_{\mathrm{LL}} G_0^+ & \mathbb{S}_{\mathrm{LL}} G_p^+ & \mathbb{S}_{\mathrm{LR}} G_1^- & \mathbb{S}_{\mathrm{LR}} G_q^- \\ \mathbb{S}_{\mathrm{RL}} G_0^+ & \mathbb{S}_{\mathrm{RL}} G_p^+ & \mathbb{S}_{\mathrm{RR}} G_1^- & \mathbb{S}_{\mathrm{RR}} G_q^- \end{bmatrix} \begin{bmatrix} \alpha_0 \\ \alpha_p \\ \beta_1 \\ \beta_q \end{bmatrix}. \end{aligned} \tag{2.83}$$

[22] Remember to omit the y components in both distribution functions and scattering matrix $\mathbb{S}$.

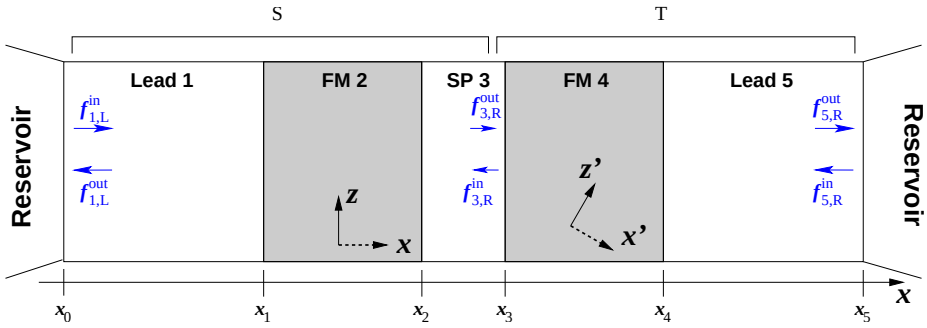

Figure 2.6: Back-propagation matrices.

By equating Eq. (2.82) and Eq. (2.83), we have which can be rearranged as

$$\begin{bmatrix} G_1^- - \mathbb{S}_{\mathrm{LL}} G_1^+ \\ -\mathbb{S}_{\mathrm{RL}} G_1^+ \end{bmatrix}$$

$$= \begin{bmatrix} \mathbb{S}_{\mathrm{LL}} G_0^+ - G_0^- & \mathbb{S}_{\mathrm{LL}} G_p^+ - G_p^- & \mathbb{S}_{\mathrm{LR}} G_1^- & \mathbb{S}_{\mathrm{LR}} G_q^- \\ \mathbb{S}_{\mathrm{RL}} G_0^+ & \mathbb{S}_{\mathrm{RL}} G_p^+ & \mathbb{S}_{\mathrm{RR}} G_1^- - G_1^+ & \mathbb{S}_{\mathrm{RR}} G_q^- - G_q^+ \end{bmatrix} \begin{bmatrix} \alpha_0 \\ \alpha_p \\ \beta_1 \\ \beta_q \end{bmatrix}. \tag{2.84}$$

In this equation, each of the $G_n^{\pm}$ is a $1 \times N$ matrix. Each symbol like $\mathbb{S}_{\mathrm{LL}}$ is a $N \times N$ matrix. Eq. (2.84) has $2N$ equations and $2N$ unknowns ($\alpha_{0,p}$ and $\beta_{1,q}$), so it is solvable. We use the solved α and β to retrieve the boundary distribution function values $f_{1,\mathrm{L}}(\mu_i) = f_1(x_0, \mu_i)$ and $f'_{5,\mathrm{R}}(\mu_i) = f'_5(x_5, \mu_i)$ using Eq. (2.80).

Once we have the distribution function values at the boundaries, it is straightforward to calculate the distribution function anywhere in the system because we have all the scattering matrices relating them to the boundary values. Here we only demonstrate how to calculate the distribution function in the spacer layer. As shown in Figure 2.6, S is the scattering matrix covering (x_0^+, x_3^-), and T is the scattering matrix covering (x_3^-, x_5^-):

$$\begin{bmatrix} f^{\mathrm{out}}_{1,\mathrm{L}} \\ f^{\mathrm{out}'}_{3,\mathrm{R}} \end{bmatrix} = \begin{bmatrix} S_{\mathrm{LL}} & S_{\mathrm{LR}} \\ S_{\mathrm{RL}} & S_{\mathrm{RR}} \end{bmatrix} \begin{bmatrix} f^{\mathrm{in}}_{1,\mathrm{L}} \\ f^{\mathrm{in}'}_{3,\mathrm{R}} \end{bmatrix} \quad \text{and} \quad \begin{bmatrix} f^{\mathrm{in}'}_{3,\mathrm{R}} \\ f^{\mathrm{out}'}_{5,\mathrm{R}} \end{bmatrix} = \begin{bmatrix} T_{\mathrm{LL}} & T_{\mathrm{LR}} \\ T_{\mathrm{RL}} & T_{\mathrm{RR}} \end{bmatrix} \begin{bmatrix} f^{\mathrm{out}'}_{3,\mathrm{R}} \\ f^{\mathrm{in}'}_{5,\mathrm{R}} \end{bmatrix}. \tag{2.85}$$

In these equations, $f^{\mathrm{in/out}}_{1,\mathrm{L}}$ and $f^{\mathrm{in/out}'}_{5,R}$ are already known from above, and there are only $3N$

unknown coefficients for $f'_{3,\mathrm{R}}(\mu_i)$, which can be written out using Eq. (2.42) and Eq. (2.43):

$$f'_{3,\mathrm{R}}(\mu_i) = \begin{bmatrix} f_3^{0'}(x_3,\mu_i) \\ f_3^{x'}(x_3,\mu_i) \\ f_3^{z'}(x_3,\mu_i) \end{bmatrix} = \begin{bmatrix} \sum_1^N \alpha_n^0 F_n^0(x_3,\mu_i) \\ \sum_{N+1}^{2N} \alpha_n^x F_n^x(x_3,\mu_i) \\ \sum_{N+1}^{2N} \alpha_n^z F_n^z(x_3,\mu_i) \end{bmatrix} \equiv \alpha_n F_n(x_3,\mu_i). \tag{2.86}$$

However, there are $6N$ equations in Eq. (2.85), so these equations are redundant. We choose half of the equations that use the incoming boundary values and not the outgoing ones, *i.e.*,

$$f_{3,\mathrm{R}}^{\mathrm{out}'} = S_{\mathrm{RL}} f_{1,\mathrm{L}}^{\mathrm{in}} + S_{\mathrm{RR}} f_{3,R}^{\mathrm{in}'}, \tag{2.87a}$$

$$f_{3,\mathrm{R}}^{\mathrm{in}'} = T_{\mathrm{LL}} f_{3,\mathrm{R}}^{\mathrm{out}'} + T_{\mathrm{LR}} f_{5,R}^{\mathrm{in}'}. \tag{2.87b}$$

Plugging Eq. (2.86) into this equation, we have

$$\begin{bmatrix} F_n(x_3,\mu_i^+) - S_{\mathrm{RR}} F_n(x_3,\mu_i^-) \\ F_n(x_3,\mu_i^-) - T_{\mathrm{LL}} F_n(x_3,\mu_i^+) \end{bmatrix} \alpha_n = \begin{bmatrix} S_{\mathrm{RL}} f_{1,\mathrm{L}}^{\mathrm{in}} \\ T_{\mathrm{LR}} f_{5,\mathrm{R}}^{\mathrm{in}'} \end{bmatrix}, \tag{2.88}$$

where the coefficients $\alpha_n^{0,x,z}$ can be easily solved by inversion. The full distribution function in the spacer layer $f_3(x,\mu_i)$ is calculated from these coefficients using Eq. (2.42). For the distribution functions in other layers, it is quite similar except we use different left and right scattering matrices.

2.2.8 Transport Properties

With the distribution functions in hand, it is straightforward to calculate transport properties like the spin density and spin current. Using Eq. (2.31), for layer m we have

$$\text{spin density:} \qquad n_m^s(x) = \sum_{i=1}^N w_i f_m^s(x,\mu_i), \tag{2.89a}$$

$$\text{spin current:} \qquad j_m^s(x) = \sum_{i=1}^N w_i \mu_i f_m^s(x,\mu_i), \tag{2.89b}$$

where $s = 0, x, z$ for $m = 1, 3, 5$ (non-magnetic layers) and $s = \uparrow, \downarrow$ for $m = 2, 4$ (ferromagnetic layers). The spin current at $x = x_3^-$ written in x'-z' frame is

$$\mathbf{Q}(x_3^-) = j_3^x(x_3^-)\hat{\mathbf{x}}' + j_3^z(x_3^-)\hat{\mathbf{z}}', \tag{2.90}$$

Table 2.2: Material parameters used in Boltzmann calculation.

Parameter	Material	Value	Units	Reference
l	Cu	110	nm	[30]
$l_{\rm sf}$	Cu	450	nm	[24]
$l^{\uparrow}$	Co	16.25	nm	[30]
$l^{\downarrow}$	Co	6.01	nm	[30]
$l_{\rm sf}$	Co	59	nm	[25]
$\alpha_{\uparrow}$	Co/Cu	0.051		[30]
$\alpha_{\downarrow}$	Co/Cu	0.393		[30]

where the $j_3^z(x_3^-)$ is the longitudinal piece parallel to the right FM layer's magnetization (z' direction), and $j_3^x(x_3^-)$ is the piece perpendicular to that. From Ref. [8], we know that the perpendicular spin current is absorbed at the NM/FM interface, therefore the spin-transfer torque acting on the right FM layer is

$$\mathbf{N}_{\rm st} = j_3^x(x_3^-)\hat{\mathbf{x}}'. \tag{2.91}$$

2.3 Results and Comparison

We now have two different approaches to calculate the spin-transfer torque in a spin valve: one is the full analytic approach described in Section 2.1 using Slonczewski's circuit theory, the other is the full numerical approach described in Section 2.2 using the Boltzmann equation. In this thesis, we examine a spin valve composed of Cu and Co, the results are quite similar if we replace Cu and Co by other non-magnet and ferromagnet materials. The input values in the Boltzmann calculation are listed in Table 2.2. The various l's are used in Eq. (2.37) and Eq. (2.39), and the $\alpha_{\uparrow,\downarrow}$ are used in Eq. (2.55) to evaluate the interface scattering coefficients.

In the circuit theory, the interface resistances for the Co/Cu interface used in Eq. (2.22) are: $G\bar{R}_I \simeq 0.97$ and $\Delta R_I/\bar{R}_I \simeq 0.72$. These values differ from the experimental value listed in Table 2.1 by about 15%. [23] These interface resistance values are actually obtained by fitting Eq. (2.15) to the spin-transfer torque calculated using the Boltzmann equation. The values of the contact resistance $G\bar{R}_C \simeq 1.1$ and $\Delta R_C/\bar{R}_C = 0$ used in Eq. (2.22)

[23]The relationship between the Boltzmann and experimental values for R_I is not straightforward. The experimental values are accurate to 10%-20% [Jack Bass (private communication)].

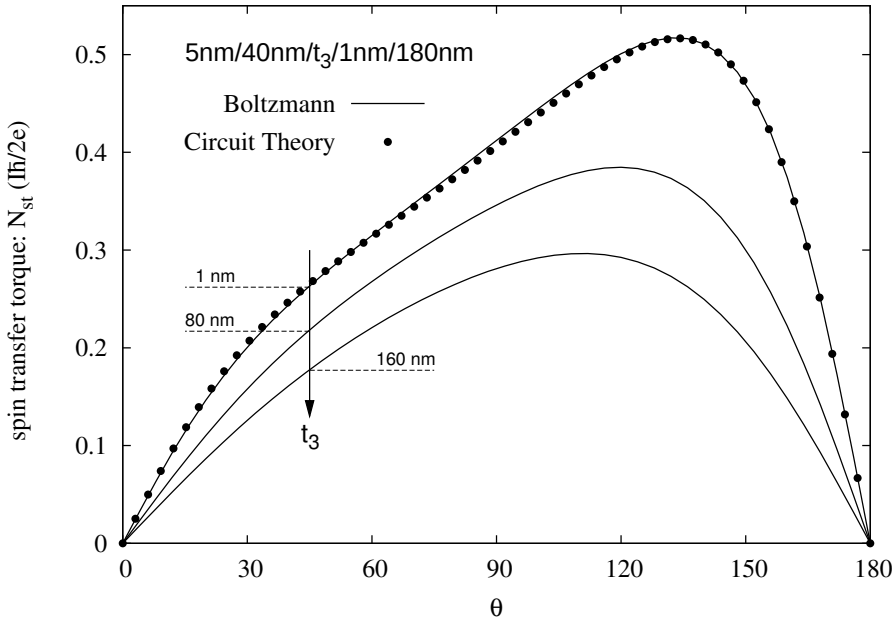

Figure 2.7: Spin-transfer torque at the right interface of the spacer layer in a spin valve with layer thicknesses 5 nm/40 nm/t_3/1 nm/180 nm with $t_3 = 1$ nm, 80 nm, and 160 nm. The solid curves are calculated from the Boltzmann equation. Solid circles are calculated by Eq. (2.15) from circuit theory. The latter do not depend on t_3.

are extracted from the Boltzmann calculation. The other material parameters used in the circuit theory can be found in Table 2.1.

The solid curves in Figure 2.7 show the angular dependence of the spin-transfer torque acting on the second (thin) Co layer calculated with the Boltzmann approach for a spin valve with geometry.

$$\text{Cu(5 nm)/Co(40 nm)/Cu(t}_3\text{)/Co(1 nm)/Cu(180 nm)},$$

The spacer layer thickness t_3 varies from 1 nm to 160 nm (the mean free path in Cu is $l = 110$ nm). The magnitude of the spin-transfer torque goes down as spacer layer thickness t_3 gets large is because the spin current injected into the right ferromagnet is smaller when the spacer layer thickness is larger due to the healing of Fermi surface after the interface scattering and spin flip scattering in the spacer layer.

The maxima of the spin-transfer torque curve does not occur for perpendicular alignment of the magnetizations ($\theta = 90^\circ$), but rather happens nearer to anti-parallel alignment. For a symmetric structure with magnetizations perpendicular to each other, the current

polarization is only 45° away from the magnetization. The current polarization becomes perpendicular to the magnetizations as they become antiparallel, but the amount of polarization decreases to zero in that limit. Therefore, the asymmetry of the curve comes from the competition between the direction and the magnitude of the current polarization.

Note that in the circuit theory, we ignored any kind of scattering in the spacer layer, which means we treat the spacer layer to be infinitely thin. In the case $t_3 = 1$ nm, the spacer layer thickness satisfies the condition of the circuit theory. If we fit the spin-transfer torque curve calculated from the Boltzmann equation using the spin-transfer torque formula Eq. (2.15) from the circuit theory (see Figure 2.7 for the fit), we find that the fitted interface resistance values agree with the experimental values within 15%. This is very good agreement considering the experimental values themselves are only accurate to 10%-20%. However, if the spacer layer thickness becomes comparable to the mean free path in Cu, the torque curves (the solid curve in Figure 2.7 with $t_3 = 80$ nm and 160 nm) cannot be fitted by the circuit theory for any values of the interface resistances.

Next, we study a spin valve with geometry:

$$\text{Cu(5 nm)/Co(40 nm)/Cu(1 nm)/Co(1 nm)/Cu(t}_5\text{)}.$$

Figure 2.8 shows how the spin-transfer torque curve acting on the second (thin) Co layer changes when we vary the right lead length t_5 from 10 nm to 160 nm. A second bump around $\theta = 30°$ appears as t_5 becomes large. From Eq. (2.15), we see that the second bump arises from the q_- term. The value of q_- is typically close to zero and negligible, but it gets prominent when the spin valve becomes highly asymmetric. By asymmetry, we mean that the left and right side of the spacer layer have different spin dependent properties. For instance, for a spin valve with the geometry

$$\text{Cu(5 nm)/Co(40 nm)/Cu(1 nm)/Co(1 nm)/Cu(160 nm)},$$

the left side of the spacer layer has 5 nm Cu and 40 nm Co and two Cu/Co interfaces, which can be considered mostly ferromagnetic, because both Co and Cu/Co interfaces have spin dependent resistances. However, on the right side of the spacer layer, there is only 1 nm of Co and two Cu/Co interfaces, but 160 nm Cu. So the 160 nm Cu dilutes the ferromagnetic

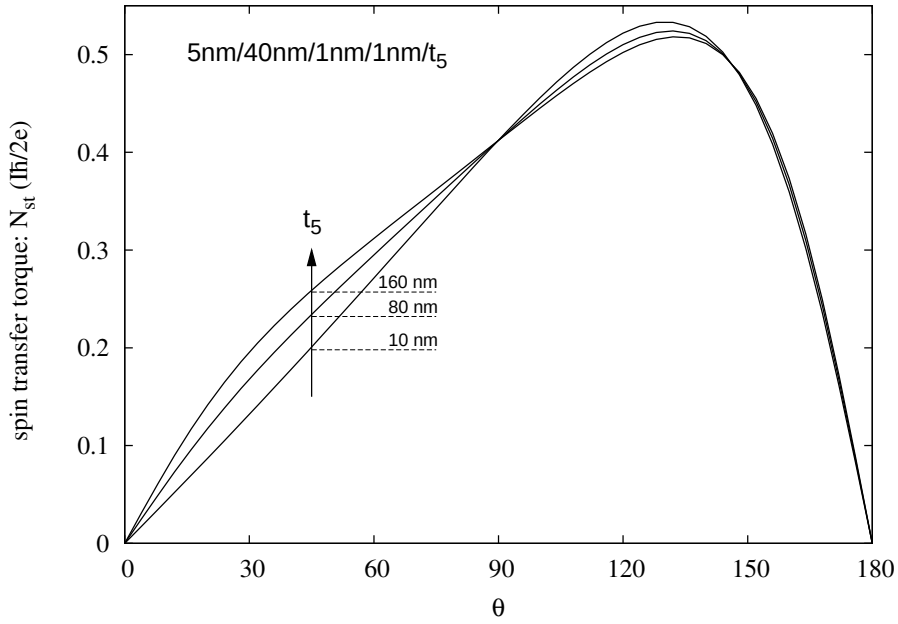

Figure 2.8: Spin-transfer torque at the right interface of the spacer layer in a spin valve with layer thicknesses 5 nm/40 nm/1 nm/1 nm/t_5 with t_5 = 10 nm, 80 nm, and 160 nm. All solid curves are calculated from the Boltzmann equation.

character of the Co bulk and the Cu/Co interfaces and makes the right side of the spacer layer more like a non-magnet. This asymmetry of the spin valve, ferromagnet-like on the left and non-magnet like on the right, leads to the emergence of the second bump in Figure 2.8.

The parameterization Eq. (2.15) is well suited to study the behavior of $N_{\rm st}^{\rm R}(\theta)$ when we vary the geometry of the magnetic heterostructure and the material parameters in our Boltzmann calculations. For convenience, we did this for symmetric geometries, so $\Lambda_L^2 = \Lambda_R^2 = \Lambda^2$. The left panel in Figure 2.9 confirms that Λ^2 is a linear function of $t_{\rm N}$ (see Eq. (2.22)) when $l_{\rm sf}^{\rm N} \gg t_{\rm N}$ but saturates when $t_{\rm N} \sim l_{\rm sf}^{\rm N}$. [24] Interestingly, the saturated value of Λ^2 varies linearly with $l_{\rm sf}^{\rm N} - l^{\rm N}$ ($l^{\rm N}$ is the inelastic scattering length) rather than with $l_{\rm sf}^{\rm N}$ as predicted by Eq. (2.22). For long leads, this can be understood from the fact that conventional resistive scattering is needed to build up non-equilibrium spin accumulation in the non-magnet while spin-flip scattering works to return the non-magnet to equilibrium.

The right panel in Figure 2.9 shows the variation of Λ^2 with lead length for different

[24] The value of Λ^2 is obtained by fitting the spin-transfer torque calculated by Boltzmann approach using Eq. (2.15).

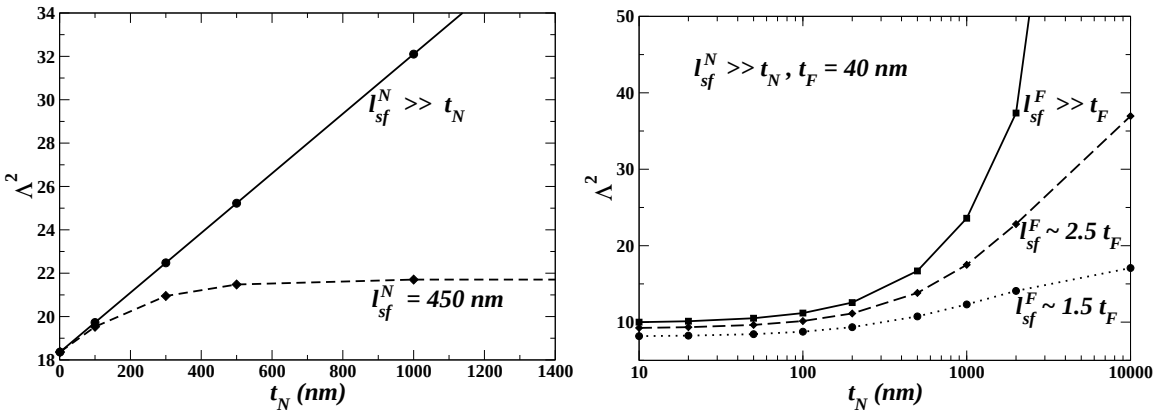

Figure 2.9: Left: Torque parameter Λ^2 as a function of $t_{\rm N}$ for large and small values of $l_{\rm sf}^{\rm N}$. Right: Torque parameter Λ^2 as a function of $t_{\rm N}$ for different values of $l_{\rm sf}^{\rm F}$. In all cases, $l_{\rm sf}^{\rm N} = \infty$. The curve for $l_{\rm sf}^{\rm F} \gg t_{\rm F}$ corresponds to $\Lambda^2 \propto t_{\rm N}$.

values of the spin-flip length in the ferromagnet. This calculation puts $l_{\rm sf}^{\rm N} \to \infty$, so we expect from Eq. (2.22) that $\Lambda^2 \propto t_{\rm N}$. This is indeed the case when $l_{\rm sf}^{\rm F} \gg t^{\rm F}$. However, when the $l_{\rm sf}^{\rm F}$ is comparable (or less than) the ferromagnetic layer thickness, the torque parameter saturates. This is a signal that our approximation $Q_0 \simeq Q_L$ used in Eq. (2.22) in the circuit theory has broken down. In this limit, fast spin-flipping in the ferromagnet reduces Q_0 to a value much less than Q_L.

The break down of the approximation $Q_0 \simeq Q_L$ can also be seen from Figure 2.10, where we show how the spin-transfer torque curve changes when varying the thickness of the left ferromagnetic layer t_2. Since $t_2 = 10$ nm is small compared to the spin flip length $l_{\rm sf}^F = 59$ nm in the ferromagnet, the circuit theory and the Boltzmann calculation agree with each other very well. But when $t_2 = 160$ nm becomes comparable or larger than $l_{\rm sf}^F$, the circuit theory fails. [25] The reason is that $Q_0 \simeq Q_L$ no longer holds when $t_2 \gtrsim l_{\rm sf}^F$. In this case, Q_0 actually depends on t_2 in a non-trivial way.

A characteristic difference between spin-transfer torque for a symmetric geometry and for an asymmetric geometry can be seen from the difference between the curves in Figure 2.8. The curve with $t_5 = 10$ nm has a bump (maximum) in the interval $\pi/2 < \theta < \pi$ only. The curve with $t_5 = 160$ nm has a small additional bump in the interval $0 < \theta < \pi/2$ that

[25] The input values in the circuit theory here in Figure 2.10 are the same as those used in Figure 2.7.

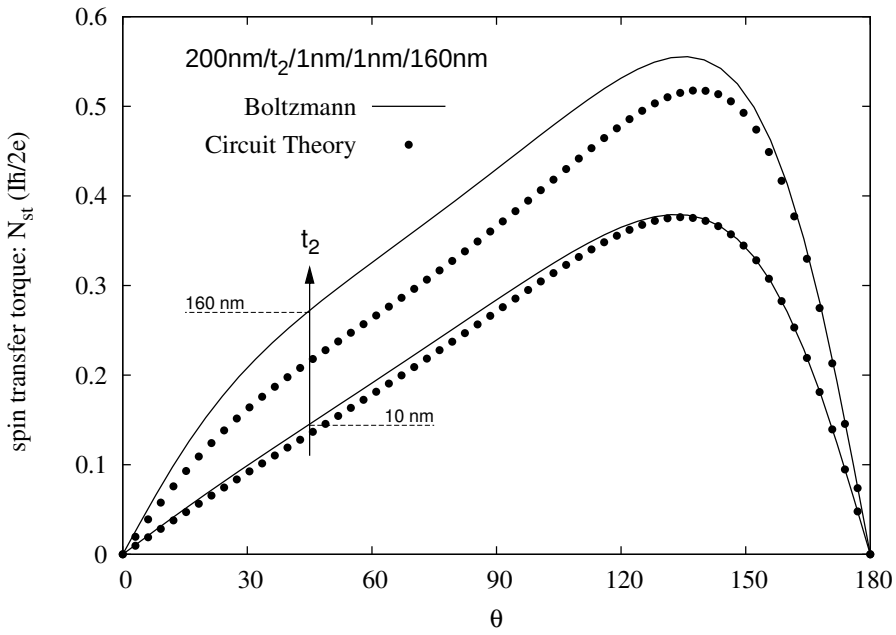

Figure 2.10: Spin-transfer torque at the right interface of the spacer layer in a spin valve with layer thicknesses 200 nm/t_2/1 nm/1 nm/160 nm with $t_2 = 10$ nm, and 160 nm. Solid curves are calculated from the Boltzmann equation, dotted curves are from circuit theory.

comes from the q_- term in Eq. (2.15). This small change is enough to produce stable magnetization precession for some asymmetric geometries.

Consider a spin valve in the presence of an external magnetic field aligned with the magnetization of the thick ferromagnet. In equilibrium, the magnetizations in both layers align with the external field; they are in parallel configuration. If we ignore shape anisotropy and lattice anisotropy, the total torque acting on the right ferromagnetic film when electrons flow from right to left in Figure 2.2 is the sum of the spin-transfer torque $L_R(\theta)$ and a Gilbert damping torque $\gamma H \sin\theta$ (top panel of Figure 2.11). [26]

The spin-transfer torque (positive torque in the top panel of Figure 2.11) pulls the magnetization of the right ferromagnetic layer away from parallel configuration, and the damping torque (negative torque) pulls the magnetization back to parallel. As the current increases, the spin-transfer torque increases and the total torque becomes positive, and the positive torque destabilizes parallel state. The total torque pulls the magnetization away from parallel until the total torque becomes zero again. Therefore, stable precession

[26] We will discuss Gilbert damping more thoroughly in Section 3.1.2 .

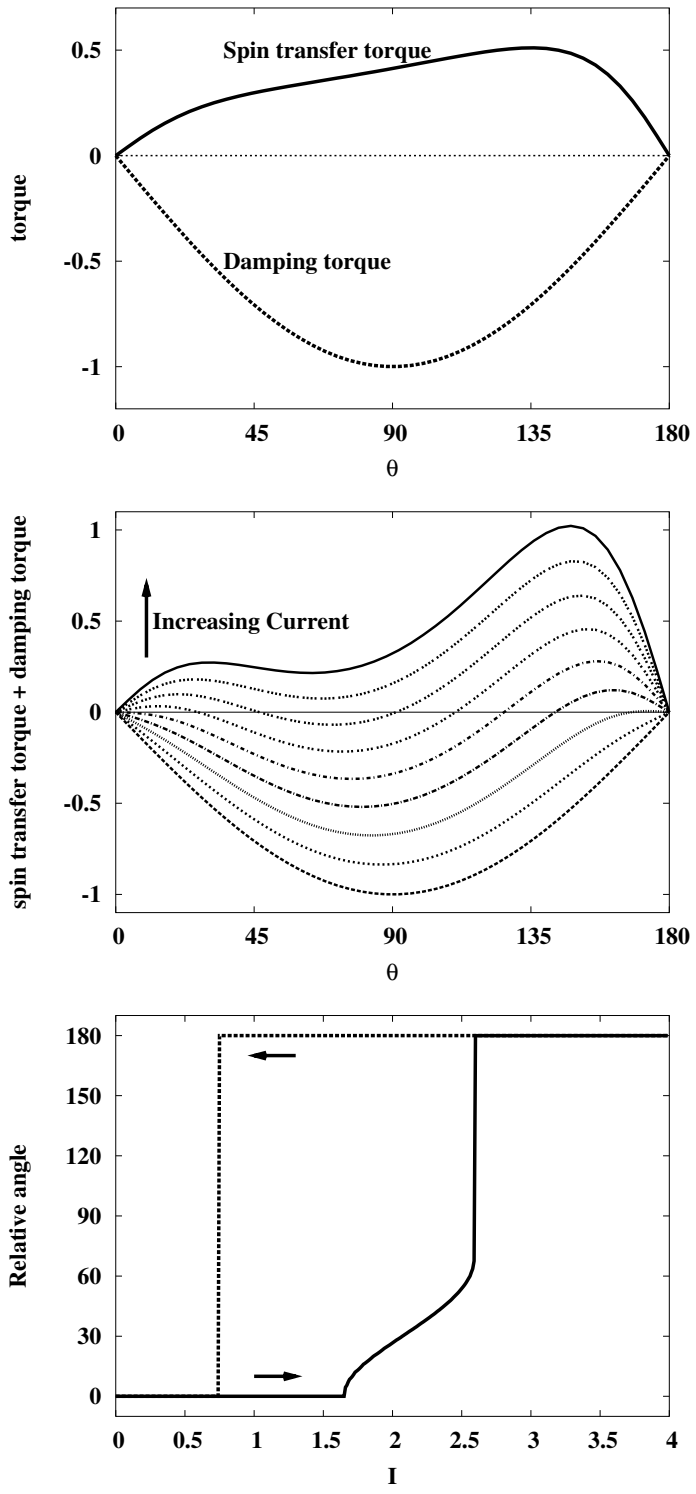

Figure 2.11: Top: Spin-transfer torque and damping torque for a 1 nm/40 nm/1 nm/1 nm/1000 nm spin valve ($q_-/q_+ \approx 0.36$); Middle: the total torque as the current increases; Bottom: the angle between two ferromagnetic moments as a function of current I in arbitrary units.

occurs at angles where the total torque changes from positive to negative (middle panel of Figure 2.11). When the total torque becomes everywhere positive, the system abruptly switches to the anti-parallel configuration (bottom panel of Figure 2.11). There is no regime of stable precession if the zero-current state is anti-parallel. [27]

In summary, we have shown that Slonczewski's circuit theory of spin-transfer torque in spin valves can reproduce the results of Boltzmann equation calculations when the non-magnetic spacer layer is thin. When the ferromagnetic layers and the spacer layer are thin, the parameters of the theory can be calculated from first principles. The results also show that asymmetric spin valves have qualitative differences from symmetric spin valves.

[27] The anisotropy-driven precession state found by Bazaliy *et al.* [31] occurs only when the magnetization and the external field are nearly anti-parallel.

CHAPTER III

MACROSPIN MODELS OF SPIN-TRANSFER DYNAMICS

The effect of spin-transfer torque on a spin valve (Figure 3.1) is to induce hysteretic switching and/or precession of the magnetization **m** in the (thinner) free layer. Because of the phenomenon of giant magnetoresistance [24], voltage measurements are sufficient to reveal that hysteretic switching of **m** occurs as a function of the applied current density J when a magnetic field H smaller than the coercive field is applied along the easy axis of the free layer. For larger values of H, it is believed that **m** exhibits one or more types of stable precession as a function of J until the current density is large enough to induce switching (see the left panel of Figure 3.2). This conclusion [6, 32–35] is based on the experimental observation of narrow band microwave emission (right panel of Figure 3.2) combined with calculations using a generalized Landau-Lifshitz-Gilbert (LLG) equation that predict precession of the free layer. Other observed dynamical behavior includes telegraph noise that is interpreted as rapid switching between two distinct states of magnetization. [5, 36–38]

Several experimental groups have used a macrospin (single domain) approximation to propose "phase diagrams" that identify the dynamical state of their spin valves as a function of J and H [3, 5, 32, 38–42] There have also been purely theoretical studies of the LLG equation (generalized to include spin-transfer torque) using both macrospin models [31, 43–48] and micromagnetics simulations [49–55] that do not make the single-domain

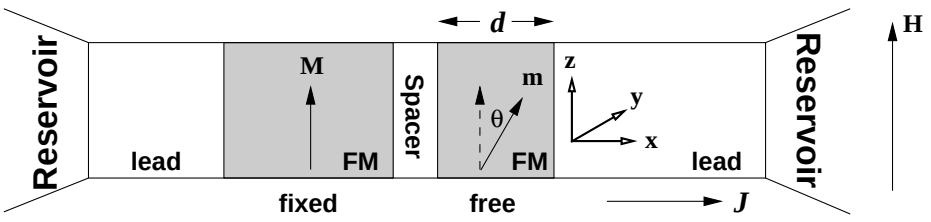

Figure 3.1: Schematic view of a spin valve.

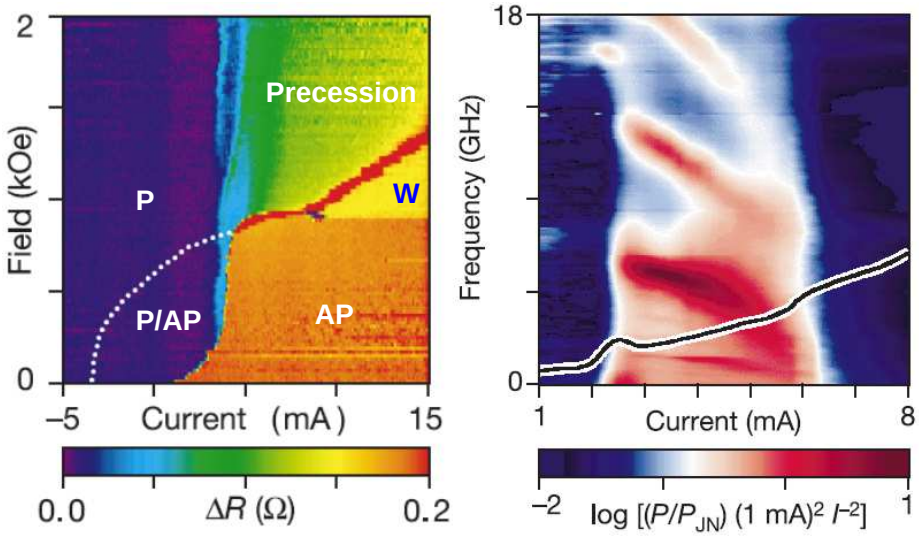

Figure 3.2: Left: differential resistance phase diagram. Right: microwave power (color scale) as function of frequency and current at fixed field (from Ref. [32]).

approximation. Unfortunately, it is difficult to extract a coherent picture from all this work because different authors make different choices for the physical effects they believe most affect the dynamics. There is not even unanimity amongst authors for the form of the spin-transfer torque itself.

This state of affairs motivated us to perform a thorough study of the LLG dynamics of a model spin valve for the purpose of a quantitative comparison with the data (Figure 3.2) reported by Kiselev *et al.* [32] for a Co/Cu/Co nanopillar. We make the macrospin approximation, but otherwise systematically examine the effects of different forms of spin-transfer torque, thermal fluctuations, spin-pumping, incomplete absorption of transverse spin current, and angle-dependent damping. We find that a "minimal" macrospin model can reproduce many (but not all) features of the experiment. The most important points of disagreement are the current dependence of the precession frequency and the existence of a microwave quiet magnetic phase with a distinct magnetoresistance signature. In light of these results, we comment on micromagnetic simulations [52, 55] designed to model the identical set of experimental data.

The plan of this chapter is as follows. Section 3.1 describes the macrospin models of

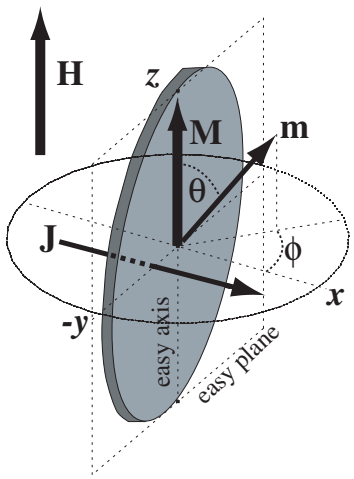

Figure 3.3: The ellipsoidal cross section of the free layer (shaded) lies in y-z plane. We represent its magnetization by a macrospin $\mathbf{m}$ that can point in any direction. The fixed layer (not shown) is represented by a fixed macrospin $\mathbf{M} \parallel \hat{\mathbf{z}}$.

interest and the generalized Landau-Lifshitz-Gilbert equation we solve numerically. Section 3.2 presents results for a "minimal" model and compares them to the measurements reported in Ref. [32]. Section 3.3 examines several variations of the minimal model within the context of the macrospin approximation. Section 3.4 compares our results with micromagnetic simulations. Section 3.5 compares our results to experiment. Appendix A provides some details omitted from the main body of the chapter.

3.1 The Macrospin Model

Our macrospin model of the spin valve shown in Figure 3.1 assumes that the magnetization is spatially uniform in both ferromagnetic layers with saturation value M_{s}. The fixed layer magnetization is $\mathbf{M} = M_s\hat{\mathbf{z}}$, but we allow the unit vector in the direction of the free layer magnetization $\hat{\mathbf{m}} = \mathbf{m}/M_s$ to point in any direction. In the coordinate system used here (Figure 3.3),

$$\hat{\mathbf{m}} = \hat{\mathbf{x}}\sin\theta\cos\phi + \hat{\mathbf{y}}\sin\theta\sin\phi + \hat{\mathbf{z}}\cos\theta. \tag{3.1}$$

The experiments of interest [32] use a "free" ferromagnetic layer with a thickness $d \approx 3$ nm and an elliptical shape of dimensions about 130 nm $\times$ 70 nm. Under these conditions, magnetostatic shape anisotropy makes the y-z plane an easy plane for $\mathbf{m}$. The z-axis is an easy axis in that plane. The control parameters are an external magnetic field H

Table 3.1: Physical quantity values in LLG calculation.

Quantity	Material	Value	Unit	Reference
M_s	Co	$0.127 \cdot 10^7$	A/m	[32]
$\mu_0 M_\mathrm{s}$	Co	1.6	T	
γ	Co	$2.4 \cdot 10^5$	m/(As)	[57]
K_u		$0.5 \cdot 10^{-3}$	J/m^2	[58]
α	Co	0.01		[59]
$g^{\uparrow\downarrow}/S$	Cu	$2.94 \cdot 10^{19}$	1/m^2	[60]
ν	Co/Cu	0.98		[60]

directed along $+z$ and an electric current J that is reckoned positive when negatively charged electrons flow from $+x$ to $-x$.

We describe the dynamics of $\hat{\mathbf{m}}$ using a generalized Landau-Lifshitz-Gilbert (LLG) equation [9, 56],

$$\frac{d\hat{\mathbf{m}}}{dt} = -\gamma \hat{\mathbf{m}} \times [\mathbf{H}_\mathrm{eff} + \mathbf{H}_\mathrm{T}] + \alpha \hat{\mathbf{m}} \times \frac{d\hat{\mathbf{m}}}{dt} + \frac{\gamma}{\mu_0 M_s}\mathbf{N}. \tag{3.2}$$

It will be convenient to discuss each term in Eq. (3.2) in turn.

3.1.1 Energy

The first term on the right side of Eq. (3.2) is a conventional magnetic torque with gyromagnetic ratio γ. This torque is driven by an effective field derived from the total energy E of the free layer with volume V:

$$\mu_0 \mathbf{H}_\mathrm{eff} = -\frac{1}{V}\frac{\partial E}{\partial \mathbf{m}}. \tag{3.3}$$

Taking account of magnetostatics, the external field, and a uniaxial surface anisotropy, we show in Appendix A that E can be written in the form

$$\frac{2E}{\mu_0 M_\mathrm{s}^2 V} = h_Z \cos^2\theta + h_Y \sin^2\theta \sin^2\phi + h_X \sin^2\theta \cos^2\phi - 2h\cos\theta. \tag{3.4}$$

Here, $h = H/M_s$ and the constants h_X, h_Y, and h_Z are computed in Appendix A using the free layer data given just below Eq. (3.1) and the material constants listed in Table 3.1.

3.1.2 Damping

The "Gilbert damping" term $\alpha \hat{\mathbf{m}} \times \dot{\hat{\mathbf{m}}}$ in Eq. (3.2) takes account of energy dissipation mechanisms such as coupling to lattice vibrations [61] and spin-flip scattering. [62] While

there is active debate among researchers whether this form of the damping is correct [63–66], this is the form that is used by almost all practitioners. The pre-factor α is usually treated as a phenomenological constant (Table 3.1) although it is not known whether this is a good approximation for situations where the amplitude of precessional motion is large. The Landau-Lifshitz approach to damping replaces the Gilbert term in Eq. (3.2) by

$$\lambda \hat{\mathbf{m}} \times (\hat{\mathbf{m}} \times \mathbf{H}_{\text{eff}}). \tag{3.5}$$

The constant λ can be calculated in some microscopic models, [67] but a phenomenological treatment is almost universal. When $\mathbf{N} = 0$ in Eq. (3.2), the Gilbert and Landau-Lifshitz expressions for the damping torque are known to be equivalent, at least formally [68]. Section 3.1.4 gives a reason why we prefer the Gilbert form, but we performed calculations using both forms for purposes of comparison. No significant differences were found.

3.1.3 Thermal Fluctuations

The stochastic vector $\mathbf{H}_{\text{T}}$ in Eq. (3.2) is used to simulate the effect of finite temperature. Each Cartesian component is chosen at random from a normal distribution with a variance chosen so the system relaxes to a Boltzmann distribution at equilibrium [69]. Specifically,

$$\langle H_{\text{T}}^{i}(t) H_{\text{T}}^{j}(t') \rangle = \frac{2 k_B T \alpha}{\gamma V \mu_0 M_{\text{s}}} \delta_{ij} \delta(t - t'), \tag{3.6}$$

where $i, j = x, y, z$.

We solve the stochastic LLG equation using the Ito calculus [70] and a numerical method described by Milshtein [71]. We have confirmed numerically that this procedure does indeed produce a Boltzmann distribution of energies at temperature T when $\mathbf{N} = 0$ in Eq. (3.2): $n(E) = g(E) e^{-E/k_B T}$, where $n(E)$ is the possibility of the magnetization with energy E, and $g(E)$ is the density of states at energy E.

In the absence of anisotropies (only external magnetic field H existing), $E = V M_s H \cos\theta$, where V is the volume of the magnetic film and θ is the angle between H and the magnetization. In this case, the density of states can be computed as:

$$g(E) = \frac{1}{4\pi} \int_0^{\pi} d\theta \; \delta(E - V M_s H \cos\theta) = \frac{1}{4\pi} \frac{1}{\sqrt{1 - (E/V M_s H)^2}}, \tag{3.7}$$

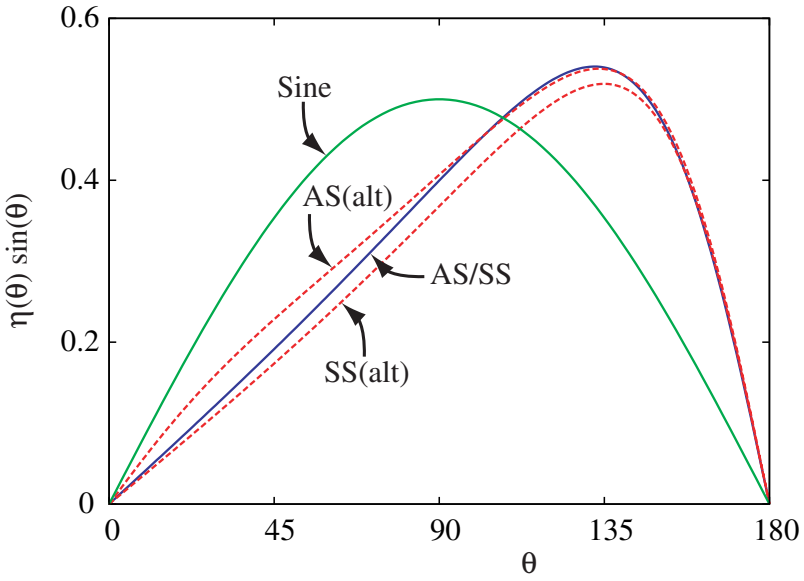

Figure 3.4: Various forms of (dimensionless) spin-transfer torque as a function of the angle θ between the fixed layer and the free layer. The sine torque does not depend on the spin valve geometry. The symmetric Slonczewski (SS) and asymmetric Slonczewski (AS) torques are essentially identical for the standard spin valve geometry studied in this chapter (AS/SS solid curve). The dashed curves show the difference between the symmetric and asymmetric Slonczewski torques for a geometry discussed in Section 3.3.2.

in which only the angle θ is integrated, but not the precessional angle ϕ. The reason is that the damping only occurs in the θ direction, the motion in ϕ direction is deterministic, therefore there is no stochastic process in ϕ direction.

3.1.4 Spin-transfer

As discussed in Chapters 1 and 2, the spin-transfer torque in a spin valve has the form

$$\mathbf{N}_{\rm st} = \eta(\theta)\frac{\hbar}{2e}\frac{J}{d}\hat{\mathbf{m}} \times [\hat{\mathbf{m}} \times \hat{\mathbf{M}}], \tag{3.8}$$

where $\hat{\mathbf{M}} = \mathbf{M}/M_s$ and $\cos\theta = \hat{\mathbf{m}} \cdot \hat{\mathbf{M}}$. The different forms of spin-transfer torque one finds in the literature correspond to different choices for $\eta(\theta)$. If one simply puts $\eta(\theta) = \eta_0$, the result is a "sine" approximation to the torque because the remaining angular factors in Eq. (3.8) give $\mathbf{N}_{\rm st} \propto \sin\theta$ (Figure 3.4). This form of the torque arises when there is spin-dependent scattering at the free layer interface and the polarization of the electron current that flows from the fixed layer to the free layer is independent of the orientation of the free layer. The prefactor $\eta(\theta)$ is not constant if there is a diffusive component to the

current anywhere and/or spin-dependent reflection occurs at the fixed-layer interface. To our knowledge, one or both of these effects is present in all transport theory calculations of $\mathbf{N}_{\rm st}$. On the other hand, the corresponding $\sin^2(\theta/2)$ approximation for the angular dependence of the magnetoresistance describes real spin valve data [72] better than one would expect based on the transport theory predictions, to which we turn next.

Our results from Chapter 2 gave

$$\eta(\theta) = \frac{q_+}{A + B\cos\theta} + \frac{q_-}{A - B\cos\theta}. \tag{3.9}$$

We will call this the asymmetric Slonczewski (AS) approximation. If $q_- = 0$, we have the symmetric Slonczewski (SS) torque. One of the solid curves in Figure 3.4 shows that the symmetric and asymmetric Slonczewski torques are essentially identical for the particular spin valve geometry we use to model the experimental sample of Ref. [32] (see Section 3.2). The two dashed curves show the difference between the the symmetric and asymmetric Slonczewski torques for a spin valve geometry we will discuss in Section 3.3.2.

Spin-transfer torque accounts for non-equilibrium processes that cannot be described by an energy functional. This means that $\mathbf{N}_{\rm st}$ does not produce an effective field like Eq. (3.4) and no damping of spin-transfer dynamics occurs if $\mathbf{H}_{\rm eff} = 0$ and the Landau-Lifshitz form Eq. (3.5) is used for damping. On the other hand, if one believes that it must be possible to influence spin-transfer driven motion by transferring energy to other degrees of freedom, it is necessary to use the Gilbert form of damping in the magnetization equation of motion. This is what we do in Eq. (3.2).

3.1.5 Current-Induced Effective Field

First principles calculations [8, 73] show that the absorption of a transverse spin current at a ferromagnetic interface is not 100% efficient. Part of the fraction that survives gives a small correction to $\eta(\theta)$ in Eq. (3.8). The remainder is polarized perpendicular to both $\mathbf{m}$ and $\mathbf{M}$ and contributes a torque density on the free layer of the form

$$\mathbf{N}_{\rm eff} = \eta(\theta)\beta\frac{\hbar}{2e}\frac{J}{d}\hat{\mathbf{m}} \times \hat{\mathbf{M}}. \tag{3.10}$$

Evidently, $\mathbf{N}_{\rm eff}$ produces motion of $\hat{\mathbf{m}}$ identical to that produced by an effective external field oriented along the magnetization direction $\hat{\mathbf{M}}$ of the fixed layer. This contribution is usually neglected because the cited calculations find $\beta \approx 0.05$. We include it here because at least one experiment [41] has been interpreted as demonstrating that $\beta \approx 0.20$.

3.1.6 Spin Pumping

A final contribution to the torque on the free layer comes from a phenomenon called "spin pumping". Since a spin polarized current incident from a non-magnet can produce magnetization dynamics in an adjacent ferromagnet, it is not unreasonable that motion of the magnetization of a ferromagnet can influence the spin current in an adjacent non-magnet. The most prominent effect is the injection of a spin current into the non-magnet whenever the magnetization moves. One consequence of the injected spin current is a back-reaction torque that increases the damping of the spin motion [74–76]. This effect has been confirmed by experiments [77–80]. The torque density due to spin-pumping is given by Tserkovnyak *et al.* [60] as

$$\mathbf{N}_{\rm sp} = \frac{1}{d}\hat{\mathbf{m}} \times \mathbf{J}_s^{\rm exch} \times \hat{\mathbf{m}}, \tag{3.11}$$

where

$$\mathbf{J}_s^{\rm exch} = \frac{1}{2}\left[\mathbf{J}_s^{\rm sp} - \nu(\mathbf{J}_s^{\rm sp}\cdot\hat{\mathbf{M}})\frac{\hat{\mathbf{M}} - \nu\hat{\mathbf{m}}\cos\theta}{1-\nu^2\cos^2\theta}\right] \tag{3.12}$$

with

$$\mathbf{J}_s^{\rm sp} = \frac{\hbar g^{\uparrow\downarrow}}{4\pi S}\hat{\mathbf{m}} \times \frac{d\hat{\mathbf{m}}}{dt}. \tag{3.13}$$

S is the cross-sectional area of the free layer. Table 3.1 gives numerical values for the parameters ν and $g^{\uparrow\downarrow}$ (defined in Ref. [81]) for the Co/Cu/Co spin valve of interest to us here.

3.2 Minimal Model

This section compares LLG simulation results with the experimental results reported in Ref. [32]. Our "minimal" model is Eq. (3.2) with $\mathbf{N} = \mathbf{N}_{\rm st}$ from Eq. (3.8) and the asymmetric Slonczewski (AS) choice in Eq. (3.9) for $\eta(\theta)$. This model takes account of magnetostatic and surface anisotropy, an external magnetic field, current-induced spin-transfer torque, Gilbert

damping, and thermal fluctuations. Most of our calculations use a spin valve geometry (see Figure 1.1) designed to mimic the nanopillar samples studied by Kiselev *et al.* [32]:

$$\text{Cu(80 nm)/Co(40 nm)/Cu(thin)/Co(3 nm)/Cu(10 nm).}$$

The notation Cu(thin) indicates that the thickness of the spacer layer is immaterial as long as it is smaller than the mean free path in copper. The precise choice of lead lengths is subject to uncertainty due to the approximations needed to model finite width and reservoir effects in a one-dimensional Boltzmann equation calculation of spin valve transport [82].

3.2.1 Computational Details

The simulations proceed by fixing the external field H and sweeping the current density J in steps of size δJ. Before changing to the next value of J, we integrate the LLG equation for a "waiting time" t^* using N time steps of length δt. After each time step, we use the instantaneous value of the angle θ between $\mathbf{M}$ and $\mathbf{m}$ and the results of Ref. [30] to evaluate the instantaneous magnetoresistance $R(\theta)$. A time-average over these N values gives the resistance we report for each J.

Figure 3.5 shows the calculated high-field and low-field magnetoresistance as a function of J for three values of the simulated sweep rate $\mathrm{SR} = \delta J/t^*$. The curves in this figure are averages over 20 realizations of the stochastic simulation. In each realization, the system switches abruptly at a particular value of current between states with distinctly different magnetoresistance (to be discussed below). Since the switching current depends on the realization, an average over essentially vertical transitions at slightly different switching currents gives the not-quite-vertical lines seen in the figure. As expected, the hysteresis loops close as the sweep rate decreases. Less obviously, the rate of closing is much greater at high field than at low field. It is important to appreciate that the simulated current sweeps are limited by the degree of numerical convergence, available computing resources, and the simulator's patience. The slowest sweep rate we found we could practically use in our simulations [$10^{11}\mathrm{A}/(\mathrm{cm}^2{\cdot}\mathrm{s})$] is still five orders of magnitude faster than the sweep rate used in the Cornell experiments.

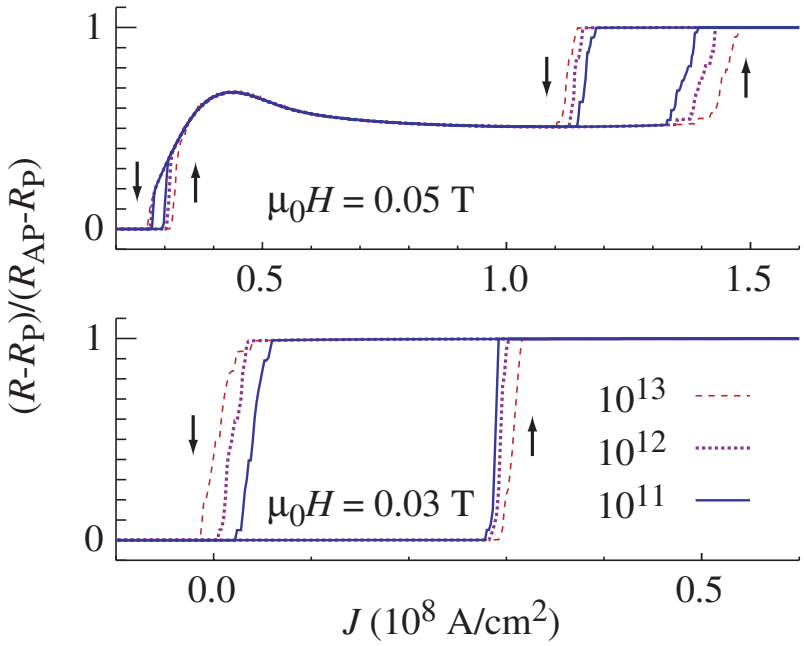

Figure 3.5: High field (upper panel) and low field (lower panel) magnetoresistance as a function of current density sweep rate (SR) in units of A/(cm^2·s). The up arrows identity the parts of the hysteresis loops traced out when J is scanned from negative values to positive values. The down arrows correspond to scanning from positive values to negative values of J.

For fixed values of H and J, the N values of resistance collected between $t = 0$ and $t = t^*$ constitute a time series for the resistance. Spin valves are Ohmic devices, so the Fourier transform of this series is proportional to the associated power spectrum. We use this numerical data below to compare with the microwave noise data reported in Ref. [32].

3.2.2 J-H Phase Diagrams

Figure 3.6 compares spin valve "phase diagrams" at $T = 3$ K, $T = 300$ K, and $T = 3000$ K for our minimal model. These should be compared with the diagram on the left side of Figure 3.2. Our diagrams were constructed by sweeping the current twice (once increasing the current and once decreasing the current) for each value of H. There is some noise at higher temperature because we did not average over multiple realizations of the simulation. Solid lines divide each diagram into phase fields with labels like A, B and A/B. The latter means that the field is occupied by phase A when the current is scanned from left-to-right in the diagram and by phase B when the current is scanned from right-to-left. Thus, a label

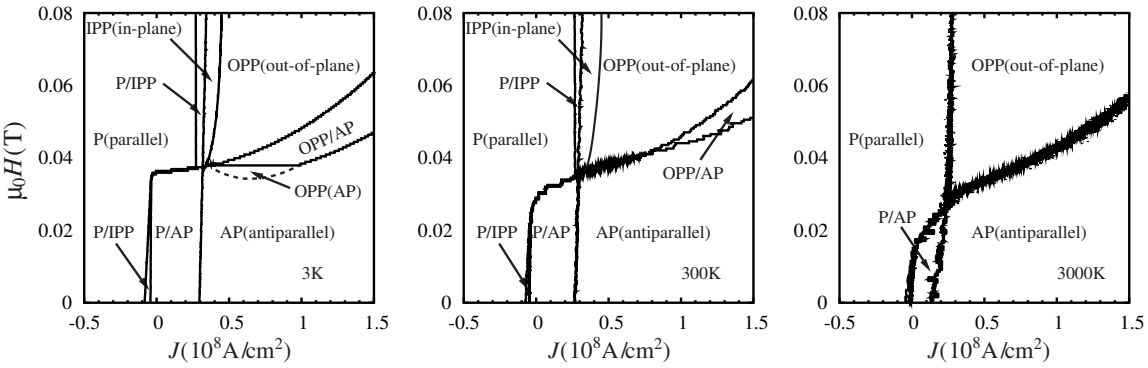

Figure 3.6: Minimal model dynamic phase diagrams for a Cu(80 nm)/Co(40 nm)/Cu(thin)/Co(3 nm)/Cu(10 nm) spin valve. Left panel: $T = 3$ K; middle panel: $T = 300$ K; Right panel: $T = 3000$ K. For fixed H, a bistable region labeled A/B exhibits the A state when J is scanned from left to right and the B state when J is scanned from right to left. The correspondence needed to compare with Ref. [32] is 10^8 A/cm^2 $\leftrightarrow$ 10 mA. The dashed curve is the OPP$\rightarrow$AP phase boundary for a field scan from large H to small H at fixed J.

like A/B is a signal that hysteresis is present.

The phase fields in Figure 3.6 are labeled P (parallel), AP (anti-parallel), IPP (in-plane precession) and OPP (out-of-plane precession). The static P and AP states are labeled by the relative orientation of **m** and **M**. The precessing states are identified from the microwave power (not shown) as described above. IPP denotes a dynamic state where **m** precesses symmetrically (or nearly so) around an axis that lies in the y-z easy plane. OPP denotes a dynamic state where **m** precesses symmetrically (or nearly so) around an axis that does not lie in the easy plane. Section 3.2.4 describes these states in more detail.

We focus first on the 3 K diagram. This is similar (but not identical) to $T = 0$ K diagrams published by others [32, 40] using the symmetric Slonczewski spin-transfer torque. Using sharp peaks in the measured noise power spectrum to identify states of stable precession, Kiselev *et al.* pointed out the topological similarity between their computed $T = 0$ K phase diagram and their measured $T = 300$ phase diagram [32].

When H exceeds the coercive field, our 3 K phase diagram shows hysteresis for the P$\leftrightarrow$IPP and OPP$\leftrightarrow$AP phase transitions. The experiment shows no hysteresis in this regime (see below). At low field, the P $\rightarrow$ AP transition occurs abruptly while the reverse-current AP $\rightarrow$ P transition does not. Instead, there is a long, skinny, triangular-shaped P/IPP

phase field within which the magnetization $\mathbf{m}$ exhibits stable, elliptical precession around the $-\hat{\mathbf{z}}$ axis. The precession amplitude increases as the current becomes more negative. The system crosses the phase boundary into the P phase when the precession angle between $\mathbf{m}$ and $-\hat{\mathbf{z}}$ exceeds 90° and the vector $\mathbf{m}$ spirals irreversibly toward $\hat{\mathbf{z}}$. We will see below that this asymmetry has its origin in the details of the dependence of the spin-transfer torque on the angle between the free layer and the fixed layer.

We draw special attention to the lower limit of the OPP/AP phase field in the 3 K phase diagram. The perfectly horizontal portion of this phase boundary is an artifact of the current scanning mode used to generate the diagram. If we fix J and scan the external field H from large values to small values, the OPP phase does not give way to the AP phase until the dashed line in the diagram is crossed. The exact shape of this boundary depends on the H-scan rate, but it is reasonable to suppose that the corresponding horizontal phase boundary found in Ref. [32] may also be an artifact of the method of taking data. [1]

Reading Figure 3.6 from left to right shows that the regions of hysteresis shrink as the temperature increases. More details can be seen in the line scans of Figure 3.7. The effect of increasing temperature is very similar to the effect of decreasing the current density sweep rate in Figure 3.5. Indeed, since our simulated current sweep rate is always much faster than experiment, the temperatures indicated on the phase diagrams in Figure 3.6 must be regarded as nominal. The true phase diagram at each temperature we show would exhibit less hysteresis. Equivalently, each panel actually corresponds to a lower physical temperature than the temperature we quote. Thus, our $T = 3000$ K diagram indicates (qualitatively) how the 300 K phase diagram might look if we could use current sweep rates comparable to those used experimentally. We note also that substantial Joule heating occurs in real spin valve samples, perhaps 15 K to 20 K per 10^7 A/cm^2 [38].

Our highest temperature simulation shows P↔AP hysteresis when H is small and complete reversibility when H is large. This resolves the disagreement between theory and experiment noted above. Moreover, state-to-state switching characterizes every reversible

[1] Ilya N. Krivorotov and Jack Sankey (private communication).

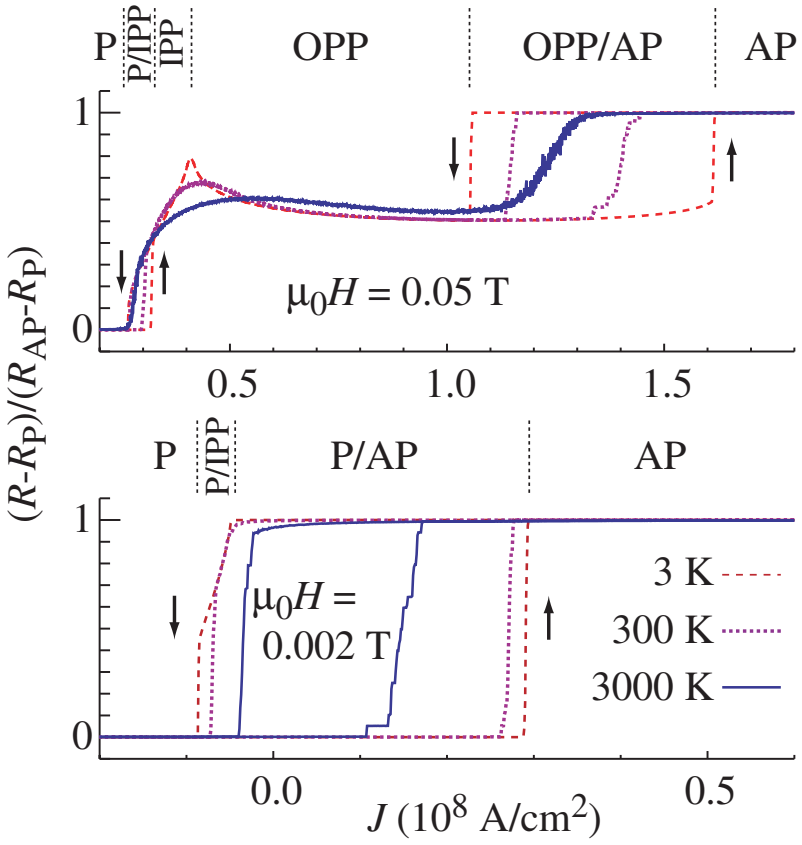

Figure 3.7: Temperature dependence of the magnetoresistance obtained by averaging the results of 20 realizations of the stochastic simulation. Upper panel: $\mu_0 H = 0.05$ T; Lower panel: $\mu_0 H = 0.002$ T.

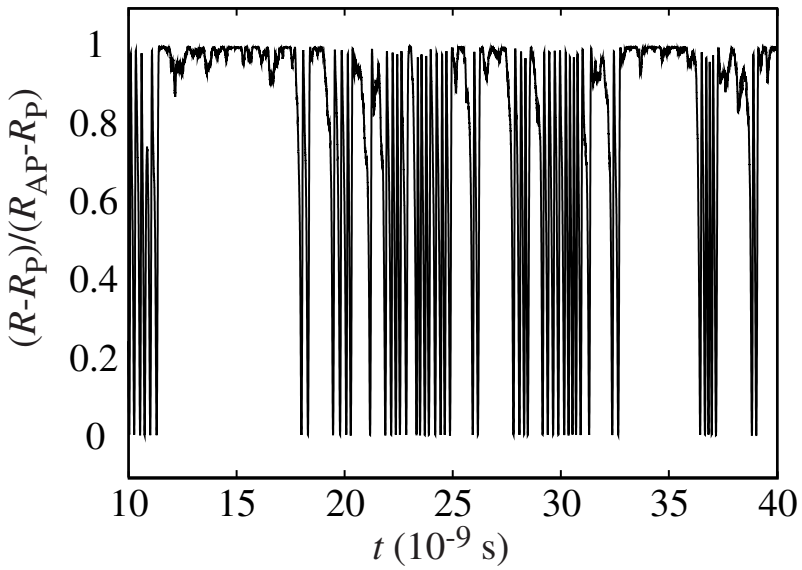

Figure 3.8: Telegraph noise in a time-series of the magnetoresistance. The data was collected on the high-temperature boundary between the AP phase and the OPP phase ($\mu_0 H = 0.04$T, $J = 0.7 \times 10^8$A/cm^2).

phase boundary. Figure 3.8 illustrates this for the dynamics of switching between the anti-parallel AP state and out-of-plane precession (OPP). The time-series data for the magnetoresistance was collected on the OPP/AP phase boundary at 3000 K. Clearly, the system switches back and forth between the AP state (small fluctuations around unit normalized resistance) and the OPP state (periodic oscillations of the normalized resistance between zero and one). Experiments show precisely this sort of telegraph noise [5, 36–38] if we replace the full scale excursions of the OPP resistance with small scale fluctuations around the average resistance of the OPP state. We are not aware of experiments that study the telegraph noise at our 300 K IPP/OPP boundary or our 3000 K P/OPP boundary. Indeed, at the latter, our simulations actually show random switching between *three* states: AP, IPP, and OPP.

The variations of the computed resistance near the 3000 K P/OPP and OPP/AP phase boundaries lead to two peaks in the differential resistance, $dIV/dI = R + I\ dR/dI$. These agree well with the peaks in dIV/dI observed experimentally. On the other hand, Kiselev *et al.* [32] identify a "W"-phase that is completely absent from our 3000 K phase diagram. However, the experimental W-phase field appears exactly where our model predicts OPP/AP phase bistability at 3 K and 300 K (two left panels of Figure 3.6). The experimental W-phase is microwave quiet above the experimental low frequency cut-off (0.1 gHz) and it exhibits a magnetoresistance that is slightly, but distinctly, smaller than that of the AP configuration. This would occur in our macrospin model if the free layer were frozen into a static configuration with $\mathbf{m}$ neither parallel nor anti-parallel to $\mathbf{M}$. We will return to the W-phase when we discuss micromagnetic simulations in Section 3.4.

Quantitatively, our calculated coercive field is about half the experimental value. This discrepancy may reflect an inaccurate description of the shape (and therefore the magnetostatic anisotropies) of the free layer. Another possibility is our complete neglect of dipolar coupling to the fixed layer. At low T, we also find that the magnitude of the critical current J_c^+ for the P→AP transition is much greater than the magnitude of the critical current J_c^- for the AP→P transition. Experiments show that J_c^+ and J_c^- are more symmetric around zero current. The calculated critical currents are determined by the angular derivatives of

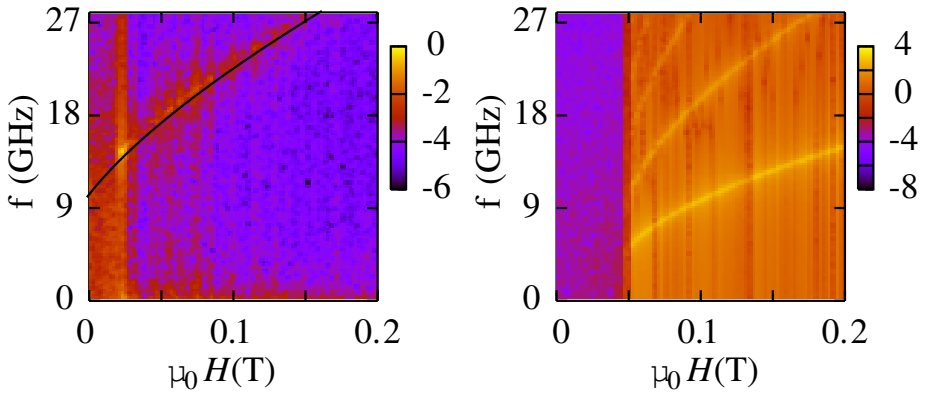

Figure 3.9: Relative microwave power at different frequencies as a function of field H at $T = 3\ K$. The gray/color scale is logarithmic. Left panel: $J = 0.3 \times 10^8 \mathrm{A/cm}^2$; the black curve is twice the resonance frequency given by the Kittel equation Eq. (3.14).

the torque for small angles around parallel and antiparallel. These quantities are [9] $\eta(0)$ and $\eta(180°)$ for the Slonczewski torques in Figure 3.4. A straightforward interpretation of the experimental results would imply that the actual torque is more nearly symmetric than would be implied by the transport calculations that have been done to date. On the other hand, our simulations at 3000 K more nearly resemble the experiments at 300 K because J_c^+ decreases strongly with temperature while J_c^- is nearly temperature independent.

3.2.3 Precession Frequency

The gray/color scale in Figure 3.9 quantifies the relative microwave power (on a logarithmic scale) at frequency f as a function of magnetic field for two values of current density J. The numerical data was obtained by Fourier transforming our simulated time series data for the magnetoresistance. The narrow bands of peak microwave power trace out the frequency $\omega(H)$ of stable precession (and its harmonics). The left panel corresponds to small-amplitude, noise-driven, in-plane precession at a value of current just before the parallel phase becomes unstable to steady in-plane-precession. As with the experimental data [6, 32], $\omega(H)$ in this regime can be described by the Kittel equation (black curve) for thin film magnetic resonance [83]. In the notation of Appendix A, the resonance frequency is

$$\omega_K = \gamma\sqrt{[H + (h_Y - h_Z)M_\mathrm{s}][H + (h_X - h_Z)M_\mathrm{s}]}. \tag{3.14}$$

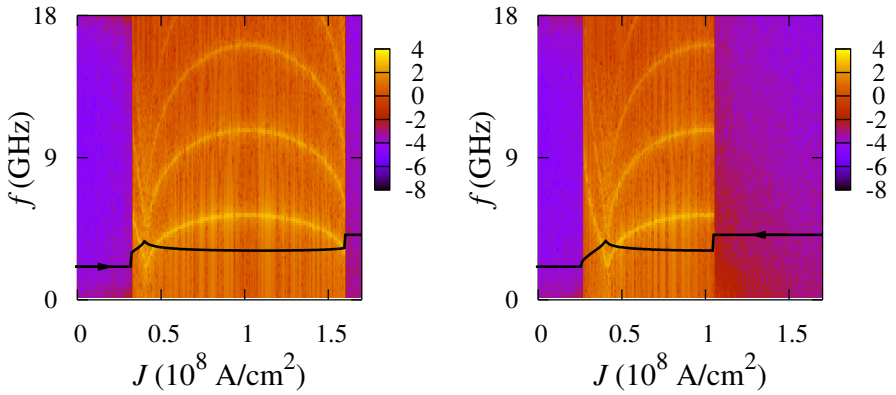

Figure 3.10: Microwave power at different frequencies as a function of J at $T = 3$ K and $\mu_0 H = 0.05$ Tesla. The gray/color scale is logarithmic. Left panel: current scan from left to right. Right panel: current scan from right to left. The narrow bands of peak power represent the frequency $\omega(J)$ of stable precession. The black traces are the magnetoresistance in arbitrary units.

Our simulation data agree with $2\omega_K$ because the periodicity of the resistance is twice the periodicity of the magnetization oscillation frequency. No analytic theory is available for comparison with our results at a higher value of J (right panel) where large amplitude out-of-plane precession occurs. But our results do show the same relative magnitude and H-dependence as seen in the experiments.

Figure 3.10 shows the relative microwave power at frequency f as a function of increasing J (left panel) and decreasing J (right panel). Similar plots for comparison with experiment have been presented by others using the symmetric Slonczewski torque [32] and the sine torque [48]. The zero power regions at low and high J correspond to the static P and AP magnetization states. In between, the narrow bands of peak microwave power trace out $\omega(J)$ (and its harmonics) for stable precession. Just above the limit of the parallel state, there is a very narrow range of in-plane precession where $\omega(J)$ decreases monotonically. At slightly higher J, the system evolves to a state of out-of-plane precession (OPP) where $\omega(J)$ first increases and then decreases. Comparison of the two panels in Figure 3.10 illustrates the hysteresis present at this low temperature.

Our results for $\omega(J)$ do not agree with observations for real spin valves. [6, 32] Putting aside the fact that no hysteresis is seen in the experiments (which we attribute to the current sweep rate as discussed above), the experimental data always show that ω decreases as J

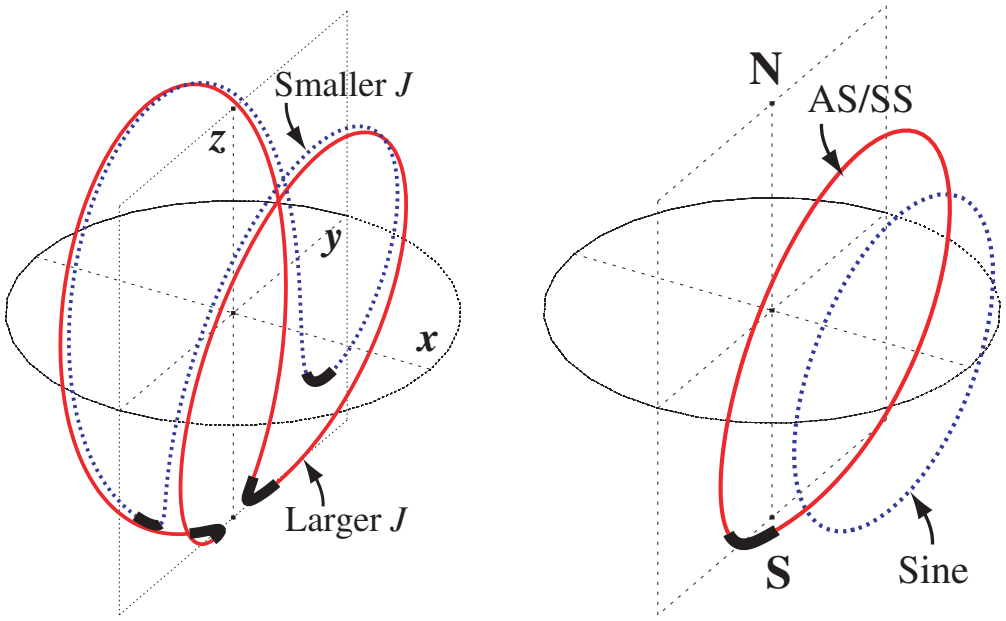

Figure 3.11: Left: In-plane precession (IPP) orbits for two nearby values of J. The thick segments are points on each orbit where the magnitude of the demagnetization field $\mathbf{H}_d = -h_X \hat{m}_x \hat{\mathbf{x}}$ is smaller than the magnitude of the external field $\mathbf{H} = H\hat{\mathbf{z}}$. The y-z easy plane and the equatorial circle of the unit sphere in the x-y plane are indicated as guides to the eye. Right: Out-of-plane precession (OPP) orbits. The geometry is the same as Figure 3.11 except that the north (N) and south (S) poles of the unit sphere are indicated. The orbit labeled "AS/SS" is produced by Slonczewski's spin-transfer torque. Along the thick segment, the spin-transfer torque and demagnetization field torque point in opposite directions. The orbit labeled "sine" is produced by a sine-type spin-transfer torque for the same value of J.

increases. Naively, it is as if in-plane precession persisted all the way to the anti-parallel state with no intervening state of out-of-plane precession. This is a serious issue because, in our model, in-plane precession occupies an extremely small portion of the J-H phase diagram.

3.2.4 Precession Trajectories

To help shed light on our simulation results for $\omega(J)$, it is instructive to analyze the relationship between this quantity and the trajectory of the tip of $\hat{\mathbf{m}}$ on the unit sphere. We will call this the orbit of the precessional motion. Without loss of generality, we set $h_Y = h_Z = 0$ and retain only the external field $\mathbf{H} = H\hat{\mathbf{z}}$ and the *local*, out-of-plane demagnetization field $\mathbf{H}_d = -h_X \hat{m}_x \hat{\mathbf{x}}$. It is crucial that the magnitude H_d changes along the trajectory because the component $\hat{m}_x$ of $\hat{\mathbf{m}}$ changes along the trajectory.

It is common to think of precession as the steady motion of a vector on a cone that makes a small angle with respect to its symmetry axis. The orbit in this case is a circle. The precessional states in the present problem are more complicated. The left panel in Figure 3.11 shows two large amplitude, saddle-shaped, in-plane precession (IPP) orbits for two nearby values of J. We call these "in-plane" precession modes because each orbit moves symmetrically (or nearly so) around an axis (the z-axis) that lies in the easy y-z plane.

Let us partition each orbit into two segments. The short thick segments lie near the easy plane where the demagnetization field H_d is smaller than the external field H. Along these segments, the orbital azimuthal angle ϕ precesses mainly around $\mathbf{H}$ with angular speed γH. Along the remaining segment of each orbit, H_d is larger than H and the orbital polar angle θ precesses mainly around $\mathbf{H}_d$ with angular speed γH_d. The left panel in Figure 3.11 shows that the angular range swept out by *both* the thick and thin segments increases as the current density (and the spin-transfer torque) increases, *i.e.*, the total arc length of the orbit increases. Since the orbital speeds change very little with J, we conclude that the orbital period increases as current density increases. This implies that $\omega(J)$ is a decreasing function for in-plane-precession orbits.

As J continues to increase, the apices of the two thick segments of the in-plane precession saddle orbit approach and then touch one another near the negative z-axis. When this occurs the orbit bifurcates into two elliptical orbits, each centered on an out-of-plane axis not far from the x-axis. [32, 47, 48, 84] Precessional states at higher current density correspond to one or the other of these out-of-plane (OPP) trajectories, *e.g.*, the AS/SS orbit in the right panel of Figure 3.11. This orbit precesses mostly around $\mathbf{H}_d$. Spin-transfer torque tends to push the orbit away from the easy plane in the northern unit hemisphere. The effect on the orbit in the southern unit hemisphere is more complex. The net result is that the "center" of the orbit moves away from the easy plane. In other words, as the current density increases, the component $\hat{m}_x$ of $\hat{\mathbf{m}}$ increases, which increases H_d, and thus increases the frequency γH_d of the orbit.

Along the thick segment of the out-of-plane orbit, the spin-transfer torque and the torque from the demagnetization field point in (nearly) opposite directions. This means that the net

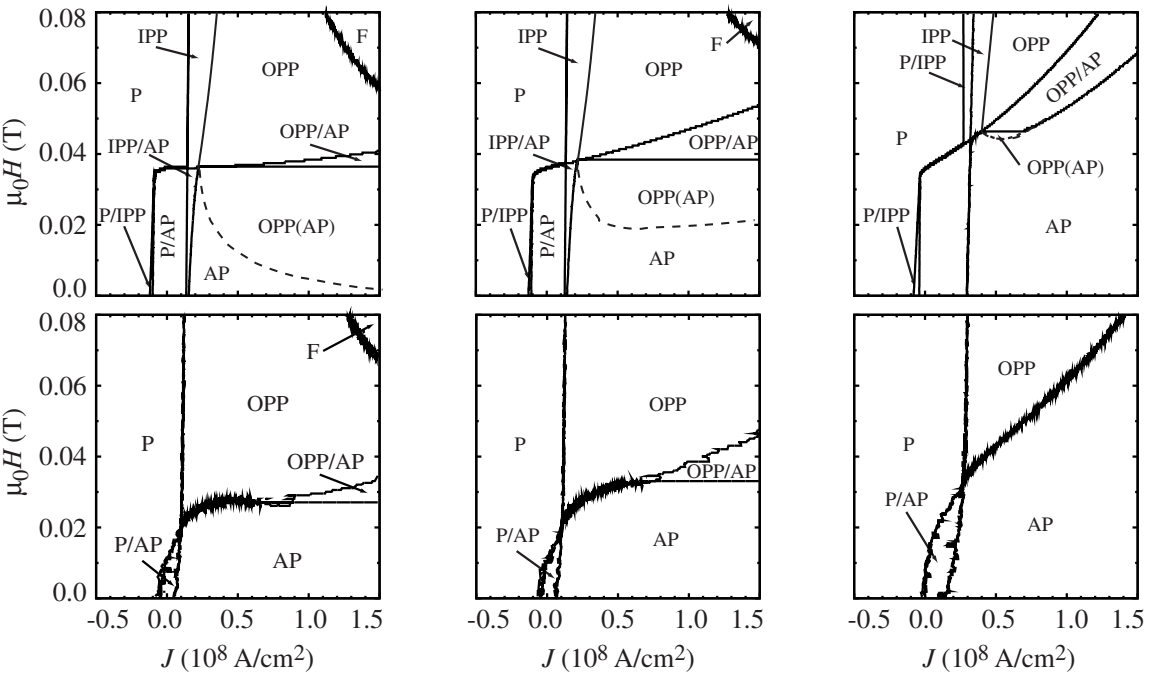

Figure 3.12: Phase Diagrams at 3 K (top panels) and 3000 K (bottom panels). Left panel: sine torque; middle panel: sine torque plus current-induced effective field; right panel: Slonczewski torque plus current-induced effective field. For fixed H, a bistable region labeled A/B exhibits the A state when J is scanned from left to right and the B state when J is scanned from right to left. The dashed curves are the OPP→AP phase boundaries for a field scan from large H to small H at fixed J.

torque, and thus the orbital speed along that segment, decreases as J increases. Eventually, this slowing down overwhelms the speeding up described just above and the total orbital period begins to increase. This is why $\omega(J)$ decreases for the largest values of J where precession occurs in the left panel of Figure 3.10.

3.3 Beyond the Minimal Model

There are two major discrepancies between the Cornell experiment [32] and our minimal model results: the variation of the precession frequency ω with current density J and the absence of a microwave quiet "W-phase". Within the context of the macrospin model, we examined several variations of our model, mostly with the hope they would improve the agreement between theory and experiment. We studied the influence of (A) a sine-type spin transfer torque for the standard geometry; (B) asymmetric vs. symmetric Slonczewski spin-transfer torque for a special asymmetric geometry; (C) the current-induced effective

field that arises due to incomplete absorption of transverse spin currents; (D) spin-pumping; and (E) angle-dependent Gilbert damping.

3.3.1 Sine Spin-Transfer Torque

Figure 3.4 shows the geometry-independent "sine" torque that is widely used in the literature. The top left panel in Figure 3.12, shows the 3 K phase diagram when this sine torque replaces the AS/SS torque. Several differences with the corresponding Slonczewski torque phase diagram (left panel of Figure 3.6) should be noted.

First, with a sine torque, the low-field P→AP transition is mediated by in-plane precession in the same way that precession mediates the AP→P transition for both the sine and Slonczewski torques. This occurs because $\sin\theta$ is symmetric around $\theta = \pi/2$ while the minimal model torque is not. Second, the sine torque generates no hysteresis in the high-field transitions P↔IPP and IPP↔OPP. Third, the lower limit of the OPP phase boundary determined by a field scan from large H to small H (dashed curve) greatly reduces the size of the AP phase field compared to the Slonczewski case. This feature does not appear to have been noticed in previous discussions of this phase diagram [46, 47].

Unlike the Slonczewski torque, increasing current or field eventually drives the sine torque model to a transition from out-of-plane precession (OPP) to a static phase where the macrospin $\mathbf{m}$ is "fixed" (F) at some angle between zero and π. This is intriguing because the magnetoresistance and microwave power characteristics of this phase match exactly to those of the experimentally observed "W-phase". Unfortunately, the location of the F phase in the sine torque phase diagram does not agree with the location of the W-phase in the experimental phase diagram (see the penultimate paragraph of Section 3.2.2)

The bottom left panel in Figure 3.12 shows the 3000 K phase diagram for the sine torque macrospin model. Compared to the corresponding diagram for the minimal model (right panel of Figure 3.6), thermal effects eliminate OPP/AP bistability only when J is small. Hysteresis between these phases remains when J is large. In this sense, the sine torque model is more resistant to thermal fluctuations than the Slonczewski torque model.

Finally, the out-of-plane precession frequency for the sine torque is a strictly increasing

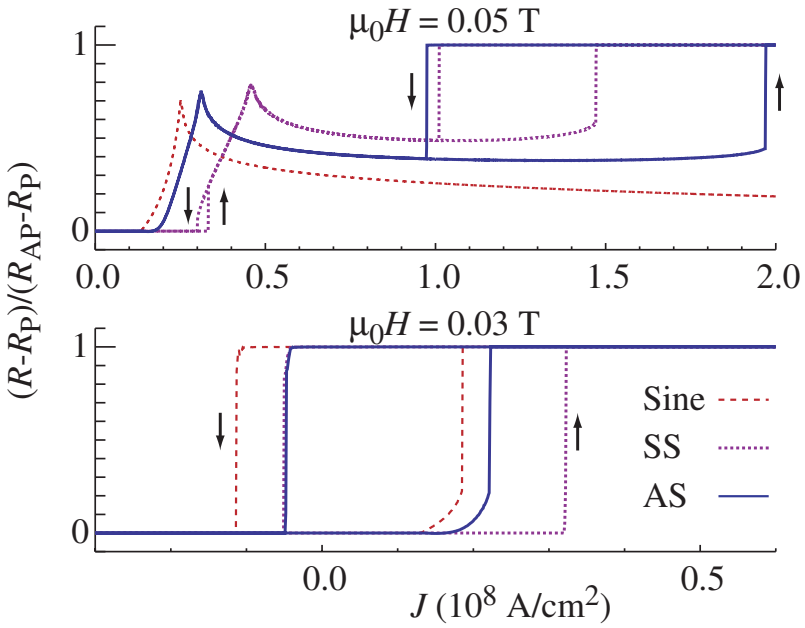

Figure 3.13: Spin valve hysteresis at 3 K for three choices of spin transfer torque using a geometry (defined in Sec. 3.3.2) chosen to emphasize the difference between the AS and SS torques. Lower panel: $H = 0.03$T; Upper panel: $H = 0.05$T.

function of J. The argument is similar to the one in Section 3.2.4 for the Slonczewski torque. However, as the current increases, the different angular dependence of the sine torque causes the orbit of $\hat{\mathbf{m}}$ to push steadily away from the easy plane everywhere and contract on the unit sphere (see Figure 3.11). The frequency γH_d increases monotonically because the demagnetization field H_d increases. The outward motion and areal contraction of the orbit continues as the current increases until the orbit area shrinks to a single point on the unit sphere. This is the signature of the fixed (F) phase.

3.3.2 AS vs. SS Spin-Transfer Torque

The AS/SS curve in Figure 3.4 shows that the asymmetric Slonczewski torque used in our minimal model is essentially identical to the symmetric Slonczewski torque for the spin valve geometry of Ref. [32]. This is not always the case. For example, compared to the geometry of Kiselev *et al.* [32], a spin valve with film thicknesses,

Cu(10 nm)/Co(40 nm)/Cu(thin)/Co(3 nm)/Cu(180 nm),

is very asymmetric. The Cu/Co bilayers on opposite sides of the spacer layer are very different: the left bilayer is mostly ferromagnet, the right bilayer is mostly non-magnet. The difference between the symmetric and asymmetric Slonczewski torques for this geometry is still small (compare the two dashed curves in Figure 3.4). Nevertheless, it is large enough to produce small-angle, in-plane precession that "rounds" the low-to-high resistance jump in the AS hysteresis curve at the P→AP transition in the lower panel of Figure 3.13. The same panel shows similar precessional rounding for the sine-type spin-transfer torque. However, the latter rounding disappears when shape anisotropy is turned off. The corresponding rounding for the asymmetric Slonczewski torque does *not* disappear when shape anisotropy is turned off [82].

Figure 3.13 also shows that the critical current J_c^+ for the P→AP transition differs for all three spin-transfer torques while the critical current J_c^- for the reverse AP→P transition distinguishes only the sine torque. This is a consequence of the fact that J_c^+ (J_c^-) is inversely proportional the slope of the torque function $\eta(\theta)\sin\theta$ (plotted in Figure 3.4) at $\theta = 0$ ($\theta = \pi$) [9]. The fact that J_c^+ is smaller for the AS torque than for the SS torque suggests that an asymmetric geometry like the one above may be desirable for some applications.

3.3.3 Current-Induced Effective Fields

We mentioned in Section 3.1.5 that a current-induced torque that acts like an effective external magnetic field can arise due to incomplete absorption of a transversely polarized spin current at the interface between the spacer and the free layer. A recent experimental report [41] has been interpreted by its authors to mean that the size of this torque — displayed in Eq. (3.10) — is much larger than theoretical estimates. Accordingly, Figure 3.12 shows how the spin valve 3 K phase diagram changes if we augment the sine torque (top middle panel) and the minimal model torque (top right panel) by an effective field torque that is 20% of the spin-transfer torque, as suggested by this experiment. For comparison, the bottom middle and bottom right panels respectively show the phase diagrams for these two situations at 3000 K. We find that the topology of the phase diagram does not change, although the precise positions of the phase boundaries do. The qualitative behavior of the

precession frequencies is not affected.

3.3.4 Spin-Pumping

The original discussion of spin-pumping [81] focused on the enhancement of Gilbert damping that occurs when a normal metal is in intimate contact with a precessing thin film ferromagnet. Subsequent work [60] has emphasized that the torque due to spin-pumping is generally of the same order of magnitude as spin-transfer torques. Since the analytic form of the torque $\mathbf{N}_{\rm sp}$ in Eq. (3.11) differs considerably from simple damping for, *e.g.*, large-angle, out-of-plane precessional motion, this raises the possibility that spin-pumping alters the dynamical behavior of a spin valve more profoundly than merely enhancing the Gilbert damping.

In the small angle limit, the parameters for intrinsic Gilbert damping and spin-pumping suggested in Ref. [60] for the Co/Cu/Co system (Table I) produce a total effective Gilbert damping of $\alpha_{\rm eff} = 0.148$. Therefore, in Figure 3.14, we compare the phase diagram at 3 K obtained with our minimal model (no spin pumping) using $\alpha = \alpha_{\rm eff}$ (solid lines) with the phase diagram obtained including both (reduced) Gilbert damping and the spin-pumping torque density $\mathbf{N}_{\rm sp}$ (dashed lines). The small differences we find between the two show that spin-pumping does not much affect the sort of precessional motion produced by our minimal model. There is also no qualitative change in the current dependence of the precession frequency. We conclude that neither effective fields nor spin pumping affects improves the agreement between experiment and the minimal model.

3.3.5 Angle-Dependent Gilbert Damping

The numerical value of the Gilbert damping constant α in 3.2 is usually extracted from ferromagnetic resonance or Brillouin light scattering experiments [63]. Since the magnetization is never tilted far from equilibrium in these situations, it is relevant that Back *et al.* [85] reported an effective increase in the damping constant for large magnetization rotation angles in cobalt films under pulsed field conditions. More recent pulsed-field experiments have been successfully analyzed using conventional Gilbert damping [86, 87]. Since transient magnetization dynamics is a common feature of all these experiments, it is not obvious

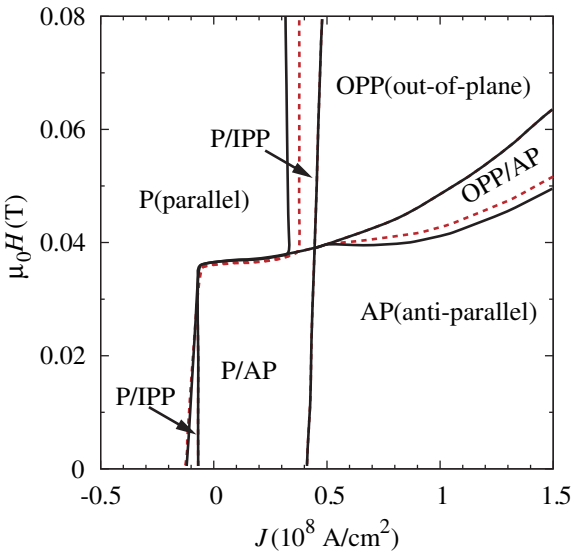

Figure 3.14: Minimal model phase diagram at 3 K with Gilbert damping only (solid lines) and spin-pumping with reduced Gilbert damping (dashed lines). See text for discussion.

that the results address the validity of the constant α approximation for large-angle, steady precession of the sort discussed in this chapter. With one exception [3], we are unaware of any models that allow the damping constant to vary during the course of precession.

A glance back at Figure 3.9 shows that the precession frequency $\omega(J)$ decreases monotonically (as seen in experiment) for in-plane-precession and also for out-of-plane precession near the boundary with the anti-parallel state. Using the damping "constant" *ansatz*

$$\alpha(\theta) = a + b \sin^2 \theta, \tag{3.15}$$

we have been able to produce dynamical phase diagrams with (i) only in-plane-precession or (ii) only out-of-plane precession with (in both cases) the "correct" behavior for $\omega(J)$, or nearly so. Unfortunately, other features appear in the simulated phase diagram that do not appear in the data, *e.g.*, an extended region of precession when the external field H is less than the coercive field. It may be possible to fine-tune the phase diagram to the desired form, but this seems unwarranted without some justification for Eq. (3.15) and the relative paucity of theoretical information about damping far from equilibrium [88].

3.4 Micromagnetics

Our macrospin approach to the Landau-Lifshitz-Gilbert (LLG) equation replaces the free layer magnetization $\mathbf{m}(\mathbf{r})$ by a constant vector $\mathbf{m}$. The numerical method of micromagnetics is a better approximation to reality because it retains spatial gradients of $\mathbf{m}(\mathbf{r})$ down to a fixed minimum length scale. Treating the spatial variation of the magnetization allows the inclusion of two effects that we have neglected because they do not contribute when the magnetization is uniform. First, the experimental samples are polycrystalline so we ignore any intrinsic magnetocrystalline anisotropy because the non-uniform effective fields tend to average to zero over the whole sample. Second, the Oersted magnetic field produced by the current itself largely averages to zero over the whole sample. While these two effects are not important for the macrospin dynamics we have considered here, full simulations [55] show that the inhomogeneities in the magnetization that result can be quite important.

There is an emerging consensus amongst micromagnetic practitioners [49–55, 89] that the inclusion of spin-transfer torque excites incoherent spin waves in the free layer (and thus inhomogeneous magnetization) if the current density is sufficiently great to induce switching and microwave emission. However, since the method takes full account of local exchange and non-local magnetostatics, systematic survey calculations of the sort we have presented in this chapter are prohibitively expensive, even for systems as small as a spin valve free layer. Using a torque density $\mathrm{N_{st}} \propto \sin\theta$ to model spin-transfer, Ref. [52] reports zero-temperature micromagnetic simulations designed to mimic the experimental conditions reported by Kiselev *et al.* [32] Like our Figure 3.6, the calculated phase diagram agrees topologically and semi-quantitatively with the experimental diagram, with one important improvement. The micromagnetics simulation identifies the experimental "W-phase" with a dynamical phase field where vortices of magnetization continuously form and annihilate. The calculated noise power in this regime is concentrated at very low frequency and thus appears to be microwave quiet in the experiment.

It seems plausible that the extra degrees of freedom present in the micromagnetic approximation allow the bistable OPP/AP phase present in our macrospin model to break up into a spatially inhomogeneous state. The same logic suggests that the fixed F phase of

the macrospin sine torque phase diagram breaks up similarly into a state of inhomogeneous magnetization. On the other hand, the micromagnetic simulation produces a nearly horizontal line for the AP phase boundary that we identify as an artifact of the current-scanning mode of data collection.

It is worth noting that the microwave power output in this micromagnetic calculation is nearly independent of J in the high-field precession regime (as we find for a macrospin) while the power output observed experimentally varies considerably in this part of the phase diagram. The precession frequency $\omega(J)$ in the same regime has been studied by Berkov and Gorn [55], who find that they are able to qualitatively reproduce the experimental frequency dependence with a highly inhomogeneous magnetic state. The inhomogeneous state arises from the non-uniform Oersted field and an (assumed) random distribution of granular magnetocrystalline anisotropy. It would be interesting to discover if this type of micromagnetic simulation can produce resonance linewidths with $Q \approx 100$ as observed in the most recent nanopillar experiments [35].

3.5 Summary & Conclusion

In this chapter, we have studied the Landau-Lifshitz-Gilbert (LLG) dynamics of a single macrospin as a model for current-driven magnetization motion in the free layer of a spin valve. We parameterized our model specifically to compare our results with those reported by Kiselev *et al.* [32] for a Cu/Co/Cu nanopillar. Due to the simplicity of the model (compared to micromagnetics), we were able to explore systematically the effects of temperature, spin-pumping, current-induced effective fields, various forms of spin-transfer torque, and angle-dependent damping. We focused most of our attention on a "minimal model" where Slonczewski's spin-transfer torque supplements the terms usually found in the LLG equation.

Low-Field Behavior: Our minimal macrospin model captures the essential features of the experiment when the external field H does not exceed the coercive field of the free layer. As a function of current density J, there is hysteretic switching between parallel and anti-parallel orientations of the free layer and the fixed layer. In the experiment, the

critical currents for P→AP and AP→P switching have opposite sign but are approximately equal in magnitude . This is not a feature of our $T = 3$ K phase diagram, but it is much more nearly true in our simulation at 3000 K, where thermal fluctuations are large enough to mimic the effect of the (slow) current sweep rate used in the experiment. The scale we calculate for H is about half as large as seen in the experiment.

High-Field Behavior: The macrospin model correctly models noise-driven, low amplitude, in-plane precession when H is larger than the coercive field and the current density is low. The existence of large-amplitude, in-plane and out-of-plane precession at higher J agrees qualitatively with observation, but the precession frequency function $\omega(J)$ is not monotonically decreasing as found in experiment. The simulation predicts peaks in dIV/dI associated with telegraph-noise switching between two (or more) states of magnetization. These peaks are present in the experiment, as is two-state telegraph noise. We find an OPP/AP bistable phase field that is occupied in the experiment by a microwave quite "W"-phase. Micromagnetic simulations by others suggest that that vortex creation and annihilation occurs in this phase field.

Other Effects: The phase diagram of the sine-torque model differs mostly in detail with the phase diagram of the minimal model. An exception is the presence of a high-field, high current "fixed" phase for the sine torque where the macrospin freezes into a fixed angle with respect to the fixed layer. This phase does not seem to occur in micromagnetic simulations. Another exception is the relative persistence of the OPP phase when we scan from high values of H to low values of H. This behavior is also absent from the micromagnetics simulations. Spin-pumping and current-induced magnetic fields do not change the phase diagram in any significant way. Large topologically changes do occur if we allow the Gilbert damping parameter to change with angle, but we have no guidance for the form $\alpha(\theta)$ should take. This seems like a fruitful direction for future research.

CHAPTER IV

SPIN-TRANSFER TORQUE FOR VARIABLE MAGNETIZATION

In the previous chapters, we focused on spin-transfer in a spin valve. There, a single domain ferromagnet feels a torque because it absorbs the component of an incident spin current that is polarized transverse to its magnetization. The same idea generalizes to systems with continuously non-uniform magnetization [44, 90]. This realization has generated a flurry of experimental [10–19] and theoretical work [91–97] focused on current-driven motion of domain walls in magnetic thin films.

The magnetization in a domain wall generally can be described by

$$\mathbf{M} = M_s(\sin\theta\cos\phi, \sin\theta\sin\phi, \cos\theta), \tag{4.1}$$

where θ and ϕ denote the spacial orientation of the magnetization in some frame, and M_s is the saturation magnetization of the material. Figure 4.1 shows a cartoon picture of a one dimensional Néel type domain wall [1] along the x axis where the magnetization rotates in the x-z plane from one domain to the other. If we define θ as the polar angle measured from the positive z axis and ϕ as the azimuthal angle in x-y plane, this wall can be described by Eq. (4.1) with

$$\theta(x) = -\arcsin\left[\tanh\left(\frac{x}{w}\right)\right] + \frac{\pi}{2}, \qquad \phi(x) = 0. \tag{4.2}$$

[1] Néel type domain wall is one in which the magnetization rotation axis is perpendicular to the domain wall direction (x-direction in Figure 4.1).

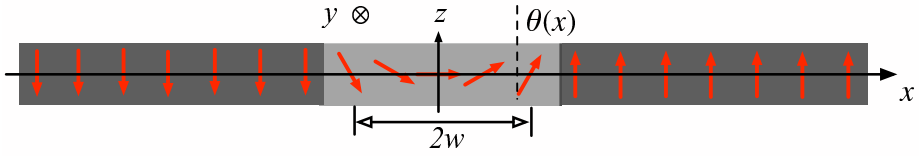

Figure 4.1: Cartoon of a Néel type domain wall.

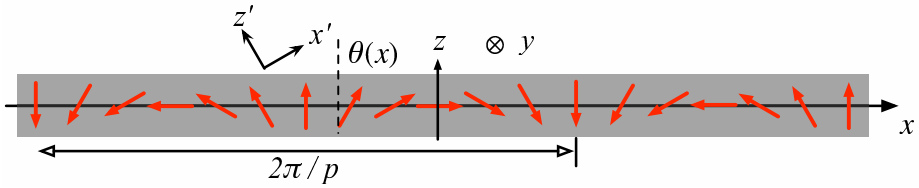

Figure 4.2: Cartoon of a spin spiral.

The parameter w is called the domain wall width.

Because of the complicated form of θ in Eq. (4.2), some theorists study a domain wall with a simpler form of θ which is a linear function of x inside the wall:

$$\theta(x) = \begin{cases} \pi, & x < -w \\ \dfrac{\pi}{2}\left(1 - \dfrac{x}{w}\right), & -w \le x \le w \\ 0, & x > w. \end{cases} \tag{4.3}$$

Even the domain wall defined by Eq. (4.3) is sometime too complicated, so we also study an even simpler magnetic structure — a spin spiral. A spin spiral is a helical magnetic structure where the direction of the magnetization rotates continuously as one moves along a fixed axis in space. Spin spirals occur in the ground state of some rare earth metals [98] and also for the γ phase of iron [99]. Figure 4.2 shows a cartoon picture of a spin spiral where the magnetization rotates uniformly in the x-z plane of a fixed coordinate system with $\hat{\mathbf{M}}(x) \cdot \hat{\mathbf{z}} = \cos\theta$. The inset shows a local coordinate system where $\mathbf{M}(x)$ always points along the z' axis. This spin spiral can be described using Eq. (4.1) with

$$\theta(x) = p\,x \qquad \text{and} \qquad \phi(x) = 0, \tag{4.4}$$

where θ and ϕ have the same definition as in domain walls.

The experiments cited at the beginning of this chapter employ Néel-type domain walls with widths $w \approx 100$ nm. This length is very large compared to the characteristic length scales of the processes that determine the local torque [8, 100]. Therefore, it is appropriate to adopt an adiabatic approximation where the spin current is assumed to lie parallel to the local magnetization [44, 90]. Surprisingly, the adiabatic prediction for the current dependence of the domain wall velocity [93, 101, 102] agrees very poorly with experiment. This has led theorists [91–95] to consider non-adiabatic effects and experimenters [103, 104]

to study systems with domain wall widths that are much shorter ($w \approx 10$ nm) than those studied previously.

Two groups [92, 102] have studied the effect on domain wall motion of a distributed spin-transfer torque represented by a sum of gradients of the local magnetization with constant coefficients. For a one-dimensional magnetization $\mathbf{M}(x)$, the torque function can be written in terms of two vectors perpendicular to the magnetization

$$\mathbf{N}_{\mathrm{st}}(x) = c_1 \partial_x \hat{\mathbf{M}} + c_2 \hat{\mathbf{M}} \times \partial_x \hat{\mathbf{M}}. \tag{4.5}$$

In general, the coefficients c_1 and c_2 are functions of position. The well-established adiabatic piece of the torque is the first term in Eq. (4.5) with a constant coefficient. Consistent with usage in the literature, we call all deviations from the adiabatic torque non-adiabatic. Any contributions of the second term are then called non-adiabatic. Zhang and Li [92] derive a contribution along this second direction in Eq. (4.5) from a consideration of magnetization relaxation due to spin-flip scattering in the context of an s-d exchange model of a ferromagnet. [100, 101] Their arguments lead them to the estimate $c_2/c_1 \approx 0.01$. The authors of Ref. [94] report that a similar value of c_2/c_1 produces agreement with experiment when Eq. (4.5) is used in micromagnetic simulations.

In this Chapter, we study the applicability of Eq. (4.5) to a free-electron Stoner model for a domain wall and a spin spiral structure. We begin with the spin spiral. This system turns out to be perfectly adiabatic; the torque is described by Eq. (4.5) with $c_2 = 0$. The same is true for realistic domain walls of the sort usually encountered in experiment. Non-adiabatic effects appear only for very narrow walls. In that case, we find that the torque is non-local and cannot be written in the form Eq. (4.5). The non-adiabatic torque decreases exponentially as the wall width increases for all realistic domain wall profiles. Finally, our analysis casts doubt on the existence of the Zhang-Li non-adiabatic contribution to the torque mentioned above.

This Chapter is organized as follows. Section 4.1 describes our Stoner model and the

methods we use to calculate the spin current and the spin-transfer torque. Section 4.2 reports our results for an infinite spin spiral and Section 4.3 does the same for one-dimensional domain walls that connect two regions of uniform magnetization. Section 4.4 relates these calculations to previous work by others. Section 4.5 discusses the effects of scattering. We summarize our results and offer some conclusions in Section 4.6. Appendix B and Appendix C provide some technical details omitted in the main body of the Chapter.

4.1 Model & Methods

The free electron Stoner model provides a first approximation to the electronic structure of an itinerant ferromagnet. The Hamiltonian is

$$H = -\frac{\hbar^2}{2m}\nabla^2 - \mu\boldsymbol{\sigma}\cdot\mathbf{B}_{\rm ex}(x), \tag{4.6}$$

where $\boldsymbol{\sigma} = (\sigma_x, \sigma_y, \sigma_z)$ are the three Pauli matrices and $\mu = g\hbar e/2m$. The magnetic field $\mathbf{B}_{\rm ex}(x)$ is everywhere parallel to $\mathbf{M}(x)$ but has a constant magnitude. [2] That magnitude is chosen so the Zeeman splitting between the majority and minority spins bands reproduces the quantum mechanical exchange energy in the limit of uniform magnetization:

$$E_{\rm ex} = 2\mu|\mathbf{B}_{\rm ex}| = \hbar^2 k_B^2/m. \tag{4.7}$$

If $E_F = \hbar^2 k_F^2/2m$ is the Fermi energy, the constant k_B in Eq. (4.7) fixes the Fermi wave vectors for up and down spins, k_F^+ and k_F^-, from

$$k_F^\pm = \sqrt{k_F^2 \pm k_B^2}. \tag{4.8}$$

Given $\mathbf{B}_{\rm ex}(x)$, we use both quantum mechanics and a semi-classical approximation to calculate the spin accumulation, spin current density, and spin-transfer torque. The building blocks are the single-particle spin density $\mathbf{s}_\pm(x, k_x)$ and the single-particle spin current density [3] $\mathbf{Q}_\pm(x, k_x)$ for an up/down ($\pm$) electron with longitudinal wave vector k_x.

[2] In reality, the magnetization is oppositely directed to the spin density since the g factor for electrons is negative. For simplicity, we ignore this sign difference and assume that the magnetization is parallel to the spin density. Care is required when using spin currents to compute torques on magnetizations.

[3] The spin current density is a tensor quantity (Ref. [8]). However, since the current defines the only relevant direction in space for this problem, we suppress this dependence and use the components of the vector $\mathbf{Q}$ to denote the Cartesian components of the spin degree of freedom in the spin current density.

Summing over all electrons and using the relaxation time approximation gives the non-equilibrium majority and minority spin density $\mathbf{s}_\pm(x)$ and spin current density $\mathbf{Q}_\pm(x)$ in the presence of an electric field $E\hat{\mathbf{x}}$:

$$\mathbf{s}_\pm(x) = \int \left[f_\pm(\mathbf{k} - \frac{eE\tau}{\hbar}\hat{\boldsymbol{x}}) - f_\pm(\mathbf{k}) \right] \mathbf{s}_\pm(x, k_x) d^3\mathbf{k} \tag{4.9a}$$

$$\mathbf{Q}_\pm(x) = \int \left[f_\pm(\mathbf{k} - \frac{eE\tau}{\hbar}\hat{\boldsymbol{x}}) - f_\pm(\mathbf{k}) \right] \mathbf{Q}_\pm(x, k_x) d^3\mathbf{k} \tag{4.9b}$$

Our use of the function $f_\pm(\mathbf{k}) = \Theta(k_F^\pm - |\mathbf{k}|)$ implies that the distribution of electrons outside the region of inhomogeneous magnetization are characteristic of the zero-temperature bulk. [4] We shall expand this point and comment on the general correctness of Eq. (4.9) in Section 4.5.

The sum $\mathbf{s}(x) = \mathbf{s}_+(x) + \mathbf{s}_-(x)$ is the total spin accumulation (spin density) and $\mathbf{Q}(x) = \mathbf{Q}_+(x) + \mathbf{Q}_-(x)$ is the total spin current density. Finally, the distributed spin transfer torque is (see Eq. (1.5))

$$\mathbf{N}_{\rm st}(x) = -\partial_x \mathbf{Q}(x). \tag{4.10}$$

The adiabatic approximation [90] to the spin dynamics leads to a spin current density that is proportional to the local magnetization, $\mathbf{Q}_{\rm ad}(x) \propto \mathbf{M}(x)$. This means that

$$\mathbf{N}_{\rm ad}(x) \propto \partial_x \mathbf{M}(x). \tag{4.11}$$

A main goal of this chapter is to study the extent to which the spin-transfer torque associated with real domain wall configurations satisfies Eq. (4.11).

4.1.1 Quantum

In light of Eq. (4.1), the exchange magnetic field that the enters the Hamiltonian in Eq. (4.6) is

$$\mathbf{B}_{\rm ex}(x) = B_{\rm ex} \left(\sin\theta\cos\phi, \sin\theta\sin\phi, \cos\theta \right). \tag{4.12}$$

[4] When $E\tau$ is sufficiently small, as we assume here, the difference in the square brackets in Eq. (4.9) is zero except in the immediate vicinity of the Fermi surface. In this limit, the integral over reciprocal space in Eq. (4.9) reduces to an integral over wave vectors restricted to the Fermi surface, reflecting the fact that nonequilibrium transport involves states near the Fermi surface. The reduction of the integration in this manner leads to the linearized Boltzmann equation. On the other hand, the equilibrium spin densities and currents, as shown in Figure 4.3, involve contributions from all occupied states, not just those near the Fermi surface.

For a given energy, the eigenfunctions for a conduction electron with wave-vector $\mathbf{k}$ take the form $\Psi_{\pm}(\mathbf{r},\mathbf{k}) = \psi_{\pm}(x,k_x)e^{ik_y y + ik_z z}$ where the spinor $\psi_{\pm}(x,k_x)$ satisfies

$$\left[-\frac{d^2}{dx^2} - k_B^2 \begin{pmatrix} \cos\theta & e^{-i\phi}\sin\theta \\ e^{i\phi}\sin\theta & -\cos\theta \end{pmatrix}\right]\psi_{\pm} = \kappa_{\pm}^2\psi_{\pm}. \tag{4.13}$$

In this expression,

$$\kappa_{\pm}^2 = k_x^2 \mp k_B^2, \tag{4.14}$$

and $\pm$ refers to majority/minority band electrons. The single-electron spin density and spin current density are [8]

$$\mathbf{s}_{\pm}(x,k_x) = \frac{\hbar}{2}\sum_{\alpha,\beta}\psi_{\pm,\alpha}^*(x,k_x)\boldsymbol{\sigma}_{\alpha,\beta}\psi_{\pm,\beta}(x,k_x) \tag{4.15}$$

and

$$\mathbf{Q}_{\pm}(x,k_x) = -\frac{\hbar^2}{2m}\sum_{\alpha,\beta}\mathrm{Im}[\psi_{\pm,\alpha}^*(x,k_x)\boldsymbol{\sigma}_{\alpha,\beta}\frac{d}{dx}\psi_{\pm,\beta}(x,k_x)]. \tag{4.16}$$

As a check, we used this formalism to calculate the equilibrium (zero applied current) spin density $\mathbf{s}_{\mathrm{eq}}(x)$ and equilibrium spin current density $\mathbf{Q}_{\mathrm{eq}}(x)$ for a magnetization distribution chosen arbitrarily except for the constraint that $|\mathbf{M}(x)|$ be uniform. The densities $\mathbf{s}_{\mathrm{eq}}(x)$ and $\mathbf{Q}_{\mathrm{eq}}(x)$ are obtained by retaining only the second term in square brackets in Eq. (4.9). The lines in Figure 4.3(a) are the Cartesian components of the imposed $\mathbf{M}(x)$. The solid dots in Figure 4.3(a) show that the spin density $\mathbf{s}_{\mathrm{eq}}(x)$ is parallel to $\mathbf{M}(x)$, as expected. Similarly, the electron-mediated spin-transfer torque should equal the phenomenological exchange torque density discussed by Brown [105]. This is confirmed by Figure 4.3(b), which shows that $\mathbf{N}_{\mathrm{eq}}(x)$ is proportional to $\mathbf{M}\times\mathbf{M}''(x)$ for the $\mathbf{M}(x)$ shown in Figure 4.3(a).

4.1.2 Semi-classical

A semi-classical approach to calculating the spin current density is useful for building physical intuition. Accordingly, we write an equation of motion for the spin density of every electron that contributes to the current. This idea has been used in the past, both semi-quantitatively [90] and qualitatively [91]. Our derivation is based on the behavior of

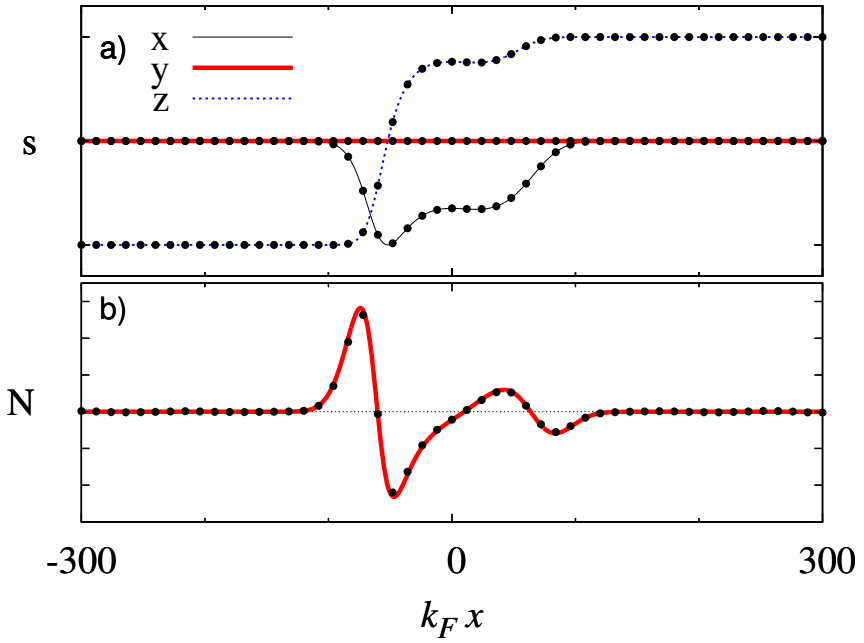

Figure 4.3: Equilibrium (zero-current) results: (a) Cartesian components of an arbitrarily chosen magnetization $\mathbf{M}(x)$ (lines); Cartesian components of the calculated spin density $\mathbf{s}_{\rm eq}(x)$ (solid dots); (b) Exchange torque (solid line) and calculated spin-transfer torque (solid dots).

an electron with energy E that moves along the x-axis through a uniform magnetic field $\mathbf{B}_{\rm ex} = B_{\rm ex}\hat{\mathbf{z}}$. The wave function for such an electron is

$$\varphi(x,E) = \begin{pmatrix} a\ e^{ik_+x} \\ b\ e^{ik_-x} \end{pmatrix}, \tag{4.17}$$

where

$$k_\pm^2 = 2mE/\hbar^2 \pm k_B^2. \tag{4.18}$$

We compute the spin density $\mathbf{s}(x,E)$ and the spin current density $\mathbf{Q}(x,E)$ for this electron using the right sides of Eq. (4.15) and Eq. (4.16), respectively, with $\psi_\pm \to \varphi$.

It is straightforward to check that the components of these densities transverse to the magnetic field satisfy the semi-classical relations

$$Q_x = s_x\langle v\rangle \qquad \text{and} \qquad Q_y = s_y\langle v\rangle, \tag{4.19}$$

where $\langle v\rangle$ is the velocity

$$\langle v\rangle = \frac{\hbar}{m}\frac{k_+ + k_-}{2} = \frac{\hbar}{m}\langle k\rangle. \tag{4.20}$$

Moreover, the transverse components of the spin density satisfy

$$\langle v \rangle \frac{ds_x}{dx} = -\frac{\hbar k_B^2}{m} s_y, \tag{4.21a}$$

$$\langle v \rangle \frac{ds_y}{dx} = -\frac{\hbar k_B^2}{m} s_x. \tag{4.21b}$$

These equations are the components of the vector equation

$$\frac{d\mathbf{s}}{dx} = -\frac{k_B^2}{\langle k \rangle} \mathbf{s} \times \hat{\mathbf{B}}_{\text{ex}} \tag{4.22}$$

where $\hat{\mathbf{B}}_{\text{ex}} = \hat{\mathbf{z}}$.

We now make the *ansatz* that all three Cartesian components of the semi-classical majority and minority spin densities $\mathbf{s}_\pm(x, k_x)$ satisfy Eq. (4.22) when the direction of the magnetic field varies in space. Specifically, if $\mathbf{B}_{\text{ex}}(x) = B_{\text{ex}} \hat{\mathbf{B}}_{\text{ex}}(x)$, we suppose that

$$\frac{d\mathbf{s}_\pm(x, k_x)}{dx} = -\frac{k_B^2}{\langle k \rangle} \mathbf{s}_\pm(x, k_x) \times \hat{\mathbf{B}}_{\text{ex}}(x), \tag{4.23}$$

where k_+ and k_- for $\mathbf{s}_+(x, k_x)$ are defined by Eq. (4.18) with $E = \hbar^2(k_x^2 - k_{\text{B}}^2)/2m$. [5] Similarly, k_+ and k_- for $\mathbf{s}_-(x, k_x)$ are defined by Eq. (4.18) with $E = \hbar^2(k_x^2 + k_{\text{B}}^2)/2m$. With suitable boundary conditions, we solve the differential equation Eq. (4.23) to determine the semi-classical, one-electron spin densities. The total, spin-resolved, spin densities follow by inserting these one-electron quantities into

$$\mathbf{s}_\pm(x) = \int \left[f_\pm(\mathbf{k} - \frac{eE\tau}{\hbar}\hat{\boldsymbol{x}}) - f_\pm(\mathbf{k}) \right] \mathbf{s}_\pm(x, k_x) \frac{k_x}{\langle k \rangle} d^3\mathbf{k}. \tag{4.24}$$

This equation differs from Eq. (4.9) by the weighting factor $k_x/\langle k \rangle$. [6] This factor guarantees that the flux carried by each electron is proportional to its velocity (see Appendix B). This is confirmed by Figure 4.4(b) which shows quantitative agreement between a fully quantum calculation of $\mathbf{s}(x)$ using Eq. (4.13), Eq. (4.15) and Eq. (4.9) and a semi-classical calculation using Eq. (4.23) and Eq. (4.24).

In light of the foregoing, it is reasonable to calculate the semi-classical single-electron spin current density from

$$\mathbf{Q}_\pm(x, k_x) = \mathbf{s}_\pm(x, k_x) \frac{\hbar k_x}{m} \tag{4.25}$$

[5] For $k_x^2 < 2k_B^2$, otherwise $k_- = 0 \Rightarrow \langle k \rangle = k_+/2$, which ensures that $\langle k \rangle$ is a continuous function of k_x.
[6] We note that k_x and $\langle k \rangle$ have the same algebraic sign.

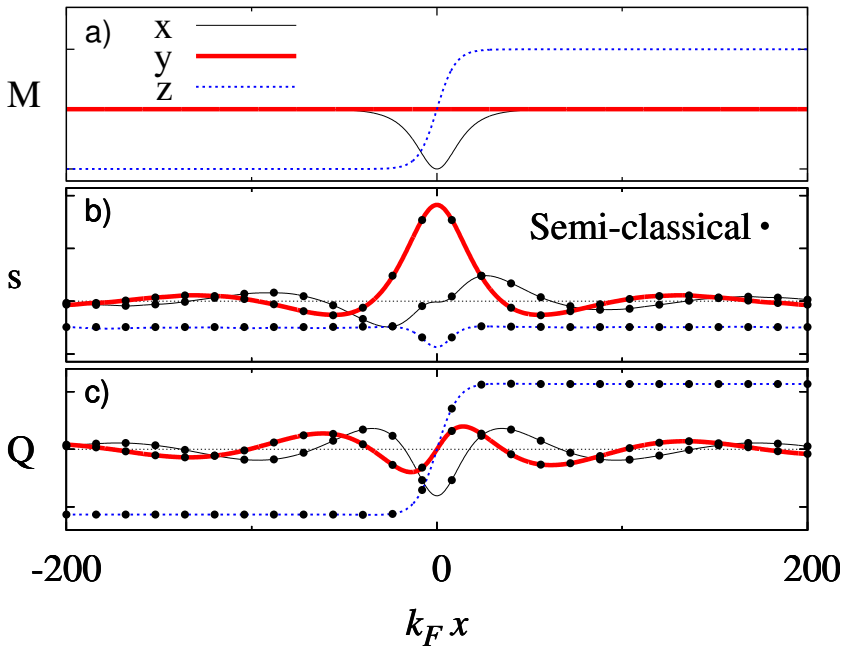

Figure 4.4: (a) Cartesian components of an imposed magnetization $\mathbf{M}(x)$ used in the other panels; (b) comparison of quantum (lines) to semi-classical (solid dots) calculations for the Cartesian components of the spin density $\mathbf{s}(x)$; (c) same comparison for the Cartesian components of the spin current density $\mathbf{Q}(x)$.

and use the second equation in Eq. (4.9) to find $\mathbf{Q}_{\pm}(x)$. The correctness of this prescription is illustrated in Figure 4.4(c).

4.2 Spin Spiral

As a preliminary to our discussion of domain walls, it is instructive to discuss the spin density and spin current density for a spin spiral. Here, we focus on a spiral with uniform pitch p where the magnetization rotates in the x-z plane, i.e., in Eq. (4.1),

$$\theta(x) = p\ x \qquad \text{and} \qquad \phi(x) = 0. \tag{4.26}$$

A cartoon version of this $\mathbf{M}(x)$ is shown in Figure 4.2. This figure also defines a *local* coordinate system that will be useful in what follows. The system (x', y', z') rotates as a function of x so the magnetization $\mathbf{M}(x)$ always points along $+z'$.

Calvo [106] solved Eq. (4.13) to find the eigenstates and eigen-energies of this spin spiral. In our notation,

$$\varepsilon_{\pm}(\mathbf{k}) = \frac{\hbar^2}{2m}\left(k^2 + \frac{1}{4}p^2 \pm \sqrt{(k_x p)^2 + k_B^4}\right), \tag{4.27}$$

and

$$\psi_{\pm}(\mathbf{k},\mathbf{r}) = e^{i\mathbf{k}\cdot\mathbf{r}} e^{-i\sigma_y\theta/2} e^{-i\sigma_x\alpha/2} \eta_{\pm}, \tag{4.28}$$

where

$$\sin\alpha = \frac{k_x p}{\sqrt{(k_x p)^2 + k_B^4}}, \tag{4.29}$$

and

$$\eta_{+} = \begin{pmatrix} 1 \\ 0 \end{pmatrix}, \qquad \eta_{-} = \begin{pmatrix} 0 \\ 1 \end{pmatrix}. \tag{4.30}$$

From these results, it is easy to compute the single-electron spin densities defined in Eq. (4.15). In the local (x', y', z') frame,

$$\mathbf{s}'_{\pm}(x, k_x) = \pm(0, \sin\alpha, \cos\alpha). \tag{4.31}$$

The corresponding calculation of the single-electron spin current densities Eq. (4.25) is straightforward but tedious and not very illuminating. Therefore, we pass directly to the total spin current density calculated by summing over all electrons as indicated in the second line of Eq. (4.9). Again in the local (x', y', z') frame,

$$\mathbf{Q}'(x) = A(p, k_{\mathrm{B}})(0, 0, 1). \tag{4.32}$$

where $A(p, k_{\mathrm{B}})$ is a constant. This shows that $\mathbf{Q}(x) \propto \mathbf{M}(x)$, *i.e.*, the spin current density for a free electron spin spiral is perfectly adiabatic. Wessely *et al.* [107] found consistent results in their density functional calculation of the steady-state spin current density associated with the helical spin density wave in erbium metal. We emphasize that Eq. (4.32) is independent of pitch for an infinite spin spiral. As we discuss below, a similar independence does *not* hold for domain walls. In that case, wide walls are adiabatic, but narrow ones are not.

The semi-classical formula Eq. (4.25) provides an appealing way to understand the adiabaticity of the spin current density in the spin spiral defined by Eq. (4.26). The key point is that the angle α in Eq. (4.29) which fixes the direction of $\mathbf{s}_{\pm}(x, k_x)$ in Eq. (4.31) is positive when k_x is positive and negative when k_x is negative (Figure 4.5). Moreover, for every k_x electron that contributes to the shifted Fermi surface sums in Eq. (4.9), there

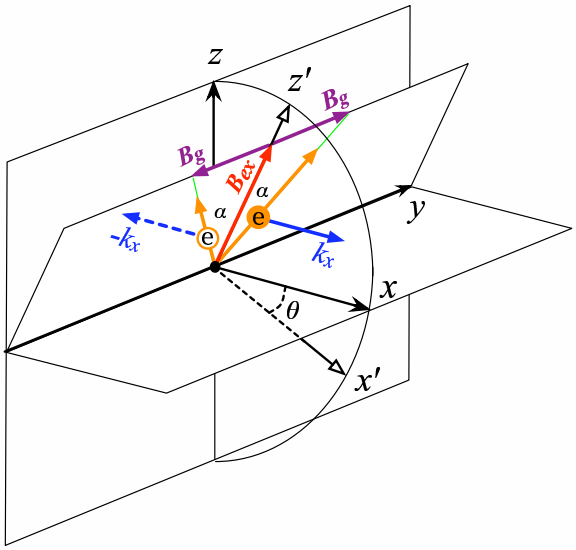

Figure 4.5: Electrons (wave vector k_x) and holes (wave vector $-k_x$) move in an effective field that is the sum of the exchange field $\mathbf{B}_{\rm ex}(x) \parallel \hat{\mathbf{z}}'$ and a fictitious, velocity-dependent "gradient" field induced by the spatial dependence of the exchange field. The spins align to the total effective field in an infinite spin spiral. The x axis lies in x'-z' plane.

is a contribution from a $-k_x$ hole. Now, a hole has opposite spin density to an electron and the spin current density Eq. (4.25) contains an additional factor of k_x. Therefore, the two spin density vectors in Figure 4.5 *subtract* to give a net spin density along $\hat{\mathbf{y}}$ while the corresponding two spin current density vectors *add* to give a net spin current density along $\hat{\mathbf{z}}'$. This occurs for all k_x in the sums so $\mathbf{Q}(x)$ aligns exactly with the local exchange field and thus with the local magnetization.

The opposite situation occurs for fully occupied states below the Fermi energy. The spins of the forward and backward moving electrons combine to produce a net moment aligned with the exchange field, as necessary for self-consistency. Further, the spin currents, with the additional factor of k_x add to give a net spin current along $\hat{\mathbf{y}}$, so that its gradient gives the correct form of the phenomenological exchange torque density.

To summarize: an electric current that passes through a spin spiral generates a spin accumulation with a component transverse to the magnetization. The spin current density possesses *no* such component due to pairwise cancellation between forward and backward moving spins of the same type (majority or minority). Moreover, since the cancellation occurs within each band, the final result is insensitive to the details of intraband scattering.

It remains only to understand the origin of the misalignment angle α. Why does each spin not simply align itself with $\mathbf{B}_{\rm ex}$? Berger [90] was the first to notice this fact and the physics was made particularly clear by Aharonov and Stern [108]. These authors studied the adiabatic approximation for a classical magnetic moment that moves in a slowly varying field $\mathbf{B}(x)$. Not obviously, the moment behaves as if were subjected to a effective magnetic field $\mathbf{B}_{\rm eff}(x)$ that is the sum of $\mathbf{B}_{\rm ex}(x)$ and a fictitious, velocity-dependent, "gradient" field $\mathbf{B}_{\rm g}(x)$ that points in the direction $\nabla\hat{\mathbf{B}}(x)\times\hat{\mathbf{B}}(x)$. For our problem,

$$\mathbf{B}_{\rm eff}=\mathbf{B}_{\rm ex}+\frac{\hbar^2 k_x}{2m\mu}\frac{d\hat{\mathbf{B}}_{\rm ex}}{dx}\times\hat{\mathbf{B}}_{\rm ex}. \tag{4.33}$$

The presence of this gradient field is apparent from Eq. (4.27) where the square root is proportional to $|\mathbf{B}_{\rm eff}|$. *The adiabatic solution corresponds to perfect alignment of the moment with* $\mathbf{B}_{\rm eff}(x)$. This alignment is indicated in Eq. (4.31) and in Figure 4.5. More generally, the expected motion of the magnetic moment is precession around $\mathbf{B}_{\rm eff}(x)$.Nevertheless, as indicated above, the total spin current density for the spin spiral aligns with $\mathbf{B}_{\rm ex}(x)$ (which is the conventional definition of adiabaticity for this quantity) when the net effect of all conduction electrons is taken into account.

The existence of the gradient field $\mathbf{B}_{\rm g}$ can be shown classically in a simple model. Imagine there is a magnetization $\mathbf{M}$ moving in a non-uniform magnetic field $\mathbf{H}(x)$. Equivalently, the variation of $\mathbf{H}$ that $\mathbf{M}$ feels due to the motion can be modeled as a time dependent magnetic field $\mathbf{H}(t)$. We assume the field rotates about the $\hat{\mathbf{y}}$ axis with constant speed: $\mathbf{H}(t)=H(\cos\omega t\,\hat{\mathbf{z}}-\sin\omega t\,\hat{\mathbf{x}})$ (Figure 4.6). We now look for a steady state solution for $\mathbf{M}$, *i.e.* a state where the relative orientation between $\mathbf{H}$ and $\mathbf{M}$ doesn't change over time. The dynamics of the magnetization $\mathbf{M}$ is governed by

$$\frac{d\mathbf{M}}{dt}=-\gamma\mathbf{M}\times\mathbf{H}(t). \tag{4.34}$$

In Figure 4.6, $\hat{\mathbf{x}},\hat{\mathbf{y}}$ and $\hat{\mathbf{z}}$ are the axes for a fixed frame, and $\hat{\mathbf{X}},\hat{\mathbf{Y}}$ and $\hat{\mathbf{Z}}$ are axes for a rotating frame where $\mathbf{H}$ always aligns to $\hat{\mathbf{Z}}$. We write $\mathbf{M}$ and $\mathbf{H}$ in the rotating frame,

$$\mathbf{M}=M_X\hat{\mathbf{X}}+M_Y\hat{\mathbf{Y}}+M_Z\hat{\mathbf{Z}}\qquad\text{and}\qquad\mathbf{H}=H\hat{\mathbf{Z}}. \tag{4.35}$$

In the steady state, $\mathbf{M}$ doesn't change its orientation in the rotating frame. This means

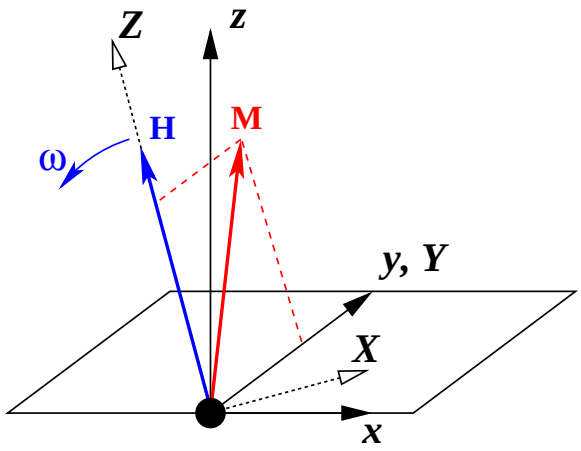

Figure 4.6: Magnetization in rotating magnetic field

that M_X, M_Y and M_Z are all constants in the rotating frame, so $\dot{M}_X = \dot{M}_Y = \dot{M}_Z = 0$. Therefore, in the rotating frame Eq. (4.34) is ($\dot{\hat{\mathbf{Y}}} = 0$)

$$M_X \dot{\hat{\mathbf{X}}} + M_Z \dot{\hat{\mathbf{Z}}} = -\gamma H (M_Y \hat{\mathbf{X}} - M_X \hat{\mathbf{Y}}). \tag{4.36}$$

Since $\dot{\hat{\mathbf{X}}} = \omega \hat{\mathbf{Z}}$ and $\dot{\hat{\mathbf{Z}}} = -\omega \hat{\mathbf{X}}$, Eq. (4.36) becomes

$$(M_Z \omega - \gamma H M_Y)\hat{\mathbf{X}} - \gamma H M_X \hat{\mathbf{Y}} + M_X \omega \hat{\mathbf{Z}} = 0. \tag{4.37}$$

This implies that $M_X = 0$ and $M_Y / M_Z = \omega / \gamma H$. Thus, $\mathbf{M}$ aligns to an effective field

$$\mathbf{H}_{\text{eff}} = H\hat{\mathbf{Z}} + \frac{\omega}{\gamma}\hat{\mathbf{Y}} = \mathbf{H} + \frac{1}{\gamma}\frac{d\hat{\mathbf{H}}}{dt} \times \hat{\mathbf{H}}, \tag{4.38}$$

which is exactly same as Eq. (4.33) if we replace the spacial derivative by the time derivative $d/dt = (\hbar k_x / m) d/dx$ and make appropriate unit conversion.

Eq. (4.38) tells us that no matter how slowly the magnetic field changes, the magnetization does not align to the magnetic field unless the field does not change in time or is uniform in space.

4.3 Domain Walls

Our main interest is the spin-transfer torque associated with domain walls that connect two regions of uniform and antiparallel magnetization. A realistic wall of this kind can be described by Eq. (4.1) with [109]

$$\theta(x) = \frac{\pi}{2} - \arcsin\left[\tanh\left(\frac{x}{w}\right)\right], \tag{4.39}$$

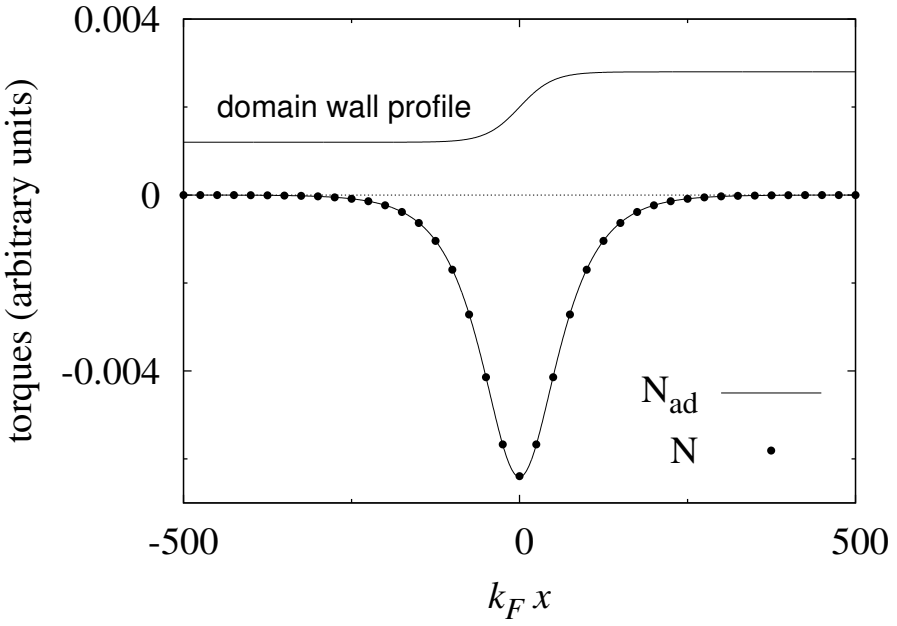

Figure 4.7: Distributed spin-transfer torque for a long Nèel domain wall with $w = 50$ and $L = 6.25$ ($k_F = 1$ and $k_B = 0.4$): semi-classical calculation of $\mathbf{N}_{\rm st}$ (solid dots) compared to Eq. (4.41) for $\mathbf{N}_{\rm ad}(x)$ (solid curve).

The wall is Néel-type if $\phi(x) = 0$ and Bloch-type if $\phi(x) = \pi/2$. We will speak of the domain wall width w as "long" or "short" depending on whether w is large or small compared to the characteristic length

$$L = \frac{E_F}{E_{\rm ex}} \frac{1}{k_F} = \frac{k_F}{k_B^2}. \tag{4.40}$$

Intuitively, the adiabatic approximation should be valid when $w \gg L$. When applied to Eq. (4.9), the predicted adiabatic spin-transfer torque for our model is

$$\mathbf{N}_{\rm ad}(x) = -\frac{\hbar}{2}\eta \frac{neE\tau}{m} \partial_x \hat{\mathbf{M}}(x), \tag{4.41}$$

where n is the electron density, and η is the polarization of the current. The calculations required to check this for long domain walls are difficult quantum mechanically (for numerical reasons) but straightforward semi-classically. At the single-electron level, adiabaticity again corresponds to alignment of the spin moment with the effective field defined in Eq. (4.33). The results for a typical long wall (Figure 4.7) demonstrate that summation over all electrons produces alignment of $\mathbf{Q}(x)$ with $\mathbf{M}(x)$ so the adiabatic formula Eq. (4.41) is indeed correct in this limit.

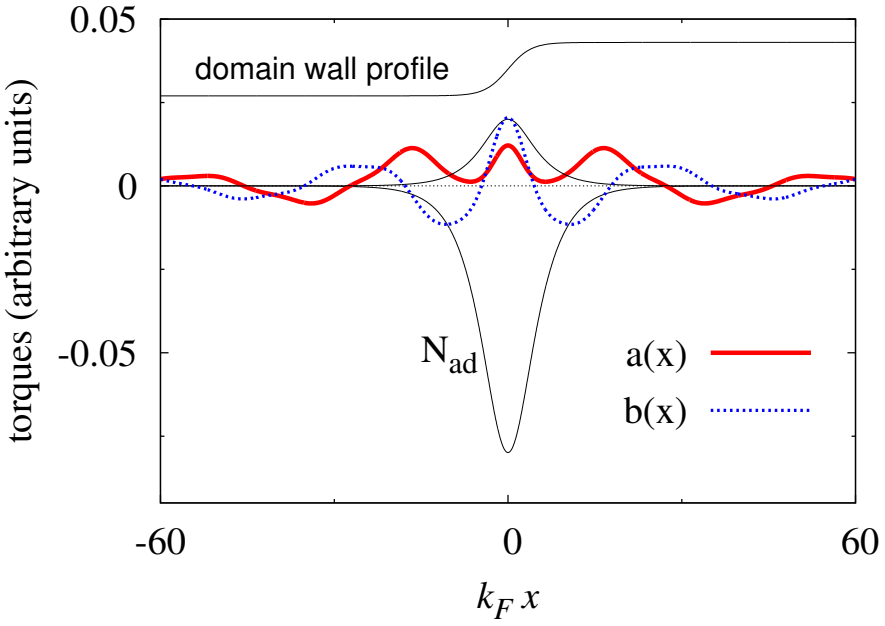

Figure 4.8: Distributed spin-transfer torque for a short Nèel domain wall with $w = 4$ and $L = 6.25$ ($k_F = 1$ and $k_B = 0.4$): in-plane piece $a(x)$ (heavy solid curve); out-of-plane piece $b(x)$ (dashed curve); adiabatic prediction (light solid curve); second term in Eq. (4.5) scaled to match the maximum of $b(x)$ (light solid curve).

For short walls, we have carried out calculations of $\mathbf{N}_{\rm st}(x)$ both quantum mechanically and semi-classically. The two methods agree very well with one another (see Figure 4.4) but not with the proposed form Eq. (4.5). Bearing in mind that, when the magnetization changes, $\hat{\mathbf{x}}'$ points along $\partial_x \mathbf{M}$ and $\hat{\mathbf{y}}$ points along $\mathbf{M} \times \partial_x \mathbf{M}$, our result for the spin-transfer torque is

$$\mathbf{N}_{\rm st}(x) = \mathbf{N}_{\rm ad}(x) + a(x)\hat{\mathbf{x}}' + b(x)\hat{\mathbf{y}}. \tag{4.42}$$

$\mathbf{N}_{\rm st}(x)$ differs from $\mathbf{N}_{\rm ad}(x)$ because gradients in the gradient field induce single electron spin moments to precess around $\mathbf{B}_{\rm eff}(x)$ rather to align perfectly with it. Figure 4.8 shows $a(x)$ and $b(x)$ as calculated for a typical short domain wall. The associated torques lie in the plane of the magnetization and perpendicular to that plane, respectively. These non-adiabatic contributions to the torque are both oscillatory functions of position that do not go immediately to zero when the the magnetization becomes uniform. In other words, $a(x)$ and $b(x)$ are generically non-local functions of the magnetization $\mathbf{M}(x)$. The positive-valued function that falls to zero at the edges of the domain wall (light solid curve in Figure 4.8) is

the second function in Eq. (4.5) with c_2 chosen to match $b(x)$ at their common maximum. Evidently, the proposed torque function Eq. (4.5) gives at best a qualitative account of the out-of-plane non-adiabatic torque.

A convenient measure of the degree of non-adiabaticity of the spin-transfer torque is

$$\mathcal{Q} = \frac{\max|b(x)|}{\max|N_{\rm ad}(x)|}. \tag{4.43}$$

Left panel of Figure 4.9 plots this quantity as a function of scaled domain wall width w/L on a log scale. The observed exponential decrease of the non-adiabatic torque as the wall width increases can be understood from the work of Dugaev *et al.* [110] These authors treat the gradient field in Eq. (4.33) as a perturbation and calculate the probability for an electron in a $(k_x \uparrow)$ state to scatter into a $(k'_x \downarrow)$ state in the Born approximation. If we choose k_x and k'_x as k_F^+ and k_F^-, respectively, their results imply that the probability $\mathcal{P}$ that a majority electron retains its spin and becomes a minority electron as it passes through a domain wall is

$$\mathcal{P} \propto \exp(-\gamma w/L), \tag{4.44}$$

where γ is a constant of order unity. This rationalizes the result plotted in the left panel of Figure 4.9 because the magnitude of the minority spin component determines the amplitude of the spin precession around $\mathbf{B}_{\rm eff}(x)$ and thus the magnitude of the non-adiabatic component of $\mathbf{s}$ and $\mathbf{Q}$ in Eq. (4.25). In fact, $N_{\rm ad} \propto 1/w$, so it is the case that

$$\max|b(x)| \propto \frac{1}{w}\exp(-\gamma w/L). \tag{4.45}$$

The slope of the straight line in the left panel of Figure 4.9, *i.e.*, the value of the constant γ in Eq. (4.44) depends on the sharpness of the domain wall. Using Eq. (4.39) and other simple domain wall profile functions, it is not difficult to convince oneself that a suitable measure of domain wall sharpness is the maximum value of the second derivative $\theta''(x)$ for walls with the same width. The numerical results shown in the right panel of Figure 4.9 confirm this to be true. The sharper the domain wall, the less rapidly the non-adiabatic torque disappears with increasing domain wall width.

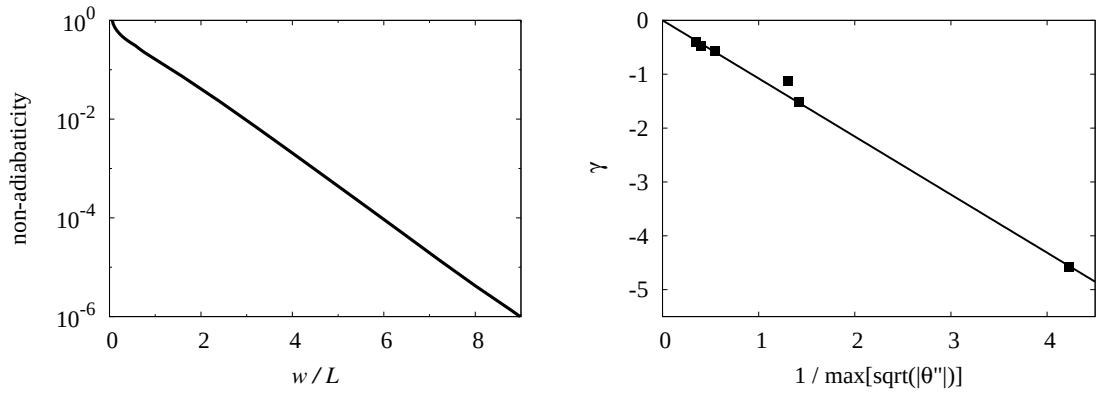

Figure 4.9: Left: Non-adiabaticity in Eq. (4.43) versus wall width scaled by the characteristic length in Eq. (2.21). Right: Dependence of γ in Eq. (4.44) on domain wall sharpness. Squares are calculated points. Straight line is a guide to the eye that passes through the origin.

4.4 Relation to Other Work

4.4.1 Waintal & Viret

Waintal and Viret [91] (WV) used a free-electron Stoner model and the Landauer-Büttiker formalism to calculate the spin transfer torque associated with a Néel wall with magnetization Eq. (4.1) and

$$\theta(x) = \begin{cases} 0, & x < -w \\ (\pi/2)\,(x/w+1)\,, & -w \le x \le w \\ \pi, & x > w. \end{cases} \tag{4.46}$$

For this wall profile (which is exactly one half-turn of a uniform spin spiral in the interval $-w \le x \le w$), WV reported oscillatory non-adiabatic contributions to the torque similar to our functions $a(x)$ and $b(x)$. This contrasts with the perfect adiabaticity we found in Sec. 4.2 for the infinite spin spiral. Moreover, the amplitude of the non-adiabatic torque reported by WV for this wall decreases only as $1/w$ rather than $(1/w)\exp(-\gamma w/L)$ as we found above.

The disparities between Ref. [91] and the present work all arise from the unphysical nature of the domain wall Eq. (4.46). Specifically, the divergence of $\theta''(x)$ at $x = \pm w$ locates this wall at the origin of right panel of Figure 4.9 where $\gamma = 0$. This brings their result into agreement with Eq. (4.45). Any rounding of the discontinuity in slope at $x = \pm w$

would yield a finite value for $\theta''(x)$ and thus a non-zero value of γ.

In Appendix C, we calculate the spin-transfer torque for the wall Eq. (4.46) using our methods. Qualitatively, the pure $1/w$ behavior of the non-adiabatic torque comes from the fact that there is a sudden jump in $\theta'(x)$ at $x = \pm w$. There is a corresponding jump in the direction of $\mathbf{B}_{\text{eff}}(x)$ as defined by Eq. (4.33). Spins propagating along the the x-axis cannot follow this abrupt jump and thus precess around the post-jump field direction with an amplitude determined by the sine of the angle between the before-and-after field directions. The latter is proportional to the jump in $\theta'(x)$, which is $\pi/2w$ for the wall Eq. (4.46).

4.4.2 Zhang & Li

In spin spirals and long domain walls, we find that the non-equilibrium spin current is adiabatic, *i.e.*, $\mathbf{Q}(x)$ is aligned with $\mathbf{M}(x)$ [or $\mathbf{B}_{\text{ex}}(x)$]. At the same time, we find in both cases that the non-equilibrium spin density $\mathbf{s}(x)$ is *not* aligned with the magnetization; there is component of $\mathbf{s}(x)$ transverse to $\mathbf{M}(x)$. The corresponding transverse component of the spin current density cancels between pairs of electrons moving in opposite directions. Zhang and Li [92] found exactly the same form of non-equilibrium spin accumulation (called $\delta\mathbf{m}(x)$ by them) using a phenomenological theory. They proposed that this non-equilibrium spin density relaxes by spin-flip scattering toward alignment with the magnetization. Such a relaxation would produce a non-adiabatic torque of the form given by the second term in Eq. (4.5). The correctness of this predicted non-adiabatic torque depends on the correctness of the assumed model for relaxation of transverse spin accumulation through spin flip scattering.

Zhang and Li assume a form for the rate of spin flip scattering, $\delta\mathbf{m}/\tau_{\text{sf}}$, that has been used successfully as a phenomenological description of *longitudinal* spin relaxation in systems with collinear magnetization. While it is plausible to extend this form, as they do, to describe *transverse* spin relaxation in non-collinear systems, our calculations indicate that it is not likely to be correct. Our reasoning is simplest to appreciate for a spin spiral with small pitch p. In this limit, Eqs. Eq. (4.29) and Eq. (4.31) show that the transverse component of the spin for every electron eigenstate is proportional to its velocity. This

means that the majority band electrons contribute a transverse spin accumulation and an electric current that are proportional to one other. The same is true, separately, for the minority band electrons. This conclusion is independent of the details of the electron distribution. Therefore, for a fixed total current, it is impossible to relax the transverse spin accumulation without changing the longitudinal polarization of the current. No such change occurs in the model in Ref. [92], casting doubt on the validity of the form of the spin flip scattering assumed there.

Microscopic considerations also argue against this form of the relaxation. As we have emphasized, the natural basis for an electron spin moving though a non-collinear magnetization is not along the local exchange field $\mathbf{B}_{\text{ex}}(x)$, but rather along a local effective field $\mathbf{B}_{\text{eff}}(x)$, which includes the corrections due to the gradient of the magnetization [see Eq. (4.33)]. Any spin that deviates from parallel or antiparallel alignment with the effective field will precess around the effective field, and on average will point parallel or antiparallel. Thus, we expect that there is *no* tendency for electron spins moving in a non-uniform magnetization to align themselves with the local exchange field $\mathbf{B}_{\text{ex}}(x)$ by spin-flip scattering (or any other mechanism). Rather, the adiabatic solution is precisely alignment of their spins with the local effective field $\mathbf{B}_{\text{eff}}(x)$. Without further microscopic justification, we believe that the phenomenological form of spin flip scattering assumed in Ref. [92] should not be used in systems with non-collinear magnetizations. Hence, this analysis argues against the existence of the resulting contribution to the "non-adiabatic" torque from spin flip scattering.

4.5 Scattering

We do not explicitly treat scattering in any of our calculations. However, the distribution function in Eq. (4.9), a shifted Fermi distribution, is an approximate solution of the Boltzmann equation in certain limits. First, the electric field must be small enough that the transport is in the linear regime. Then, the appropriate limits are determined by three important length scales, the Fermi wavelength, the mean free path, and the characteristic length of the structure, either the pitch of the spin spiral or the width of the domain wall.

In all cases, we consider the limit in which the Fermi wavelength is short compared to the mean free path. This limit allows the description of the states of the system in terms of the eigenstates of the system in the absence of scattering. Different limits apply to the cases of domain walls and of spin spirals because the distribution functions are interpreted differently for these two structures.

We use the Boltzmann equation in two different ways. When the mean free path is much longer than the characteristic size of the structure, the distribution function describes the occupancy of the eigenstates of the entire system. This distribution function is independent of the spatial coordinate and we refer to this approach as global. In the opposite limit, the distribution function is spatially varying and describes the occupancy of eigenstates of the local Hamiltonian, which includes the exchange field and the gradient field. We refer to this approach as local, as the distribution function can vary spatially.

For spin spirals, the distribution functions are shifted Fermi functions of the eigenenergies of the spin spiral. In the limit that the pitch of the spiral is much shorter than the mean free path, the shifted distribution given in Eq. (4.9) is a solution of the global Boltzmann equation in the relaxation time approximation. The distribution function also becomes a solution in the opposite limit, where the mean free path is much shorter than the pitch of the spiral. In this limit, the Boltzmann equation is considered locally rather than globally. At each point in space the states are subject to the local exchange field, and the local gradient field. The distribution function is defined for states that are locally eigenstates of the sum of the fields. The local distribution function is given by the adiabatic evolution in the rotating reference frames of the distribution function specified in Eq. (4.9). In the limit that the pitch of the spiral goes to infinity, this distribution function locally solves the Boltzmann equation in the relaxation time approximation. Thus, for spin spirals, the distribution function given in Eq. (4.9) is a solution in the limits that the mean free path is much greater than or much less than the pitch. We speculate that the corrections in between these limits are small.

Domain walls are not uniform in the way that spin spirals are, so the distribution functions need to be given a different interpretation. For these structures, the distribution

function is determined from the properties of the states in the leads. For example, in the Landauer-Büttiker approach to this problem,[91] scattering is ignored in the domain wall itself and confined to the "leads" adjacent to it (these leads are assumed to be "wide" and function as electron reservoirs). An applied voltage is assumed to raise the energy of electron states in one lead relative to the other. Thus, in a formula like Eq. (4.9), the distribution function is shifted in energy rather than in velocity.

We also do not treat scattering within the domain wall explicitly, but we assume that the wall is bounded by long leads that are as "narrow" as the domain wall region and have resistances per unit length that are comparable to that of the domain wall region. Thus, the distribution of the states approaching the domain wall region is similar to the distribution of states in an extended wire, *i.e.*, to that given by Eq. (4.9). For domain walls in long wires, the distribution function for left going states is determined by the right lead and for right going states by the left lead. With this interpretation, the distribution given in Eq. (4.9) is a solution in the limit that the scattering in the domain wall is weak, that is, the domain wall is much narrower than the mean free path.

The distribution in Eq. (4.9) is also a solution in the limit that the mean free path is much shorter than the domain wall width. Since the Fermi wave length is much shorter than the mean free path, it is much less than the domain wall width. In this case, quantum mechanical reflection is negligible and the quantum mechanical states are closely related to the semiclassical trajectories. With a similar interpretation of the distribution function as was made for the spin spirals in this limit, the same conclusion holds for the domain walls.

4.6 Summary & Conclusion

In this chapter, we analyzed spin-transfer torque in systems with continuously variable magnetization using previous results of Calvo [106] for the eigenstates of an infinite spin spiral and of Aharonov and Stern [108] for the classical motion of a magnetic moment in an inhomogeneous magnetic field. Adiabatic motion of individual spins corresponds to alignment of the spin moment *not* with the exchange field (magnetization) but with an effective field that is slightly tilted away form the exchange field by an amount that

depends on the spatial gradient of the magnetization. Nevertheless, when summed over all conduction electrons, the spin current density is parallel to the magnetization both for an infinite spin spiral and for domain walls that are long compared to a characteristic length L that depends on the exchange energy and the Fermi energy.

Non-adiabatic corrections to the spin-transfer torque occur only for domain walls with widths w that are comparable to or smaller than L. The non-adiabatic torque is oscillatory and non-local in space with an amplitude that decreases as $w^{-1}\exp(-\gamma w/L)$. The constant γ is largest for walls with the sharpest magnetization gradients. This suggests that non-adiabatic torques may be important for spin textures like vortices where the magnetization varies extremely rapidly.

Using microscopic considerations, we have also argued that the role of the gradient field to tilt spins away from the exchange field casts serious doubt on a recent proposal by Zhang and Li [92] that a non-negligible non-adiabatic contribution to the torque arises from relaxation of the non-equilibrium spin accumulation to the magnetization vector by spin flip scattering. We conclude that, if the second term in Eq. (4.5) truly accounts for the systematics of current-driven domain wall motion, the physics that generates this term still remains to be identified.

Finally, we have carefully discussed the role of scattering in this problem with particular emphasis on the approximation used here to neglect scattering within the domain wall itself but to treat the adjacent ferromagnetic matter as bulk-like. We argue that this approximation is valid in limits that either include or bracket the most interesting experimental situations and therefore is likely to be generally useful.

APPENDIX A

ENERGY EXPRESSION

The energy of the free layer includes a Zeeman energy E_Z from the external field H, a magnetostatic shape anisotropy energy E_s, and a surface anisotropy energy (parameterized by K_u) that vanishes in the limit that the free layer thickness $d \to \infty$.

The Zeeman energy is

$$E_Z = V\mu_0 M_\mathrm{s}\hat{\mathbf{m}} \cdot \mathbf{H}. \tag{A.1}$$

The shape anisotropy energy is

$$E_s = V\frac{1}{2}\mu_0 M_\mathrm{s}\hat{\mathbf{m}} \cdot \mathbf{H}_d = V\frac{1}{2}\mu_0 M_\mathrm{s}^2\hat{\mathbf{m}} \cdot \mathcal{N} \cdot \hat{\mathbf{m}}, \tag{A.2}$$

where $\mathbf{H}_d = M_\mathrm{s}\mathcal{N} \cdot \hat{\mathbf{m}}$ and $\mathcal{N}$ are the demagnetization field and demagnetization tensor, respectively. Referring to Figure 3.3, the total energy is

$$\begin{aligned} E = &\frac{1}{2}\mu_0 M_\mathrm{s}^2 V[L\cos^2\theta + M\sin^2\theta\sin^2\phi + N\sin^2\theta\cos^2\phi] \\ &- \mu_0 M_\mathrm{s} V H\cos\theta - \frac{2VK_u}{d}\sin^2\theta\cos^2\phi \end{aligned} \tag{A.3}$$

where L, M, N are the demagnetization factors for the $\hat{z}, \hat{y}, \hat{x}$ directions. These terms can be combined to give

$$\frac{2E}{\mu_0 M_\mathrm{s}^2 V} = -2h\cos\theta + h_L\cos^2\theta + h_M\sin^2\theta\sin^2\phi + h_N\sin^2\theta\cos^2\phi, \tag{A.4}$$

where $h = H/M_s$, and

$$h_L = L - \frac{H_k}{M_\mathrm{s}}, \qquad h_M = M, \qquad h_N = N - \frac{4K_u}{\mu_0 M_\mathrm{s}^2 d}. \tag{A.5}$$

If we model the thin free layer as a very flat ellipsoid with semi-axis $a \geq b \gg c$, Eqs. (2.23-25)

in Ref. [111] give

$$L = \frac{c}{a}(1-e^2)^{1/2}\frac{K-E}{e^2}, \tag{A.6a}$$

$$M = \frac{c}{a}\frac{E-(1-e^2)K}{e^2(1-e^2)^{1/2}}, \tag{A.6b}$$

$$N = 1 - \frac{cE}{a(1-e^2)^{1/2}}, \tag{A.6c}$$

where K and E are complete elliptic integrals with argument $e = \sqrt{1-b^2/a^2}$. For the nominal geometry of Ref. [32], we have $2a = 130\,\mathrm{nm}, 2b = 70\,\mathrm{nm}, 2c = 3\,\mathrm{nm}$, so $L \approx 0.017, M \approx 0.035, N \approx 0.948$.

APPENDIX B

SEMI-CLASSICAL WEIGHTING FACTOR

The weighting factor $k_x/\langle k\rangle$ used in Eq. (4.24) brings the amplitude of the dynamic (transverse) part of the semi-classical, one-electron spin density into accord with the corresponding quantum mechanical amplitude. This can be seen from a simple model problem that we solve both quantum mechanically and semi-classically. Namely, a spin initially oriented along the $+\hat{\mathbf{x}}$ direction propagates from $x = -\infty$ to $x = \infty$ through a magnetization that changes abruptly from $\mathbf{M}(x) = M(1,0,0)$ for $x < 0$ to $\mathbf{M}(x) = M(0,0,1)$ for $x \geq 0$. For $x < 0$, the eigenstates are

$$\psi_\uparrow^-(x) = \frac{1}{\sqrt{2}}\begin{pmatrix} 1 \\ 1 \end{pmatrix} e^{ik_\uparrow x}, \qquad \psi_\downarrow^-(x) = \frac{1}{\sqrt{2}}\begin{pmatrix} 1 \\ -1 \end{pmatrix} e^{ik_\downarrow x}, \tag{B.1}$$

and for $x > 0$, the eigenstates are

$$\psi_\uparrow^+(x) = \begin{pmatrix} 1 \\ 0 \end{pmatrix} e^{ik_\uparrow x}, \qquad \psi_\downarrow^+(x) = \begin{pmatrix} 0 \\ 1 \end{pmatrix} e^{ik_\downarrow x}. \tag{B.2}$$

If we choose the incoming state as

$$\psi(x) = \psi_\uparrow^-(x), \tag{B.3}$$

the reflection and transmission amplitudes for spin flip $(r_{\uparrow\downarrow}, t_{\uparrow\downarrow})$ and no spin flip $(r_{\uparrow\uparrow}, t_{\uparrow\uparrow})$ are determined by matching the total wave function and its derivative at $x = 0$:

$$\psi_\uparrow^- + r_{\uparrow\uparrow}(\psi_\uparrow^-)^* + r_{\uparrow\downarrow}(\psi_\downarrow^-)^* = t_{\uparrow\uparrow}\psi_\uparrow^+ + t_{\uparrow\downarrow}\psi_\downarrow^+, \tag{B.4a}$$

$$k_\uparrow\psi_\uparrow^- - r_{\uparrow\uparrow}k_\uparrow(\psi_\uparrow^-)^* - r_{\uparrow\downarrow}k_\downarrow(\psi_\downarrow^-)^* = t_{\uparrow\uparrow}k_\uparrow\psi_\uparrow^+ + t_{\uparrow\downarrow}k_\downarrow\psi_\downarrow^+. \tag{B.4b}$$

It is straightforward to confirm that these equations are solved by

$$r_{\uparrow\uparrow} = \frac{k_\uparrow^2 - k_\downarrow^2}{k_\uparrow^2 + 6k_\uparrow k_\downarrow + k_\downarrow^2}, \qquad r_{\uparrow\downarrow} = \frac{2k_\uparrow(k_\downarrow - k_\uparrow)}{k_\uparrow^2 + 6k_\uparrow k_\downarrow + k_\downarrow^2}, \tag{B.5a}$$

$$t_{\uparrow\uparrow} = \frac{4\sqrt{2}k_\uparrow k_\downarrow}{k_\uparrow^2 + 6k_\uparrow k_\downarrow + k_\downarrow^2}, \qquad t_{\uparrow\downarrow} = \frac{2\sqrt{2}k_\uparrow(k_\uparrow + k_\downarrow)}{k_\uparrow^2 + 6k_\uparrow k_\downarrow + k_\downarrow^2}. \tag{B.5b}$$

We are interested in the transmitted wave function,

$$\psi_{\rm tr}(x) = t_{\uparrow\uparrow}\psi^+_\uparrow(x) + t_{\uparrow\downarrow}\psi^+_\downarrow(x) = \begin{pmatrix} t_{\uparrow\uparrow}e^{ik_\uparrow x} \\ t_{\uparrow\downarrow}e^{ik_\downarrow x} \end{pmatrix}, \tag{B.6}$$

which carries a spin density,

$$\mathbf{s}^{\rm qm}_{\rm tr}(x) = \frac{\hbar}{2}\left[2t_{\uparrow\uparrow}t_{\uparrow\downarrow}\cos(\delta k x), 2t_{\uparrow\uparrow}t_{\uparrow\downarrow}\sin(\delta k x), (t^2_{\uparrow\uparrow} - t^2_{\uparrow\downarrow})\right], \tag{B.7}$$

where $\delta k = k_\uparrow - k_\downarrow$. Notice that the oscillation is transverse to the $x \to \infty$ magnetization and of amplitude $\hbar t_{\uparrow\uparrow}t_{\uparrow\downarrow}$.

If we analyze the same problem semi-classically, a majority electron propagates freely until it reaches $x = 0$. At that point, the electron feels a magnetization perpendicular to its magnetic moment and begins precession around that magnetization with unit amplitude. The associated spin density is

$$\mathbf{s}^{\rm sc}_{\rm tr}(x) = \frac{\hbar}{2}\left[\cos(\delta k x), \sin(\delta k x), 0\right]. \tag{B.8}$$

Comparing Eq. (B.7) to Eq. (B.8) shows that the transverse oscillation amplitudes will be equal if we multiply the semi-classical result by the weighting factor

$$2t_{\uparrow\uparrow}t_{\uparrow\downarrow} = \frac{32k^2_\uparrow k_\downarrow(k_\uparrow + k_\downarrow)}{(k^2_\uparrow + 6k_\uparrow k_\downarrow + k^2_\downarrow)^2} \approx \frac{2k_\uparrow}{k_\uparrow + k_\downarrow} = \frac{k_x}{\langle k\rangle}. \tag{B.9}$$

Figure B.1 illustrates the quality of the approximation in Eq. (B.9) if we identify $k_\uparrow$ and $k_\downarrow$ with k^+_F and k^-_F (respectively) in Eq. (4.8). Of course, k_x plays the role of $k_\uparrow$ in Eq. (4.24).

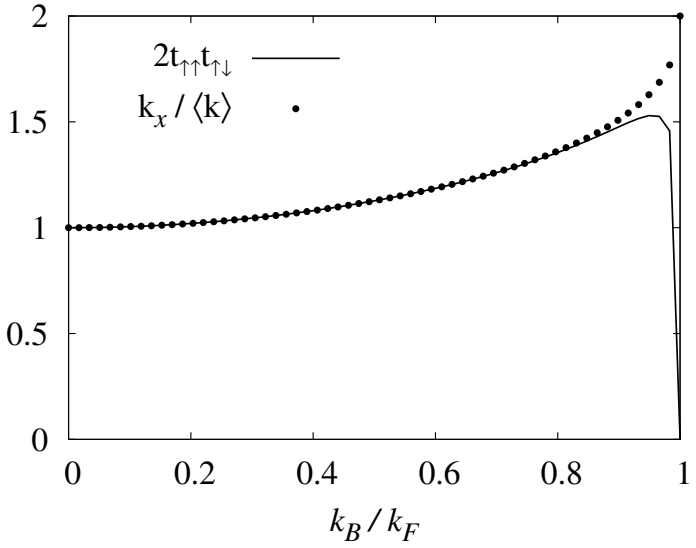

Figure B.1: The semi-classical weighting factor for the spin density. Solid (dotted) curve is the expression on the left (right) side of the $\approx$ symbol in Eq. (B.9).

APPENDIX C

SPIN SPIRAL DOMAIN WALL

The semi-classical spin density associated with electron propagation through a magnetization like Eq. (4.1) is the solution of Eq. (4.23) with suitable boundary conditions. Choosing $\phi = 0$, we simplify the notation by using the prefactor $\lambda = k_B^2/\langle k \rangle$ and an overdot for d/dx to write the components of Eq. (4.23) as

$$\dot{s}_x = -\lambda s_y \cos\theta \tag{C.1a}$$

$$\dot{s}_y = -\lambda s_z \sin\theta + \lambda s_x \cos\theta \tag{C.1b}$$

$$\dot{s}_z = \lambda s_y \sin\theta. \tag{C.1c}$$

In the local frame (x', y', z') defined in Figure 4.2, the components of the spin density,

$$s'_x = s_x \cos\theta - s_z \sin\theta \tag{C.2a}$$

$$s'_y = s_y \tag{C.2b}$$

$$s'_z = s_x \sin\theta + s_z \cos\theta, \tag{C.2c}$$

satisfy

$$\dot{s}'_x = -\lambda s'_y - s'_z \dot{\theta} \tag{C.3a}$$

$$\dot{s}'_y = \lambda s'_x \tag{C.3b}$$

$$\dot{s}'_z = s'_x \dot{\theta}. \tag{C.3c}$$

Eliminating s'_y gives

$$\ddot{s}'_x + (\lambda^2 + \dot{\theta}^2) s'_x + s'_z \ddot{\theta} = 0. \tag{C.4}$$

The differential Eq. (C.4) cannot be solved analytically for realistic domain wall profiles. However, it is easily solvable for the wall defined by Eq. (4.46) where one-half turn of a spin spiral with pitch $p = \pi/2w$ connects two regions with uniform (but reversed) magnetization.

In the limit $\pi/w \ll \lambda$ of a long wall, the components of the spin density transverse to the wall magnetization for the range $x \in [-w, w]$ are (after multiplying the weighting factor $k_x/\langle k \rangle$ for the semi-classical approach)

$$s'_x(x) = \frac{\hbar}{2}\frac{k_x}{\langle k \rangle}\frac{\pi}{2w\lambda}\sin(\lambda(x \pm w)) \tag{C.5a}$$

$$s'_y(x) = \frac{\hbar}{2}\frac{k_x}{\langle k \rangle}\frac{\pi}{2w\lambda}\left[1 - \cos(\lambda(x \pm w))\right], \tag{C.5b}$$

where the plus (minus) refers to electrons that flow from left (right) to right (left). The associated spin current density and spin transfer torque carried by each electron follow from Eq. (4.25) and Eq. (4.10), respectively. Bearing in mind that $\hat{\mathbf{x}}'$ varies with x, our final result for the torque (in the local frame) generated by a single electron moving from right to left is

$$N'_x = \frac{\hbar}{2}\frac{\hbar k_x}{m}\frac{k_x}{\langle k \rangle}\frac{\pi}{2w}\left[1 - \cos\lambda(x-a)\right]\ \hat{\mathbf{x}}' \tag{C.6a}$$

$$N'_y = \frac{\hbar}{2}\frac{\hbar k_x}{m}\frac{k_x}{\langle k \rangle}\frac{\pi}{2w}\sin\lambda(x-a)\ \hat{\mathbf{y}}. \tag{C.6b}$$

This may be compared with the results of Ref. [91] which pertain to the entire ensemble of conduction electrons.

Bibliography

[1] M. N. Baibich, J. M. Broto, A. Fert, F. N. V. Dau, F. Petroff, P. Eitenne, G. Creuzet, A. Friederich, and J. Chazelas, "Giant Magnetoresistance of (001)Fe/(001)Cr Magnetic Superlattices," *Phys. Rev. Lett.* **61**, 2472 (1988).

[2] G. Binasch, P. Grünberg, F. Saurenbach, and W. Zinn, "Enhanced magnetoresistance in layered magnetic structures with antiferromagnetic interlayer exchange," *Phys. Rev. B* **39**, 4828 (1989).

[3] J. A. Katine, F. J. Albert, R. A. Buhrman, E. B. Myers, and D. C. Ralph, "Current-Driven Magnetization Reversal and Spin-Wave Excitations in Co/Cu/Co Pillars," *Phys. Rev. Lett.* **84**, 3149 (2000).

[4] M. Tsoi, A. G. M. Jansen, J. Bass, W.-C. Chiang, M. Seck, V. Tsoi, , and P. Wyder, "Excitation of a Magnetic Multilayer by an Electric Current," *Phys. Rev. Lett.* **80**, 4281 (1998).

[5] S. Urazhdin, N. O. Birge, W. P. Pratt, Jr., , and J. Bass, "Current-Driven Magnetic Excitations in Permalloy-Based Multilayer Nanopillars," *Phys. Rev. Lett.* **91**, 146803 (2003).

[6] W. H. Rippard, M. R. Pufall, S. Kaka, S. E. Russek, , and T. J. Silva, "Direct-Current Induced Dynamics in $Co_{90}Fe_{10}/Ni_{80}Fe_{20}$ Point Contacts," *Phys. Rev. Lett.* **92**, 27201 (2004).

[7] A. Fert, V. Cros, J.-M. George, J. Grollier, H. Jaffrès, A. Hamzic, A. Vaurès, G. Faini, J. B. Youssef, and H. L. Gall, "Magnetization reversal by injection and transfer of spin: experiments and theory," *J. Magn. Magn. Mater.* **272**, 1706 (2004).

[8] M. D. Stiles and A. Zangwill, "Anatomy of spin-transfer torque," *Phys. Rev. B* **66**, 14407 (2002).

[9] J. C. Slonczewski, "Current-driven excitation of magnetic multilayers," *J. Magn. Magn. Mater.* **159**, L1 (1996).

[10] L. Gan, S. H. Chung, K. H. Ashenbach, M. Dreyer, and R. D. Gomez, "Pulsed-current-induced domain wall propagation in permalloy patterns observed using magnetic force microscope," *IEEE Trans. Magn.* **36**, 3047 (2000).

[11] H. Koo, C. Krafft, and R. D. Gomez, "Current-controlled bi-stable domain configurations in Ni81Fe19 elements: An approach to magnetic memory devices," *Appl. Phys. Lett.* **81**, 862 (2002).

[12] J. Grollier, P. Boulenc, V. Cros, A. Hamzic, A. Vaures, A. Fert, and G. Faini, "Switching a spin valve back and forth by current-induced domain wall motion," *J. Appl. Phys.* **83**, 509 (2003).

[13] M. Kläui, C. A. F. Vaz, J. A. C. Bland, W. Wernsdorfer, G. Faini, E. Cambril, and L. J. Heyderman, "Domain wall motion induced by spin polarized currents in ferromagnetic ring structures," *Appl. Phys. Lett.* **83**, 105 (2003).

[14] M. Tsoi, R. E. Fontana, and S. S. Parkin, "Magnetic domain wall motion triggered by an electric current," *J. Appl. Phys.* **83**, 2617 (2003).

[15] N. Vernier, D. A. Allwood, D. Atkinson, M. D. Cooke, and R. P. Cowburn, "Domain wall propagation in magnetic nanowires by spin-polarized current injection," *Europhys. Lett.* **65**, 526 (2004).

[16] A. Yamaguchi, T. Ono, S. Nasu, K. Miyake, K. Mibu, and T. Shinjo, "Real-Space Observation ofCurrent-Driven DomainWall Motion in Submicron MagneticWires," *Phys. Rev. Lett.* **92**, 077205 (2004).

[17] C. Lim, T. Devolder, C. Chappert, J. Grollier, V. Cros, A. Vaurères, A. Fert, and G. Faini, "Domain wall displacement induced by subnanosecond pulsed current," *Appl. Phys. Lett.* **84**, 2820 (2004).

[18] E. Saitoh, H. Miyajima, T. Yamaoka, and G. Tatara, "Current-induced resonance and mass determination of a single magnetic domain wall," *Nature* **432**, 203 (2004).

[19] M. Yamanouchi, D. Chiba, F. Matsukura, and H. Ohno, "Current-induced domain-wall switching in a ferromagnetic semiconductor structure," *Nature* **428**, 539 (2004).

[20] J. C. Slonczewski, "Currents and torques in metallic magnetic multilayers," *J. Magn. Magn. Mater.* **247**, 324 (2002).

[21] A. Brataas, Y. V. Nazarov, and G. E. W. Bauer, "Spin-Transport in multi-terminal normal metal-ferromagnet systems with non-collinear magnetizations," *Euro. Phys. J. B* **22**, 99 (2001).

[22] J. Manschot, A. Brataas, , and G. E. W. Bauer, "Nonmonotonic angular magnetoresistance in asymmetric spin valves," *Phys. Rev. B* **69**, 92407 (2004).

[23] M. D. Stiles, J. Xiao, and A. Zangwill, "Phenomenological Theory of Current-Induced Magnetization Precession," *Phys. Rev. B* **69**, 54408 (2004).

[24] J. Bass and W. P. Pratt, Jr., "Current-perpendicular(CPP) magnetoresistance in magnetic metallic multilayers," *J. Magn. Magn. Mater.* **200**, 274 (1999).

[25] Q. Yang, P. Holody, S.-F. Lee, L. L. Henry, R. Loloee, P. A. Schroeder, J. W. P. Pratt, and J. Bass, "Spin flip diffusion length and giant magnetoresistance at low temperatures," *Phys. Rev. Lett.* **72**, 3274 (1994).

[26] L. Piraux, S. Dubois, A. Fert, and L. Belliard, "The temperature dependence of the perpendicular giant magnetoresistance in Co/Cu multilayered nanowires," *Euro. Phys. J. B* **4**, 413 (1998).

[27] W. H. Press, B. P. Flannery, S. A. Teukolsky, and W. T. Vetterling, *Numerical Recipes* (Cambridge University Press, 1986).

[28] D. R. Penn and M. D. Stiles, "Solution of the Boltzmann equation without the relaxation-time approximation," *Phys. Rev. B* **59**, 13338 (1999).

[29] M. D. Stiles and D. R. Penn, "Calculation of spin-dependent interface resistance," *Phys. Rev. B* **61**, 3200 (2000).

[30] M. D. Stiles and A. Zangwill, "Noncollinear spin transfer in Co/Cu/Co multilayers," *J. Appl. Phys.* **91**, 6812 (2002).

[31] Y. B. Bazaliy, B. A. Jones, and S.-C. Zhang, "Current-induced magnetization switching in small domains of different anisotropies," *Phys. Rev. B* **69**, 94421 (2004).

[32] S. I. Kiselev, J. C. Sankey, I. N. Krivorotov, N. C. Emley, R. J. Schoelkopf, R. A. Buhrman, and D. C. Ralph, "Microwave oscillations of a nanomagnet driven by a spin-polarized current," *Nature* **425**, 380 (2003).

[33] M. Covington, M. AlHajDarwish, Y. Ding, N. Gokemeijer, and M. Seigler, "Current-Induced Magnetization Dynamics in Current Perpendicular to the Plane Spin Valves," *Phys. Rev. B* **69**, 184406 (2004).

[34] W. H. Rippard, M. R. Pufall, S. Kaka, T. Silva, and S. E. Russek, "Current-Driven Microwave Dynamics in Magnetic Point Contacts as a Function of Applied Field Angle," *Phys. Rev. B* **70**, 100406 (2004).

[35] I. N. Krivorotov, N. C. Emley, J. C. Sankey, S. I. Kiselev, D. C. Ralph, and R. A. Buhrman, "Time-domain measurements of nanomagnet dynamics driven by spin-transfer torques," *Science* **307**, 228 (2005).

[36] E. B. Myers, F. J. Albert, J. C. Sankey, E. Bonet, R. A. Buhrman, , and D. C. Ralph, "Thermally Activated Magnetic Reversal Induced by a Spin-Polarized Current," *Phys. Rev. Lett.* **89**, 196801 (2002).

[37] M. R. Pufall, W. H. Rippard, S. Kaka, S. E. Russek, , T. J. Silva, J. Katine, and M. Carey, "Large-angle and gigahertz-rate random telegraph switching induced by spin-momentum transfer," *Phys. Rev. B* **69**, 214409 (2004).

[38] I. N. Krivorotov, N. C. Emley, A. G. F. Garcia, J. C. Sankey, S. I. Kiselev, D. C. Ralph, and R. A. Buhrman, "Temperature Dependence of Spin-Transfer-Induced Switching of Nanomagnets," *Phys. Rev. Lett.* **93**, 166603 (2004).

[39] J. Z. Sun, D. Monsma, T. Kuan, M. Rooks, D. Abraham, B. Oezyilmaz, A. Kent, and R. Koch, "Spin-torque transfer in batch-fabricated spin-valve magnetic nanojunctions," *J. Appl. Phys.* **93**, 6859 (2003).

[40] J. Grollier, V. Jaffres, A. Hamzic, J. M. George, G. Faini, J. B. Youssef, H. L. Gall, and A. Fert, "Field dependence of magnetization reversal by spin transfer," *Phys. Rev. B* **67**, 174402 (2003).

[41] M. A. Zimmler, B. Özyilmaz, W. Chen, A. D. Kent, J. Z. Sun, M. J. Rooks, and R. H. Koch, "Current-induced effective magnetic fields in Co/Cu/Co nanopillars," *Phys. Rev. B* **70**, 184438 (2004).

[42] D. Lacour, J. Katine, N. Smith, M. Carey, and J. Childress, "Thermal Effects on the Magnetic Field Dependence of Spin-Transfer Torque-Induced Magnetization Reversal," *Appl. Phys. Lett.* **85**, 4681 (2004).

[43] J. Z. Sun, "Spin-current interaction with a monodomain magnetic body: A model study," *Phys. Rev. B* **62**, 570 (2000).

[44] Y. B. Bazaliy, B. A. Jones, and S.-C. Zhang, "Modification of the Landau-Lifshitz equation in the presence of a spin-polarized current in colossal- and giant-magnetoresistive materials," *Phys. Rev. B* **57**, 3213 (1998).

[45] Y. B. Bazaliy, B. A. Jones, and S.-C. Zhang, "Toward metallic magnetic memory: How to interpret experimental results on magnetic switching induced by spin-polarized currents," *J. Appl. Phys.* **89**, 6793 (2001).

[46] H. Xi and Z. Lin, "In-plane Magnetization dynamics driven by spin-polarized currents in magnetic nanostructures," *Phys. Rev. B* **70**, 092403 (2004).

[47] H. Morise and S. Nakamura, "Stable magnetization states under a spin-polarized current and a magnetic field," *Phys. Rev. B* **71**, 14439 (2005).

[48] S. E. Russek, S. Kaka, W. H. Rippard, M. Pufall, and T. Silva, "Finite Temperature Modelling of Spin Momentum Transfer Induced Dynamics in Magnetic Nano-devices," *Phys. Rev. B* **71**, 104425 (2005).

[49] J. Miltat, G. Albuquerque, A. Thiaville, and C. Vouille, "Spin transfer into an inhomogeneous magnetization distribution," *J. Appl. Phys.* **89**, 6982 (2001).

[50] Z. Li and S. Zhang, "Magnetization dynamics with a spin-transfer torque," *Phys. Rev. B* **68**, 24404 (2003).

[51] J.-G. Zhu and X. Zhu, "Spin transfer induced noise in CPP read heads," *IEEE Trans. Magn.* **40**, 182 (2004).

[52] K.-J. Lee, A. Deac, O. Redon, J.-P. Nozieres, and B. Dieny, "Excitations of incoherent sin-waves due to spin-transfer torque," *Nature Mater.* **3**, 877 (2004).

[53] B. Montigny and J. Miltat, "Numerical simulations of current-induced magnetic microwave excitations," *unpublished* (2005).

[54] D. V. Berkov and N. L. Gorn, "Transition from the macrospin to chaotic behavior by a spin-torque driven magnetization precession of a square nanoelemen," *Phys. Rev. B* **71**, 052403 (2005).

[55] D. V. Berkov and N. L. Gorn, "Magnetization precession due to a spin-polarized current in a thin nanoelement: Numerical simulation study," *Phys. Rev. B* **72**, 094401 (2005).

[56] N. Smith, "Basic considerations for magnetization dynamics in the combined presence of spin-transfer torques and thermal fluctuations," *arXiv* , cond.

[57] S. Bhagat and P.Lubitz, "Temperature variation of ferromagnetic relaxation in the 3 d transition metals," *Phys. Rev. B* **10**, 179 (1974).

[58] P. Bruno and J.-P. Renard, "Magnetic Surface Anisotropy of Transition Metal Ultrathin Films," *Appl. Phys. A* **49**, 499 (1989).

[59] R. D. McMichael, (private communication).

[60] Y. Tserkovnyak, A. Brataas, G. E. W. Bauer, and B. I. Halperin, "Nonlocal magnetization dynamics in ferromagnetic hybrid nanostructures," *Rev. of Mod. Phys.* **77**, 1375 (2005).

[61] H. Suhl, "Theory of the Magnetic Damping Constant," *IEEE Trans. Magn.* **34**, 1834 (1998).

[62] V. Kambersky, "On the Landau-Lifshitz relation in ferromagnetic metals," *Can. J. Phys.* **48**, 2906 (1970).

[63] D. L. Mills and S. M. Rezende, *Spin Dynamics in Confined Magnetic Structures II* (Springer-Verlag, Berlin, 2003), edited by B. Hillebrands, and K. Ounadjela, Topics in Appl. Phys. Vol. 87.

[64] A. Rebei, M. Simionato, and G. J. Parker, "Correlation functions of the magnetization in thin films," *Phys. Rev. B* **69**, 134412 (2004).

[65] V. L. Safonov, "Tensor form of magnetization damping," *J. Appl. Phys.* **91**, 8653 (2002).

[66] V. L. Safonov, "Microscopic mechanisms of magnetization reversal," *J. Appl. Phys.* **95**, 7145 (2004).

[67] D. Fredkin and A. Ron, "Microsopic derivation of the Landau-Lifshitz equation for ferromagnetic relaxation," *Phys. Rev. B* **61**, 8654 (2000).

[68] J. Mallinson, "On Damped Gyromagnetic Precession," *IEEE Trans. Magn.* **23**, 2003 (1987).

[69] W. F. Brown, Jr., "Thermal Fluctuations of a Single-Domain Particle," *Phys. Rev.* **130**, 1677 (1963).

[70] D. Berkov, "Fast Switching of Magnetic Nanoparticles: Simulation of Thermal Noise Using the Langevin Dynamics," *IEEE Trans. Magn.* **38**, 2489 (2002).

[71] G. N. Milshtein, "A Method of second-order accuracy integration of stochastic differential equations," *Theory Prob. Appl.* **23**, 396 (1978).

[72] S. Urazhdin, R. Loloee, and J. W. P. Pratt, "Giant Magnetoresistance in Multilayers with Noncollinear Magnetizations," *arXiv* , cond (2004).

[73] K. Xia, P. J. Kelly, G. E. W. Bauer, A. Brataas, , and I. Turek, "Spin torques in ferromagnetic normal-metal structures," *Phys. Rev. B* **65**, 220401 (2002).

[74] Y. Tserkovnyak, A. Brataas, and G. E. W. Bauer, "Enhanced Gilbert Damping in Thin Ferromagnetic Films," *Phys. Rev. Lett.* **88**, 117601 (2002).

[75] E. Simanek and B. Heinrich, "Gilbert damping in magnetic multilayers," *Phys. Rev. B* **67**, 144418 (2003).

[76] D. Mills, "Ferromagnetic resonance relaxation in ultrathin films: the role of conduction electrons," *Phys. Rev. B* **68**, 014419 (2003).

[77] R. Urban, G. Woltersdorf, and B. Heinrich, "Gilbert damping in single and multilayer ultrathin films: Role of interfaces in nonlocal spin dynamics," *Phys. Rev. Lett.* **87**, 217204 (2001).

[78] S. Mizukami, Y. Ando, and T. Miyazaki, "Effect of spin diffusion on Gilbert damping for a very thin permalloy layer in Cu/permalloy/Cu/Pt films," *Phys. Rev. B* **66**, 104413 (2002).

[79] S. Ingvarsson, L. Ritchie, X. Y. Liu, G. Xiao, J. C. Slonczewski, P. L. Trouilloud, and R. H. Koch, "Role of electron scattering in the magnetization relaxation of thin Ni81Fe19 films," *Phys. Rev. B* **66**, 214416 (2002).

[80] K. Lenz, T. Tolìnski, J. Lindner, E. Kosubek, and K. Baberschke, "Evidence for spin-pumping effect in the ferromagnetic resonance of coupled trilayers," *Phys. Rev. B* **69**, 144422 (2004).

[81] Y. Tserkovnyak, A. Brataas, and G. E. W. Bauer, "Dynamic stiffness of spin valves," *Phys. Rev. B* **67**, 140404 (2003).

[82] J. Xiao, A. Zangwill, and M. D. Stiles, "Boltzmann Test of Slonczewski's Theory of Spin Transfer Torque," *Phys. Rev. B* **70**, 172405 (2004).

[83] C. Kittel, "On the Theory of Ferromagnetic Resonance Absorption," *Phys. Rev.* **73**, 155 (1948).

[84] M. D. Stiles and J. Miltat, *Spin Dynamics in Confined Magnetic Structures III* (Springer-Verlag, Berlin, 2003), edited by B. Hillebrands, and K. Ounadjela.

[85] C. Back, R. Allenspach, W. Weber, S. Parkin, D. Weller, E. Garwin, and H. Seigmann, "Minimum Field Strength in Precessional Magneization Reversal," *Science* **285**, 864 (1999).

[86] P. Kabos, S. Kaka, S. Russek, and T. Silva, "Metastable States in large angle magnetization rotations," *IEEE Trans. Magn.* **36**, 3050 (2000).

[87] W. Hiebert, G. Ballentine, and M. Freeman, "Comparison of experimental and numerical micromagnetic dynamics in coherent precessional switching and modal oscillations," *Phys. Rev. B* **65**, 140404 (2002).

[88] A. Y. Dobin and R. Victora, "Intrinsic Nonlinear Ferromagnetic Relaxation in Thin Metallic Films," *Phys. Rev. Lett.* **90**, 167203 (2003).

[89] H. Xi, K.-Z. Gao, and Z. Lin, "Circuits, Devices Syst.," 2005, (in press).

[90] L. Berger, "Low-field Magnetoresistance and domain drag in ferromagnets," *J. Appl. Phys.* **49**, 2156 (1978).

[91] X. Waintal and M. Viret, "Current-induced distrotion of a magnetic domain wall," *Europhys. Lett.* **65**, 427 (2004), cond-mat/0301293.

[92] S. Zhang and Z. Li, "Roles of Nonequilibrium Conduction Electrons on the Magnetization Dynamics of Ferromagnets," *Phys. Rev. Lett.* **93**, 127204 (2004).

[93] G. Tatara and H. Kohno, "Theory of Current-Driven DomainWall Motion: Spin Transfer versus Momentum Transfer," *Phys. Rev. Lett.* **92**, 086601 (2004).

[94] A. Thiaville, Y. Nakatani, J. Miltat, and Y. Suzuki, "Micromagnetic understanding of current-driven domain wall motion in patterned nanowires," *Europhys. Lett.* **69**, 990 (2005).

[95] S. E. Barnes and S. Maekawa, "Current-Spin Coupling for Ferromagnetic Domain-Walls in Fine Wires," *Phys. Rev. Lett.* **95**, 107204 (2005).

[96] J. He, Z. Li, and S. Zhang, "Effects of current on vortex and transverse domain walls," *arXiv* , cond (2005).

[97] Z. Li, J. He, and S. Zhang, "Effects of spin current on ferromagnets," *arXiv* , cond (2005).

[98] J. Jensen and A. K. Mackintosh, *Rare Earth Magnetism* (Oxford University Press, 1991).

[99] M. Marsman and J. Hafner, "Broken symmetries in the crystalline and magnetic structures of ?-iron," *Phys. Rev. B* **66**, 224409 (2002).

[100] S. Zhang, P. M. Levy, and A. Fert, "Mechanisms of Spin-Polarized Current-Driven Magnetization Switching," *Phys. Rev. Lett.* **88**, 236601 (2002).

[101] L. Berger, "Possible existence of a Josephson effect in ferromagnets," *Phys. Rev. B* **33**, 1572 (1986).

[102] A. Thiaville, Y. Nakatani, J. Miltat, and N. Vernier, "Domain wall motion by spin-polarized current: a micromagnetic study," *J. Appl. Phys.* **95**, 7049 (2004).

[103] M. Klaui, P. O. Jubert, R. Allenspach, A. Bischof, J. Bland, G. Faini, and U. Rudiger, "Direct Observation of Domain-Wall Configurations Transformed by Spin Currents," *Phys. Rev. Lett.* **95**, 026601 (2005).

[104] D. Ravelosona, D. Lacour, J. A. Katine, B. D. Terris, and C. Chappert, "Nanometer Scale Observation of High Efficiency Thermally Assisted Current-Driven DomainWall Depinning," *Phys. Rev. Lett.* **95**, 117203 (2005).

[105] J. William F. Brown, *Magnetostatic Principles in Ferromagnetism* (North-Holland Publishing Company, 1962).

[106] M. Calvo, "Quantum theory of neutrons in helical magnetic fields," *Phys. Rev. B* **18**, 5073 (1978).

[107] O. Wessely, B. Skubic, and L. Nordström, "Current driven magnetization dynamics in helical spin density waves," *arXiv* , cont (2005).

[108] Y. Aharonov and A. Stern, "Origin of the geometric forces accompanying Berry's geometric potentials," *Phys. Rev. Lett.* **69**, 3593 (1992).

[109] A. Hubert and R. Schäfer, *Magnetic Domains* (Springer-Verlag, Berlin, 1998).

[110] V. K. Dugaev, J. Barnas, A. Lusakowski, and L. A. Turski, "Electrons in a ferromagnetic metal with a domain wall," *Phys. Rev. B* **65**, 224419 (2002).

[111] J. A. Osborn, "Demagnetizing Factors of the General Ellipsoid," *Phys. Rev.* **67**, 351 (1945).

VITA

Jiang Xiao was born in Xingguo, Jiangxi Province of China, in August 1979. He received his Bachelor degree of Science in Physics from Peking University, Beijing, China, in 2001. Since then, he has been conducting graduate research under supervision of Professor Andrew Zangwill in the School of Physics, Georgia Institute of Technology. He also received Master of Science in Mathematics from the School of Mathematics at Georgia Tech in 2005.